Chapter 1

Introduction

When reactive systems are embedded in a fluid environment, their constituent particles, which interact via chemical, biological or other active processes, are transported by the fluid flow. Such a flow is referred to as an active flow. The reactant particles are assumed to be passively advected in that they do not affect the dynamics of the fluid flow; however, the nature of the underlying hydrodynamic advection can impact the dynamics of the reaction process [10, 118, 166]. Of particular interest in recent years is the case where these active flows exhibit chaos [123, 158, 159, 156, 155]. In this thesis we shall examine the behaviour of chaotically stirred reactive systems using a recently developed analytical method [47], which was introduced in the context of unstirred excitable media and which we extend to active chaotic flows.

The field of active flows is a rapidly developing interdisciplinary area of nonlinear science that has attracted a lot of interest due to the ubiquitousness of such flows in nature and industry. They are found to occur in many environmental contexts including the development of plankton blooms [2, 15, 4, 3, 83, 151, 81, 86, 41, 85, 88, 84, 51], the increased depletion of ozone in the stratosphere caused by chlorine filaments [29, 30, 147, 169, 168], the clustering of populations of "brownian bugs" [170] and the growth inhibition of dinoflagellates [42]. They are also found in a number of other contexts such as continuously fed or batch reactors [31, 8], population dynamics [138, 54, 59, 139], combustion processes [167, 133, 45, 44, 126], polymerisations [110, 74, 66], geophysical processes [140, 50, 153], pharmaceutical operations [105] and several chemical systems [7, 31, 94, 93, 96, 124].

The individual reactant particles or tracers of reactive systems are stirred and advected by time-dependent laminar flows, which can result in Lagrangian chaos [10, 20, 61, 148, 120, 118]. Chaoticity implies a sensitive dependence of the behaviour of the advected particles on the initial condi-

tions. In the context of active flows, this was first examined in [96] for a set of competing autocatalytic reactions. Here it was observed that for very small changes in the initial condition, the coupling of the reaction process with the underlying chaotic advection will alter the composition of the final product mix of the reaction. Active chaotic flows display a number of phenomena that are not observed in unstirred flows. For example, chaotic flows can determine synchronisation in oscillatory excitable media [172, 114] and are found to be a crucial factor in the nontrivial coexistence of competing aquatic species [139]. It has also been observed that a differential fluid flow can generate a non-Turing mechanism for pattern formation [135]. We note that chaotic stirring can affect the behaviour of reactive systems both in the case of open flows [155] which occur over an infinite domain, as well as in closed flows [96], where the fluid motion is constrained to a finite region.

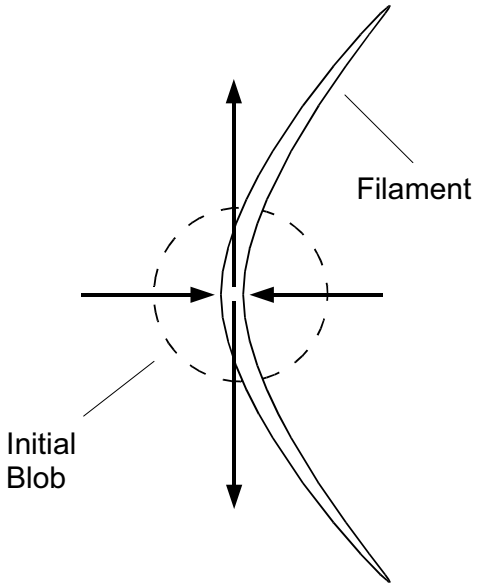

Figure 1.1: Sketch of an initial blob (represented by a dashed circle) being stretched and compressed into an elongated filamental structure in a hyperbolic region of a chaotic fluid flow. The arrows represent the directions of stretching and compression.

Chaotic flows are characterised by hyperbolic regions of stretching and compression which cause fluid parcels to form elongated filamental structures as seen in Fig. 1.1. The advection of reactant tracers along these filaments leads to an increase in the surface area of the tracers. This greatly affects the reaction kinetics leading to phenomena such as those described above.

The evolution of these filamental structures was first considered in [40] and has been numerically described in [106, 107, 100, 121, 79, 78, 80, 57, 9]. The filamentation process is beautifully illustrated in dye droplet experiments [17, 20, 120, 76, 75, 152, 57, 150, 149, 134]. An experimental study of the behaviour of reacting particles in a chaotic flow was first done in [71].

An increase in the stirring rate leads to a greater compression of the filaments. However, the widths of the filaments remain finite due to diffusion, which tries to balance the effect of the stretching flow. When the stirring rate is too large, the filaments are compressed to the extent that the reaction cannot be sustained. This corresponds to a saddle-node bifurcation, and is of great physical significance as it relates to the often unwanted termination of a reaction by the mixing process. This bifurcation is generic to chaotically stirred reaction-diffusion systems, and is found to occur both in open flows, where the filaments eventually leave the fluid container, and in closed flows, where they fill up the entire container and become too thin to allow the reaction to spread [113]. In addition to this stirring-induced saddle-node bifurcation, other bifurcation scenarios and solution behaviours may arise depending on the reaction kinetics of the system. For example, as we shall see in Chapter 5, a chaotically stirred excitable system will also exhibit a supercritical Hopf bifurcation, a previously unreported region of bistability characterised by a hysteresis loop and a saddle-node arising from propagation failure.

The focus of this thesis is the solution behaviour near these bifurcations, which we shall qualitatively and quantitatively describe. The analytical method that we use involves a nonperturbative, non-asymptotic variational approach where appropriate parameterised test functions are fitted to the solution. This method is ideally suited to investigate the system dynamics in regions where the solution takes a well defined form. For example, this method will provide a good description of the solution behaviour close to the saddle-node where, as we shall see in the following chapters, the solution assumes a bell-shaped profile. We note that this method has an advantage over traditional asymptotic techniques such as asymptotic matching, which are only applicable for solutions which are separable into distinct inner and outer solutions (usually separated by a steep narrow front) [13]. The use of this nonperturbative method requires no such preconditions on the nature of the solution profile. We test this method against numerical simulations of the equations describing the systems.

Early numerical models of active chaotic flows considered the behaviour of discrete interacting particles in the absence of diffusion [101, 14, 96]. Subsequently, most studies of these problems have involved a continuous approach, where the system behaviour has been described using a reaction-advection-

diffusion model [129, 130, 99, 137, 132, 131, 171]. The dynamics of an imperfectly mixed chemical or biological system with N components can be described by the following equations [111, 115, 113, 52]

$$\frac{\partial c_i(\mathbf{x},t)}{\partial t} + \mathbf{v}(\mathbf{x},t)\cdot\nabla c_i(\mathbf{x},t) = D_i\,\nabla^2 c_i(\mathbf{x},t) + k\,\mathcal{F}_i(c_1,\ldots,c_N)\ , \quad (1.1)$$

where $i = 1\ldots N$, and where $c_i(\mathbf{x},t)$ are dimensionless quantities corresponding to characteristics of the reactants such as the concentration or the temperature. The advecting velocity $\mathbf{v}(\mathbf{x},t)$ is assumed to be chaotic. The interactions between the tracers are described by a set of reaction terms $\mathcal{F}_i$ with reaction rate k. The parameters D_i represent the diffusion coefficients of the components. To simplify the following discussion we assume that all components diffuse equally, $D_i = D$.

We may non-dimensionalise (1.1) by introducing the variables $x' = x/L$, $t' = t\,(V/L)$ and $v' = v/V$, where L and V are the characteristic length and velocity scales respectively. Omitting the primes, we obtain

$$\frac{\partial c_i(\mathbf{x},t)}{\partial t} + \mathbf{v}(\mathbf{x},t)\cdot\nabla c_i(\mathbf{x},t) = \mathcal{P}^{-1}\,\nabla^2 c_i(\mathbf{x},t) + Da\,\mathcal{F}_i(c_1,\ldots,c_N)\ , \quad (1.2)$$

where we have introduced two non-dimensional variables: the Péclet number $\mathcal{P} = L\,V/D$ [72], which measures the ratio of the time scales of stirring and diffusion and the Damköhler number $Da = k\,L/V$ [27], which measures the ratio of the time scales of reaction and stirring. A system with a small value of Da is dominated by stirring, while a system with a large value of Da is reaction-dominated.

This model has been used to numerically describe the two-dimensional (2-D) behaviour of chaotically stirred reactive systems [111, 115, 113, 52]. However, the nature of these equations, which involve multi-scale processes, do not allow for a complete analytical treatment. We shall therefore consider a one-dimensional (1-D) reduction of (1.1), which will also allow us to numerically describe the local dynamics of the reactive system with much less computational effort. These 1-D models will be a caricature of the full 2-D problem which allows us to study generic instabilities and bifurcations of filaments in a 2-D chaotically stirred environment.

A critical account of such reductions is given in [25], where a number of simplified models were tested against the corresponding full 2-D system over a range of the Péclet number $\mathcal{P}$. Reduced models which ignore the effect of spatial inhomogeneities [77] were found to be valid only in the limit $\mathcal{P} \to 0$, where the effects of diffusion are much stronger than that of fluid mixing. A more advanced set of models, known as lamellar models [122, 128, 116, 117, 119], were found to provide a better description of the full solution

behaviour. Models of this type were originally introduced in the context of mixing in time-dependent laminar flows, and were motivated by studies that considered the connection between the dynamics of chemical reactions and the underlying flows [36, 37, 70]. In such models, the intricate filamental structures that arise in chaotic flows are approximated as lamellar arrays. These lamellar structures are described in detail in [162]. The lamellar arrays are often assumed to be 1-D as this greatly simplifies the numerical analysis. The accuracy of 1-D lamellar models was considered in [21] where it was found that such models provide a fairly good description of the behaviour of the full 2-D system up to moderately large values of $\mathcal{P}$. Lamellar models have been used in [19] for the description of single-bimolecular, competitive-consecutive and competitive-parallel reaction schemes, and in [18, 33, 34, 35] to describe polymerisation. They have since been examined numerically [102, 103, 104] and analytically [145, 146] for reactions of the type $A + B \to P$.

Two 1-D lamellar models were tested in [25]: a model where the effect of fluid mixing was described with a continuous stretching term, and a model where the effect of fluid folding (a generic characteristic of the 2-D flow) was described using a Baker transformation. It was observed that both models provide fairly good predictions for behaviour of the full system for values of $\mathcal{P}$ up to around $\mathcal{P} \approx 300$. Moreover, the lamellar model with continuous stretching captures the monotonic fall in the product yield observed when increasing $\mathcal{P}$ in the full 2-D system.

In this thesis we consider a lamellar model of this type, known as the Lagrangian filament model [111, 115, 113], which describes the local behaviour of a single filament under the influence of continuous stretching. We note that for appropriate choices of the length and velocity scales, specifically for $L = V^{-1}$, the Péclet number can simply be expressed as $\mathcal{P} = D^{-1}$. In the following chapters, we shall therefore consider the diffusion coefficients of the components rather than the Péclet number.

In the next chapter we describe the 1-D lamellar model which we use to numerically examine several one- and two-component reactive systems. We also describe the generic solution behaviour of chaotically stirred reaction-advection-diffusion equations which can be captured using such a model, as well as the asymptotic solution behaviour for various limiting cases of Da. In Chapter 3 we introduce the nonperturbative method that we use to analyse these systems. We demonstrate the versatility of this method in subsequent chapters by considering various reactive systems with multiple homogeneous steady states. In Chapter 4 we consider two one-component systems, an autocatalytic and a bistable system. Both systems possess a specific critical value Da_c as a lower bound for the existence of stable non-trivial solutions. While this value corresponds to a saddle-node bifurcation of two non-trivial

solutions in the bistable system, it is a transcritical bifurcation of a non-trivial solution with the trivial solution branch itself in the autocatalytic system. The solution behaviour of the two systems is examined close to the bifurcations as well as far away from them. We then examine a two-component excitable system in Chapter 5. A detailed numerical investigation of this excitable system reveals a variety of previously unexamined phenomena. We provide a non-exhaustive account of the various bifurcations and solution behaviours observed in this system. We find that the nonperturbative method can be used to closely describe these behaviours. In Chapter 6 we study the flame filament structures that arise in a two-component combustion system. The nonperturbative method is used to describe the solution behaviour near the saddle-node bifurcation. We present an empirical formula for the speed of a propagating flame front that we shall use in conjunction with the nonperturbative method to describe the solution behaviour far from the saddle-node. We conclude with a summary in Chapter 7.

All numerical calculations were carried out using the MATLAB computer package. Part of Chapters 4 and 6 has been previously published in [91] and [92] respectively. Part of Chapter 5 has been submitted for publication [90].

Chapter 2

The Lagrangian filament model

2.1 Description of the model

We now derive a 1-D reduced model of the system (1.1) for the local behaviour of the filament structures that arise in an active chaotic flow (see Fig. 1.1). As the concentration of reactants along the filaments is homogenised by the local stirring, one may construct a model for the description of the cross-filament concentration where gradients arise due to the compression of the ambient chaotic flow. These so-called Lagrangian filament models were used to describe the solution of a number of chaotically stirred reaction-diffusion systems including autocatalytic, bistable and excitable systems [111, 115, 113]. The model has subsequently been applied to a variety of contexts [53, 64, 63] and has been found to qualitatively describe several important features of the full system [113]. We note that similar models have also been considered in the study of oceanic plankton distributions [83, 88].

We shall focus on the behaviour of these filaments by introducing a local coordinate system (x, y) where x is across the filament and y is along it. We describe the effect of the local advecting velocity field by considering continuous stretching in pure strain flow, i.e. we take $\mathbf{v}(\mathbf{x}, t) = (-\lambda x, \lambda y)$. Here the directions of the stable compression and the unstable stretching of the straining flow are along the x and y axes respectively. The strain rate λ can be thought of as the Lagrangian mean strain in the contracting direction, given by the absolute value of the negative Lyapunov exponent [118], or alternatively by the topological entropy [9, 6]. However, it has been found that the use of the topological entropy leads to a worse approximation of the full 2-D system [25]. For a different approach to this problem see [154, 157].

This flow results in the homogenisation of the concentration of the tracer along the direction of stretching. Simultaneously, strong gradients occur in the direction of compression. This allows us to make a reduction by

restricting to the local dynamics along the direction of compression of the filament. The compressing part of the velocity is given by

$$\mathbf{v}_{\text{stir}} = -\lambda\, x\,, \tag{2.1}$$

and we therefore replace the full system (1.1) with the following set of 1-D reaction-advection-diffusion equations for the transverse profile of the tracer filament

$$\frac{\partial c_i\,(x,t)}{\partial t} - \lambda\, x\, \frac{\partial c_i\,(x,t)}{\partial x} = D_i\, \frac{\partial^2 c_i\,(x,t)}{\partial x^2} + k\, \mathcal{F}_i\,(c_1, \ldots, c_N)\ , \tag{2.2}$$

where we have introduced a characteristic reaction rate, k.

The equation (2.2) can be non-dimensionalised by introducing variables $t' = \lambda\, t$ and $x' = \sqrt{\lambda}\, x$. Substituting the variables into (2.2) and omitting the primes, we obtain

$$\frac{\partial c_i}{\partial t} = D_i\, \frac{\partial^2 c_i}{\partial x^2} + x\, \frac{\partial c_i}{\partial x} + Da\, \mathcal{F}_i\,(c_1, \ldots, c_N)\ , \tag{2.3}$$

where we have introduced the Damköhler number, $Da = k/\lambda$.

Although the dynamics of this 1-D filament model depends strongly on the reaction term $\mathcal{F}_i$, systems of this type exhibit several generic features which we shall now describe.

2.2 Generic solution behaviour

Chaotically stirred systems of the type (2.3) typically have stationary solutions ($\partial c_i/\partial t = 0$), which arise from the balance between the inwards-directed advection and the outwards-directed diffusion-mediated propagation. This can be understood by the following phenomenological picture.

In the corresponding unstirred system, starting from a sufficiently large initial condition centred at $x = 0$, a travelling wave evolves and propagates with a constant velocity $\mathbf{v}_{\text{diff}} = \pm v_0$ to $\pm\infty$ [98, 60, 142]. In the stirred system (2.2), we have the additional inwards-directed x-dependent velocity $\mathbf{v}_{\text{stir}} = -\lambda\, x$ from (2.1). As illustrated in Fig. 2.1, when the magnitudes of these two velocities are equal the travelling wave will cease to propagate. We will therefore have a stationary solution with wave fronts at the spatial location $\mu = \pm v_0/\lambda$. In the non-dimensional system (2.3), we rescale to obtain $\mu = \pm v_0$. The total extent of such a stationary front is $2\,\mu = 2\,v_0$.

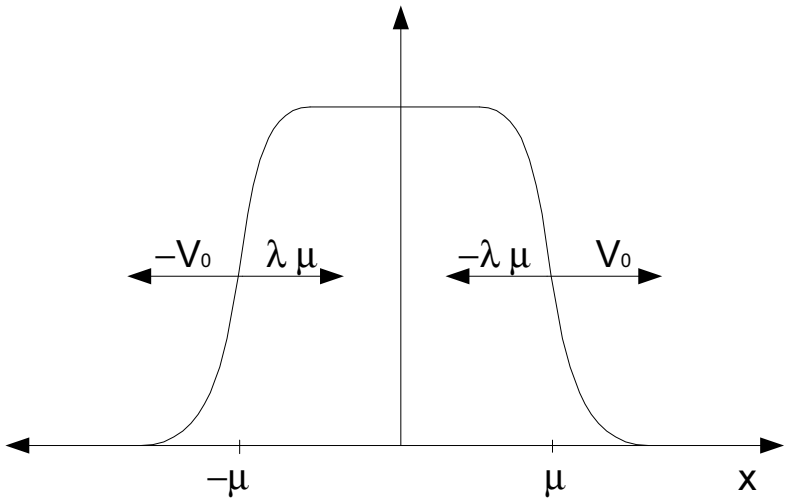

Figure 2.1: Sketch of a stationary solution of the chaotically stirred system. At $x = \pm\mu$, there is a balance between the outward propagating velocity $\pm v_0$ and the inward-directed advection $-\lambda\, x$.

The stationary solutions of the non-dimensionalised model (2.3) are

$$D_i \frac{d^2 c_i}{dx^2} + x \frac{dc_i}{dx} + Da\, \mathcal{F}_i\,(c_1, \ldots, c_N) = 0\,. \tag{2.4}$$

The behaviour of these solutions depends on the rate at which the system is stirred. As we decrease the value of Da the stirring rate increases, resulting in greater compression of the filaments. Below a critical value Da_c the filaments are too compressed to sustain the reaction, and hence no solutions exist. For values of $Da > Da_c$, we observe that nontrivial stable and unstable stationary solutions coexist. At the critical value these stable and unstable solution branches collide in a saddle-node bifurcation. We now describe the asymptotic behaviour of the stationary solutions in some limiting cases [26].

2.3 Asymptotic solution behaviour

2.3.1 Asymptotic solution for large Da

In the limit of large Damköhler numbers, the system (2.3) behaves like an unstirred system. This is intuitively plausible since the limit $Da(= k/\lambda) \to \infty$ corresponds to $\lambda \to 0$. More precisely, this can be seen by zooming into the small spatial scale $\xi = \sqrt{Da}\, x$ to transform the system (2.3) to the unstirred steady-state system up to order $\mathcal{O}(Da^{-1})$.

As discussed above, the location of the stationary solution is given by the balance of the outward directed diffusion and the inward directed compression of the flow. As we shall see in subsequent chapters, for the reaction-diffusion systems that we consider the distance of the stationary front from $x = 0$ scales with $\sqrt{Da}$. We set $\mu = \sqrt{Da}\,\bar{\mu}$, with $\bar{\mu} = \mathcal{O}(1)$. We therefore scale

$$\xi = \sqrt{Da}\,\left(x - \sqrt{Da}\,\bar{\mu}\right)\,, \tag{2.5}$$

and rescale (2.2) to obtain the following equation for the steady state solutions

$$D_i\,\frac{d^2c_i}{d\xi^2} + \bar{\mu}\,\frac{dc_i}{d\xi} + \mathcal{F}_i\,(c_1,\ldots,c_N) = \mathcal{O}(Da^{-1})\,. \tag{2.6}$$

This describes solutions of the corresponding unstirred system in a frame of reference that is moving with speed $v_0 = \bar{\mu}$, which directly relates to the phenomenological argument that the stationary solution arises from a balance between the velocities of advection and diffusion.

2.3.2 Asymptotic solution for small Da

The solution behaviour close to the stirring induced saddle-node of systems of this type can be described asymptotically. For small values of Da, we shall expand c_i as

$$c_i(x,t) = Da\,c_{0i}(x,t) + \mathcal{O}(Da^2)\,. \tag{2.7}$$

At leading order, the full system (2.3) is found to be satisfied by

$$c_{0i}(x,t) = f_{0i}(t)\,\exp(-w_i^2(t)\,x^2)\,, \tag{2.8}$$

where the behaviour of the amplitude $f_{0i}(t)$ and inverse pulse width $w_i(t)$ is given by

$$\frac{1}{f_{0i}(t)}\frac{df_{0i}}{dt} - 2\,w_i(t)\,x^2\,\frac{dw_i}{dt} = D_i\,\left(4\,w_i(t)^4\,x^2 - 2\,w_i(t)^2\right) - 2\,w_i(t)^2\,x^2\,, \tag{2.9}$$

and where both $f_{0i}(t)$ and $w_i(t)$ are non-negative for the physically realistic case. As the condition (2.9) has to hold for all x, we obtain the individual conditions

$$\frac{df_{0i}}{dt} = -2\,D_i\,f_{0i}(t)\,w_i(t)^2\,, \tag{2.10}$$

$$\frac{dw_i}{dt} = w_i(t)\,\left(1 - 2\,D_i\,w_i^2(t)\right)\,. \tag{2.11}$$

We immediately see that f_0 goes to zero for $t \to \infty$. The solution of (2.11) converges, for positive initial conditions, to $w_i(t) \to 1/\sqrt{2\,D_i}$. The temporal

decay of the amplitude f_0 captures the solution behaviour for Damköhler numbers below Da_c. In the actual full system, Da_c is an $\mathcal{O}(1)$ quantity. However, as we shall see in the following chapters, the solution profile of various systems of the type (2.3) near the saddle-node is still well approximated by a Gaussian. We shall use this asymptotic result with the nonperturbative method described in the next chapter to motivate the choice of test function near the saddle-node.

In this thesis, we study several systems where the reaction terms $\mathcal{F}_i$ are nonlinear, and which permit multiple steady-state solutions. Depending on the system, the chaotic stirring may give rise to more complex bifurcation scenarios than the generic saddle-node described above. For example, in Chapter 5 we explore Hopf bifurcations and regions of hysteresis. The full set of partial differential equations (2.3) will be numerically evaluated via a semi-implicit Crank-Nicolson scheme, with the nonlinearities treated using an Adams-Bashforth scheme [127]. The steady-state solutions ($\partial c_i/\partial t = 0$) can be found via a shooting technique, which allow us to obtain both stable and unstable solutions. A detailed explanation of these numerical methods is provided in Appendix A. In the next chapter we will describe a method to analytically investigate the solution and bifurcation behaviour of (2.3).

Chapter 3

A variational method to approximate solution profiles

3.1 Introduction

In previous studies of chaotically stirred reaction-diffusion systems, the solution in various limiting cases was described using asymptotic techniques. Specifically, if the solution is separable into inner and outer regions then an approximate solution can be obtained by asymptotically matching the two limiting solutions [13]. Such methods are applicable in regions of the chaotically stirred system (2.3) where the concentration profile is plateau-like. This is commonly observed far from the bifurcation points in these systems. Here the solution is characterised by flat inner and outer regions separated by a steep narrow front. These techniques have been used to describe the solution of a chaotically stirred combustion system in several limiting cases [64].

However, asymptotic matching techniques are found to break down near saddle-node bifurcations of (2.3). This is due to the fact that the solutions near the bifurcation points of these systems exhibit a pulse-like behaviour for which there is no clear distinction between the inner and outer regions. This behaviour is seen in various systems that we shall consider (see Chapters 4, 5 and 6). One therefore requires a more general method of analysis which can be used to describe the solution behaviour of such systems over the entire parameter space.

One such method, which takes a nonperturbative, non-asymptotic variational approach to the analysis of the solution behaviour, was developed in the context of critical wave propagation of single pulses and wave trains in unstirred 1-D and 2-D excitable media [47]. This method makes explicit use of the near-symmetric pulse-like solution profile near saddle-node bifurcations. It involves restricting the solution space of the system to that of

a set of parameterised test functions which approximate the profiles of the solutions. The parameters are then varied to give the best possible fit to the solution, analogous to the method of collective coordinates in the context of solitary waves [142]. The method can be generalised to study the solution behaviour in chaotically stirred reaction-diffusion systems, and has been successfully applied to several such systems [91, 26, 92, 90].

3.2 Description of method

To study the solution behaviour of a chaotically stirred system (2.3), we choose a set of test functions that approximates the profiles of c_i at some fixed values of the equation parameters. We use the ansatz

$$c_i(x,t) = C_i(x, p_i^j(t)) \,, \quad i = 1, \ldots, N \,, \quad j = 1, \ldots, m_i \,, \tag{3.1}$$

where $C_i(x, p_i^j(t))$ are the corresponding test functions, each with m_i time-dependent parameters $\left\{p_i^j(t)\right\}$. The number of free parameters for each component will vary depending on the nature of the test function chosen. They typically represent quantities such as the amplitude, width and steepness of the test function. The total number of parameters of the solution space will be denoted by $M = \sum_i m_i$.

We restrict the solution space of (2.3) to the subspace defined by (3.1). This gives us a set of N equations

$$-\frac{\partial C_i}{\partial t} + D_i \frac{\partial^2 C_i}{\partial x^2} + x \frac{\partial C_i}{\partial x} + Da\, \mathcal{F}_i \left(C_1, \ldots, C_N\right) = \varkappa_i \left(x,t\right) \,, \tag{3.2}$$

where $\varkappa_i \left(x,t\right)$ is the error obtained by making this restriction. The parameters $\left\{p_i^j(t)\right\}$ are then appropriately determined such that this error is minimised. This can be achieved by demanding that the error $\varkappa_i \left(x,t\right)$ is orthogonal to the tangent space of the restricted subspace, which is spanned by the set of basis functions $\partial C_i / \partial p_i^j$. This condition assures that the error lies in the orthogonal complement of the function space spanned by the prescribed test functions. This error is obviously small if the actual solution is well approximated by the test function. There are m_i such orthogonality conditions for each of the N test functions. We obtain a total of $M = \sum_i m_i$ orthogonality conditions

$$\left\langle -\frac{\partial C_i}{\partial t} + D_i \frac{\partial^2 C_i}{\partial x^2} + x \frac{\partial C_i}{\partial x} + Da\, \mathcal{F}_i \left(C_1, \ldots, C_N\right) \middle| \frac{\partial C_i}{\partial p_i^j} \right\rangle_x = 0 \,, \tag{3.3}$$

where again $i = 1, \ldots, N$ and $j = 1, \ldots, m_i$, and where the brackets denote integration over the whole domain. These conditions determine the M

free parameters $\left\{p_i^j(t)\right\}$ of these test functions. The time-derivatives of C_i appearing in (3.3) are given by

$$\frac{\partial C_i}{\partial t} = \sum_j \frac{\partial C_i}{\partial p_i^j} \frac{dp_i^j}{dt} \,. \tag{3.4}$$

By substituting this in (3.3), we obtain a set of M coupled ordinary differential equations for $\left\{p_i^j(t)\right\}$. This constitutes a dimensional reduction, as instead of solving a set of infinite-dimensional partial differential equations one only needs to solve these M equations to obtain the time-dependent behaviour of the parameters of the test function, thus allowing us to model the evolution of the concentrations of the tracers of the system.

A problem of particular interest is the behaviour of the steady-state solutions in various limiting cases of the system. As discussed in Sec. 2.2, near the saddle-node bifurcation we have the coexistence of stable and unstable steady-state solutions. We can analyze the solution in this case by setting $\partial C_i/\partial t = 0$ in (3.3) to obtain

$$\left\langle D_i \frac{\partial^2 C_i}{\partial x^2} + x \frac{\partial C_i}{\partial x} + Da\, \mathcal{F}_i\left(C_1, \ldots, C_N\right) \middle| \frac{\partial C_i}{\partial p_i^j} \right\rangle_x = 0 \,. \tag{3.5}$$

This is also a dimensional reduction, as instead of solving the set of ordinary differential equations for the steady state solutions one only needs to solve these M algebraic equations to obtain expressions for the M variables $\left\{p_i^j(t)\right\}$ in terms of the equation parameters.

The time-independent algebraic equations can be used to study stationary bifurcations such as the saddle-node mentioned above. In the region of the saddle-node, one typically observes a quadratic behaviour in the parameters, where two values of each $\left\{p_i^j\right\}$ coexist at every value of Da. The critical Damköhler number Da_c, which corresponds to the stirring induced saddle-node, can be obtained from the expressions for the parameters by requiring that we have a unique value of each $\left\{p_i^j\right\}$.

To test the effectiveness and accuracy of this variational test function method, we will compare these results with those obtained from numerical simulations of the full filament model (2.3). This will be done in the following chapters for several systems with multiple homogeneous steady states (see Sections 4.3, 4.4, 5.5, 6.4 and 6.5). We now present two of the test functions that we shall use in the following chapters to model the solution behaviour in various limits.

3.3 Generic test functions

In order to study the behaviour of the concentration of a tracer that has a bell-shaped profile, we shall use a Gaussian test function, i.e.

$$C(\eta, p_i) = f_0 \exp(-\eta^2), \quad \eta = w\, x\,, \tag{3.6}$$

with $\{p_i\} = \{f_0, w\}$. Here f_0 is the amplitude of $C(\eta, p_i)$ and w is its inverse-width. The tangent space of this test function is spanned by the two basis functions

$$\frac{\partial C}{\partial f_0} = \frac{C}{f_0}, \qquad \frac{\partial C}{\partial w} = \frac{\eta\, C_\eta}{w}\,, \tag{3.7}$$

where C_η is the derivative of C with respect to η. This test function is found to be a good fit to the solution of (2.3) near saddle-node bifurcations (see Chapters 4, 5 and 6). However, we note that solutions with such a profile may be equally well modelled using other bell-shaped functions such as a sech^2 function [26].

If the concentration of a tracer is plateau-like, we shall use the following front-like test function

$$C(\eta, p_i) = \frac{g_0}{2}\left(\tanh\left(\eta + \omega\,\mu\right) - \tanh\left(\eta - \omega\,\mu\right)\right), \quad \eta = \omega\, x\,, \tag{3.8}$$

with $\{p_i\} = \{g_0, \omega, \mu\}$. Again, g_0 is the amplitude of $C(\eta, p_i)$ and ω is its steepness while μ can be understood as the width of the plateau measured from $\eta = 0$ to the turning point ($\partial^2 C/\partial\eta^2 = 0$). The tangent space of this test function is spanned by the three basis functions

$$\begin{aligned} &\frac{\partial C}{\partial g_0} = \frac{C}{g_0}, \qquad \frac{\partial C}{\partial \omega} = \frac{\eta\, C_\eta + \mu\, C_\mu}{\omega}, \\ &\frac{\partial C}{\partial \mu} = \frac{g_0\,\omega}{2}\left(\operatorname{sech}\left(\eta + \omega\,\mu\right)^2 + \operatorname{sech}\left(\eta - \omega\,\mu\right)^2\right). \end{aligned} \tag{3.9}$$

In Fig. 3.1, we see a variety of profiles that can be obtained using this test function. We see that this test function can also be used to describe bell-shaped profiles, and in the following chapters we shall use it to analyze the solution behaviour near saddle-node bifurcations as well.

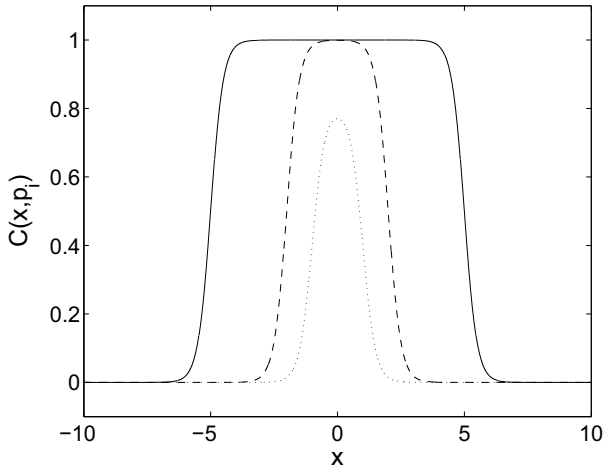

Figure 3.1: The behaviour of a front-like test function (3.8) for three distinct sets of parameters $\{p_i\} = \{g_0, \omega, \mu\}$. The profiles are shown for $\{p_i\} = \{1, 2, 5\}$ (solid line), $\{p_i\} = \{1, 2, 2\}$ (dashed line) and $\{p_i\} = \{0.8, 2, 1\}$ (dotted line).

We shall use the nonperturbative method to investigate the solution behaviour near the bifurcation point and far away from them in several filamental models. Specifically we examine two single component systems, the autocatalytic and bistable systems (Chapter 4), and two multi-component systems, an excitable system (Chapter 5) and a combustion system (Chapter 6).

Chapter 4

One component systems: Autocatalytic and bistable systems

4.1 Introduction

We first examine two one-component systems with multiple homogeneous steady-states. We shall consider an autocatalytic as well as a bistable system. The influence of chaotic stirring on these systems has been recently numerically investigated [83, 88, 113], and it was found that these systems exhibit stationary solutions for a range of values of the Damköhler number Da. In addition, it was observed that nontrivial stationary solutions do not exist below a certain critical value Da_c. However, the solution behaviour near this critical value has not been previously described analytically.

In this chapter we shall use the nonperturbative method introduced in the previous chapter to describe the solution behaviour of these systems near Da_c. In addition, we shall use this method to analyze the system behaviour far from the critical value ($Da \gg Da_c$). The accuracy of these results is tested by comparing them with the corresponding results obtained from the numerical solution of the full system. Part of this work has been published in [91].

We restrict our attention to the steady-state solutions of these systems. However, we note that the nonperturbative method has been successfully used to analyze the time-dependent behaviour of initial perturbations in the bistable system [26].

4.2 Description of the models

The behaviour of autocatalytic and bistable systems in the absence of stirring is well known [98, 97, 60, 142]. These simple systems have been used in various contexts as toy models for the description of unstirred processes such as flame front propagation in combustion systems [22, 126], as well as stirred chemical and biological reactions such as the crystallisation of sodium chlorate in a stirred flow [67, 96, 68], stirred autocatalytic bienzyme reactions [24], and the chlorite-thiosulfate 'clock reaction' [109, 31]. A chaotically stirred autocatalytic system has recently been used to model oceanic plankton distributions [88]. We shall analyse the effect of chaotic stirring on the two systems using the 1-D filament model described in Chapter 2. We now briefly introduce these models.

4.2.1 The autocatalytic system

The autocatalytic reaction $A + B \rightarrow 2B$ has the rate equations [113]

$$\frac{dc_A}{dt} = -r\, c_A\, c_B\,, \quad \frac{dc_B}{dt} = r\, c_A\, c_B\,, \tag{4.1}$$

where c_A and c_B are the number of molecules of the components A and B respectively, and where r is a constant. This system can be described with a variable $c = c_B/(c_A + c_B)$, which has a reaction rate $k\,c\,(1-c)$ where $k = r\,(c_A + c_B)$. This reaction rate can also be understood in the context of population dynamics as a description of logistic growth [98].

This system has two homogeneous solutions: a stable fixed point at $c = 1$ and an unstable one at $c = 0$. When coupled with diffusion, the system exhibits travelling waves with fronts propagating from the stable to the unstable state, and is a prototypical equation for propagation of this kind [163]. The related reaction-diffusion equation is commonly known as the Fisher equation [38] or the Kolmogorov-Petrovsky-Piskunov (KPP) equation [65]. The influence of chaotic stirring on this system can be studied using the following 1-D, one-component model

$$\frac{\partial c}{\partial t} = \frac{\partial^2 c}{\partial x^2} + x\,\frac{\partial c}{\partial x} + Da\, c\,(1-c)\ . \tag{4.2}$$

As discussed in Sec. 2.2, a chaotically stirred system of this type exhibits stationary solutions that arise from the balance between advection and diffusion. We observe that this system has a critical Damköhler number $Da_c = 1$, below which no nontrivial stationary solutions exist. For $Da > Da_c$, the solution splits into two branches: a stable branch of nontrivial solutions and

the trivial solution branch which is unstable. This corresponds to a transcritical bifurcation. The stable stationary solutions of the system (4.2) are shown for a range of Da in Fig. 4.1. The solution profile near the bifurcation point is bell-shaped, and centred on $x = 0$ in accordance with our asymptotic theory of Sec. 2.3. As we approach Da_c, the amplitude of the solution profile goes to zero.

On increasing Da, we observe that the width of the solution profile increases. The amplitude of the solution approaches $c(x) = 1$, and eventually settles around this value. The solution for large values of Da has a well-defined plateau-like profile with flat regions separated by narrow fronts.

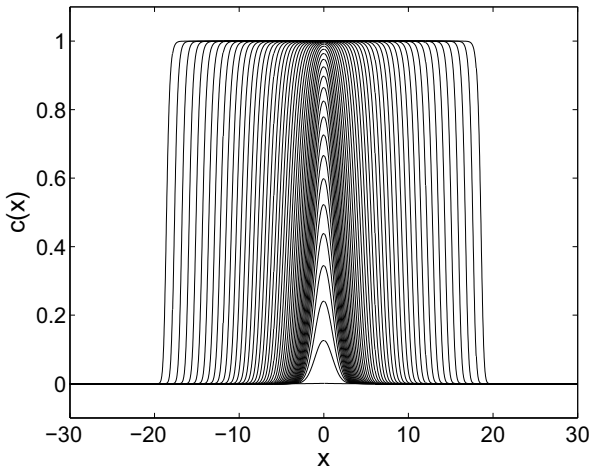

Figure 4.1: The stable stationary solutions of the autocatalytic system (4.2) for 50 logarithmically spaced values of Da between the critical value $Da = 1$ and $Da = 100$.

4.2.2 The bistable system

The second model we shall consider is the bistable system

$$\frac{\partial c}{\partial t} = \frac{\partial^2 c}{\partial x^2} + x\,\frac{\partial c}{\partial x} + Da\,c\,(\alpha - c)\,(c - 1)\ , \tag{4.3}$$

where α is a constant in the range $0 < \alpha < 1$. We first describe the corresponding unstirred system, which is related to the reduced Nagumo equation [108, 98] that has been used in the study of nerve action potentials [87]. The Nagumo equation has a reaction term $\mathcal{F}(c) = (c - c_1)\,(c_2 - c)\,(c - c_3)$, with three homogeneous steady-states c_1, c_2 and c_3. The bistable system has a specific form of this reaction term, with $c_1 = 0$, $c_2 = \alpha$ and $c_3 = 1$.

This system has two stable fixed points at $c = 0$ and $c = 1$ and an unstable one at $c = \alpha$. Here, an initial perturbation which is larger than α over a finite range spreads over the whole domain if $0 < \alpha < 0.5$, and decays to the stable state $c = 0$ if $0.5 < \alpha < 1$. The value $\alpha = 0.5$, for which the velocity of a travelling wave in this system is zero, is known as the Maxwell point.

The chaotically stirred bistable system (4.3) exhibits stationary solutions which we now examine. These are shown for a range of Da in Fig. 4.2. As in the autocatalytic system, the solution profile is bell-shaped near the bifurcation point and plateau-like far away from it, as expected from our asymptotic theory in Sec. 2.3. This system also has a critical Damköhler number, below which nontrivial stationary solutions do not exist. This critical value corresponds to the bifurcation point of a saddle-node. For all values of $Da > Da_c$ we find that a stable stationary solution coexists with an unstable one. The solution at the saddle-node has a nonzero amplitude and as we increase Da the amplitude of the stable solution approaches $c(x) = 1$.

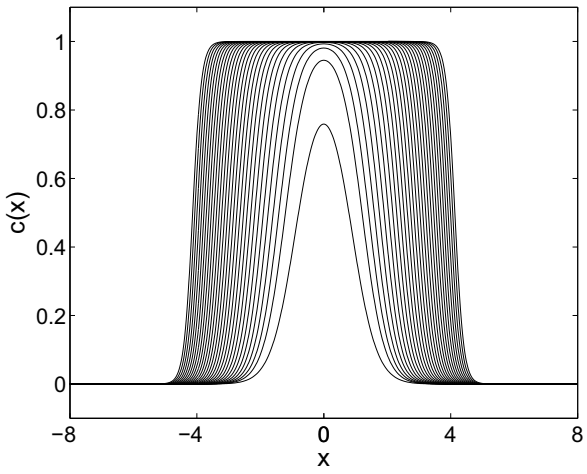

Figure 4.2: The stable stationary solutions of the bistable system (4.3) for 30 logarithmically spaced values of Da between $Da \approx Da_c$ and $Da = 100$.

4.3 The solution near the critical value

In the following we apply the nonperturbative method to describe the solution behaviour near the critical values of the two systems. As seen in the previous section, the solution in this region is bell-shaped. This is in accordance with the asymptotic analysis in the limit of small Da which suggested that

these solutions can be approximated by a Gaussian test function (3.6) near Da_c. As seen in Fig. 3.1, bell-shaped profiles can also be described using the more versatile tanh-based test function (3.8). We shall therefore use the nonperturbative method with both test functions to study this region.

4.3.1 The autocatalytic system

We first consider a Gaussian test function $C(\eta)$ with free parameters $\{p_i\} = \{f_0, w\}$. Restricting the solution space to the subspace of this test function, we obtain

$$w^2 \frac{\partial^2 C}{\partial \eta^2} + \eta \frac{\partial C}{\partial \eta} + Da\, C\,(1 - C) = \varkappa(\eta)\,. \tag{4.4}$$

To minimise the error $\varkappa(\eta)$, we require that (4.4) is orthogonal to the tangent space of $C(\eta)$, which is spanned by (3.7). We therefore have the following two conditions determining the parameters f_0 and w,

$$\langle w^2\, C_{\eta\eta} + \eta\, C_\eta + Da\, C\,(1 - C) \mid C \rangle_\eta = 0\,, \tag{4.5}$$

$$\langle w^2\, C_{\eta\eta} + \eta\, C_\eta + Da\, C\,(1 - C) \mid \eta\, C_\eta \rangle_\eta = 0\,. \tag{4.6}$$

Here we denote $C_\eta = \partial C/\partial\eta$ and $C_{\eta\eta} = \partial^2 C/\partial\eta^2$. We note that for a general function $f(\eta)$ whose spatial derivative vanishes at the boundaries of the domain η (i.e. for fronts or localised pulses), the following relations apply

$$\begin{aligned} \langle f_{\eta\eta}\, f \rangle_\eta &= 2\langle \eta f_{\eta\eta}\, f_\eta \rangle_\eta = -\langle f_\eta^2 \rangle_\eta, \\ \langle \eta\, f_\eta\, f^p \rangle_\eta &= -\frac{1}{p+1} \langle f^{p+1} \rangle_\eta\,. \end{aligned} \tag{4.7}$$

Using these relations, we reduce (4.5) and (4.6) to the single equation

$$-2\,\langle \eta^2 C_\eta^2 \rangle + \left(2\,Da - \frac{1}{2}\right) \langle C^2 \rangle - \frac{5\,Da}{3} \langle C^3 \rangle = 0\,. \tag{4.8}$$

As $C(\eta)$ is chosen to be a Gaussian (3.6), we can explicitly evaluate the following integrals

$$\langle C^p \rangle = f_0^p \sqrt{\frac{\pi}{p}}\,, \qquad \langle C_\eta^2 \rangle = f_0^2 \sqrt{\frac{\pi}{2}}\,, \qquad \langle \eta^2 C_\eta^2 \rangle = \frac{3 f_0^2}{4} \sqrt{\frac{\pi}{2}}\,. \tag{4.9}$$

This allows us to simplify our minimisation condition (4.8), and we obtain two distinct solutions for the amplitude: the trivial solution $f_0 = 0$ and

$$f_0 = \frac{3\sqrt{6}}{5} \left(\frac{Da - 1}{Da}\right)\,. \tag{4.10}$$

Since $f_0 = 0$ at the bifurcation point, we immediately find the value of the critical Damköhler number to be $Da_c = 1$. This corresponds exactly to the numerical observation in Sec. 4.2.1. Below this critical value we have only the trivial solution with $f_0 = 0$.

The parameter w can then be found by substituting (4.10) in either (4.5) or (4.6) to obtain

$$w^2 = \frac{1}{\langle C_\eta^2 \rangle} \left[\left(Da - \frac{1}{2} \right) \langle C^2 \rangle - Da \langle C^3 \rangle \right] , \tag{4.11}$$

where we have substituted the relations (4.7). Using the integrals (4.9), we obtain the expression

$$w = \sqrt{\frac{7 - 2\,Da}{10}} \, . \tag{4.12}$$

From this expression we see that a Gaussian test function is only valid for values of Da in the range $1 \leq Da \leq 3.5$. This is an indication of the fact that as we increase Da, the solution quickly moves away from a bell-shaped profile (as can be seen from the profiles of the numerical solutions in Fig. 4.1).

Next, we consider a tanh-based test function $T(\zeta)$ (3.8) with free parameters $\{q_i\} = \{g_0, \omega, \mu\}$ and where $\zeta = \omega\, x$. The amplitude of such a test function is given by $T(x = 0)$ rather than g_0. Projecting onto the tangent space spanned by the basis functions $\partial T / \partial q_i$, we obtain the conditions

$$\langle \omega^2 T_{\zeta\zeta} + \zeta\, T_\zeta + Da\, T\,(1 - T) \mid \partial T / \partial g_0 \rangle_\zeta = 0 \, , \tag{4.13}$$

$$\langle \omega^2 T_{\zeta\zeta} + \zeta\, T_\zeta + Da\, T\,(1 - T) \mid \partial T / \partial \omega \rangle_\zeta = 0 \, , \tag{4.14}$$

$$\langle \omega^2 T_{\zeta\zeta} + \zeta\, T_\zeta + Da\, T\,(1 - T) \mid \partial T / \partial \mu \rangle_\zeta = 0 \, , \tag{4.15}$$

These equations do not yield explicit formulae for the parameters, and we therefore need to solve them numerically.

The results obtained using the nonperturbative method can be compared with the corresponding numerical results obtained from the solution of the full system (4.2). In Fig. 4.3, we see a comparison between the amplitudes of a Gaussian test function, given by the expression for f_0 (4.10), and for a tanh-based test function, given by $T(x = 0)$ as evaluated from (4.13)-(4.15), with those of the full system. We find that a Gaussian test function is an increasingly good fit to the solution as we approach Da_c. Moreover, such a test function exactly locates the value of the critical Damköhler number $Da_c = 1$. The tanh-based test function is also a good fit to the solution in this regime. As we move away from Da_c we find that the tanh-based test function is much better fit to the solution, which can be explained by the fact that this test function can capture the plateau-like solution profiles observed

for larger values of Da (see Fig. 4.1). We note that in Fig. 4.3 the angle of the nonzero branch at the critical value is not vertical, which is an indication that this bifurcation is transcritical rather than a saddle-node.

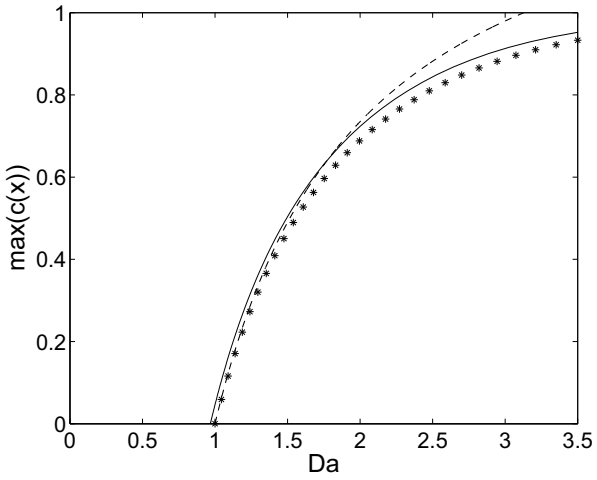

Figure 4.3: Comparison of the amplitude of the stationary solution of the autocatalytic system (4.2), represented by stars, with the corresponding values obtained using the nonperturbative method. We use a Gaussian test function, whose amplitude f_0 is given explicitly by (4.10) (represented by a dashed line), and a tanh-based test function whose amplitude $T(x = 0)$ is obtained numerically from (4.13)-(4.15) (represented by a continuous line).

We illustrate this point in Fig. 4.4, where we superimpose the profile of $c(x)$ obtained from the full system (4.2) with a Gaussian and a tanh-based test function whose parameters are obtained using the nonperturbative method at two values of the Damköhler number. We find that both test functions closely approximate the solution for a value of Da close to the critical value, although the Gaussian test function is a slightly better fit to the solution. For the larger value of Da, the tanh-based test function is a much better fit to the solution than the Gaussian test function. As we move away from the saddle-node and approach $Da = 3.5$, the Gaussian test function is no longer a good approximation as its inverse width approaches zero (see (4.12)).

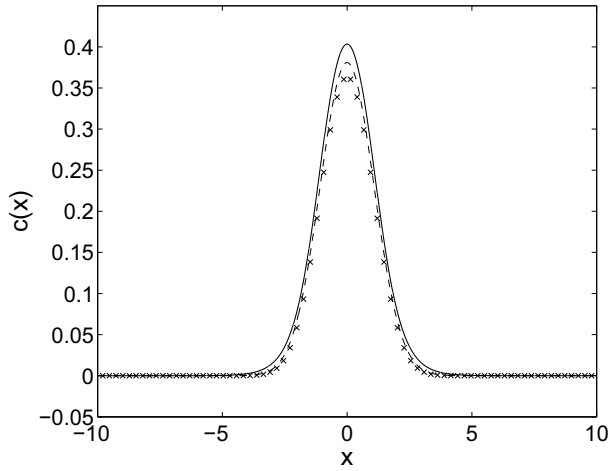

(a)

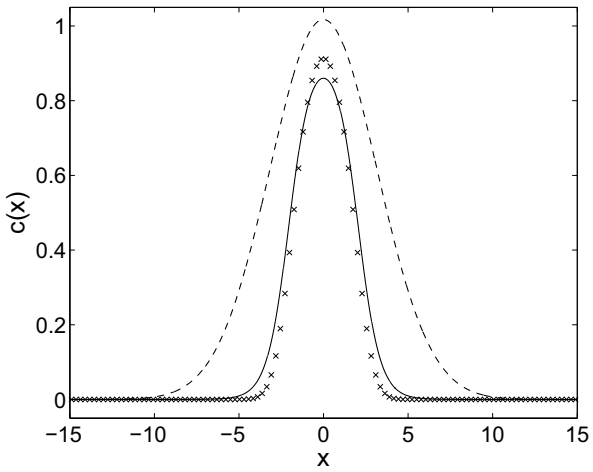

(b)

Figure 4.4: Comparison of the profile of the solution obtained from the numerical solution of the autocatalytic system (4.2), represented by crosses, with two different test functions whose parameters are obtained using the nonperturbative method. We use a Gaussian test function (3.6) whose parameters f_0 and w are given explicitly by (4.10) and (4.12) (represented by a dashed line), and a tanh-based test function (3.8) whose parameters g_0, ω and μ are obtained numerically from (4.13)-(4.15) (represented by a continuous line). (a) $Da = 1.35$. (b) $Da = 3.25$.

4.3.2 The bistable system

We now perform the nonperturbative approach for the chaotically stirred bistable equation close to the saddle-node. We again consider a Gaussian test function $C(\eta)$ with free parameters $\{p_i\} = \{f_0, w\}$. Restricting the solution space to the subspace of this test function, we obtain

$$w^2 \frac{\partial^2 C}{\partial \eta^2} + \eta \frac{\partial C}{\partial \eta} + Da\, C\,(\alpha - C)\,(C-1) = \varkappa(\eta)\,. \tag{4.16}$$

The error $\varkappa(\eta)$ is minimised by projecting (4.16) onto the tangent space spanned by the basis functions (3.7). This gives us the conditions

$$\langle w^2\, C_{\eta\eta} + \eta\, C_\eta + Da\, C\,(\alpha - C)\,(C-1) \mid C\rangle_\eta = 0\,, \tag{4.17}$$

$$\langle w^2\, C_{\eta\eta} + \eta\, C_\eta + Da\, C\,(\alpha - C)\,(C-1) \mid \eta\, C_\eta\rangle_\eta = 0\,. \tag{4.18}$$

Using the relations in (4.7), we reduce the equations (4.17) and (4.18) to the single equation

$$-2\,\langle \eta^2 C_\eta^2\rangle + \frac{5\,Da}{3}\,(1+\alpha)\,\langle C^3\rangle - \left(2\,Da\,\alpha + \frac{1}{2}\right)\langle C^2\rangle - \frac{3\,Da}{2}\langle C^4\rangle = 0\,, \tag{4.19}$$

which upon using the integrals in (4.9), yields the following quadratic equation for the amplitude

$$A\, f_0^2 + B\, f_0 + C = 0\,, \tag{4.20}$$

where

$$A = \frac{3}{4}\,,\quad B = \frac{-5(1+\alpha)}{3\sqrt{3}}\,,\quad C = \frac{\sqrt{2}\,(1 + Da\,\alpha)}{Da}\,. \tag{4.21}$$

This has two solutions f_0, corresponding to stable and unstable branches, which meet at the saddle-node bifurcation. The parameter w can now be found from either (4.17) or (4.18) as

$$w^2 = \frac{1}{\langle C_\eta^2\rangle}\left(\langle \eta\, C_\eta C\rangle + Da\ (1+\alpha)\ \langle C^3\rangle - Da\,\alpha\,\langle C^2\rangle - Da\,\langle C^4\rangle\right)\,, \tag{4.22}$$

which upon evaluating the integrals using (4.9) becomes

$$w = \left[-\frac{1}{2} - Da\left(\frac{f_0^2}{\sqrt{2}} - (1+\alpha)\sqrt{\frac{2}{3}}\, f_0 + \alpha\right)\right]^{1/2}\,, \tag{4.23}$$

where f_0 is given by one of the two solutions of (4.20). We therefore have two values of w corresponding to the two values of f_0.

The critical Damköhler number Da_c for any value of α corresponds to the value of Da where the two solutions of (4.20) coalesce. We therefore solve $B^2 - 4\,A\,C = 0$ to obtain

$$Da_c = \frac{1}{q\,(1+\alpha)^2 - \alpha}\,, \tag{4.24}$$

where $q = 25/(81\sqrt{2})$. From this, we find an upper bound for the value of α, given by

$$\alpha_{max} = \frac{1 - 2\,q - \sqrt{1 - 4\,q}}{2\,q} \approx 0.4744\,. \tag{4.25}$$

This result indicates that chaotic stirring moves the Maxwell point towards smaller values of α. It follows from (4.24) that (4.21) only has solutions for $Da \geq Da_c$.

From (4.23), one finds that imaginary values of w are possible for particular values of Da and α. For $\alpha = 0.2$, we find that we obtain imaginary values for the stable branch of w for all values of Da greater than a critical value $Da \approx 16.208$. Consequently, the test function approach breaks down for the stable branch of the solution at this value.

We now consider a tanh-based test function $T(\zeta)$ (3.8) with free parameters $\{q_i\} = \{g_0, \omega, \mu\}$, and where $\zeta = \omega\,x$. Projecting onto the tangent space of the basis functions, we obtain the conditions

$$\langle \omega^2\,T_{\zeta\zeta} + \zeta\,T_\zeta + Da\,T\,(\alpha - T)\,(T-1) \mid \partial T/\partial g_0 \rangle_\zeta = 0\,, \tag{4.26}$$

$$\langle \omega^2\,T_{\zeta\zeta} + \zeta\,T_\zeta + Da\,T\,(\alpha - T)\,(T-1) \mid \partial T/\partial \omega \rangle_\zeta = 0\,, \tag{4.27}$$

$$\langle \omega^2\,T_{\zeta\zeta} + \zeta\,T_\zeta + Da\,T\,(\alpha - T)\,(T-1) \mid \partial T/\partial \mu \rangle_\zeta = 0\,, \tag{4.28}$$

As in the autocatalytic case, these equations do not yield explicit formulae for the parameters and are therefore solved numerically.

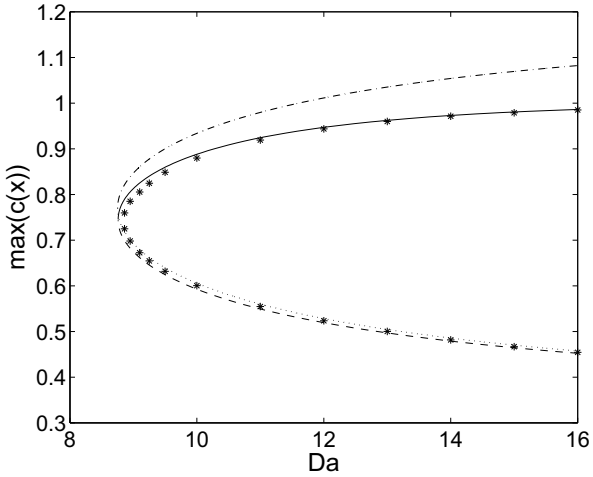

Figure 4.5: Comparison of the amplitudes of the numerically obtained stationary solutions of the bistable system (4.3), represented by stars, with the corresponding values of the amplitude of the test function obtained via the nonperturbative method at $\alpha = 0.2$. The stable and unstable branches of the amplitudes of a Gaussian test function (3.6), obtained explicitly from (4.20)-(4.21), are represented by a dashed-dotted and a dotted line respectively. The stable and unstable branches of the amplitudes of the tanh-based test function (3.8), obtained by numerically solving (4.26)-(4.28), are represented by a continuous and a dashed line respectively

As seen in Fig. 4.5, a Gaussian test function is an excellent fit to the solution along the unstable branch. However it is not as good an approximation for stable solutions in this region. This can be understood from the numerical observation in Sec. 4.2.2 that the stable solutions move away from a bell-shaped profile as we move away from Da_c, while the unstable solutions remain bell-shaped, even for large values of Da. On the other hand, we find that the tanh-based test function (3.8) is an extremely good fit along both branches, which can be understood from the fact that such a test function can approximate both bell-shaped and plateau-like profiles. In Fig. 4.6, we see that both test functions approximate the profile of the stable solution near Da_c well.

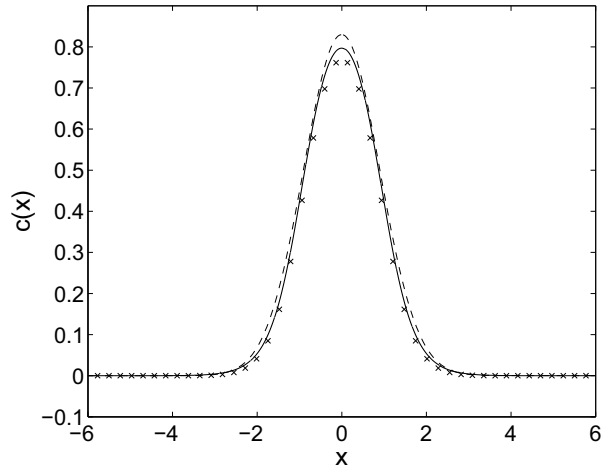

Figure 4.6: Comparison of the profile of the stable steady-state solution obtained from the numerical solution of the bistable system (4.3) at $Da = 8.9$ and $\alpha = 0.2$, represented by crosses, with the profiles of two different test functions with parameters obtained using the nonperturbative method at the same value of Da. A Gaussian test function whose parameters f_0 and w are obtained from (4.20)-(4.21) and (4.23) is represented by a dashed line, while a tanh-based test function (3.8) with parameters obtained by numerically solving (4.26)-(4.28) is represented by a continuous line.

As seen in Fig. 4.7, both the Gaussian test function and the tanh-based test function (3.8) are able to accurately locate the critical Damköhler number of the numerical solution of (4.3). The values of Da_c obtained analytically with the Gaussian test function from (4.24) move away from the numerical results as we approach α_{max}, indicating that the solution profile near the saddle-node moves further away from a Gaussian as we approach the Maxwell point. On the other hand, the values obtained numerically with the tanh-based test function (3.8) remain close to the numerical values over the whole range of α.

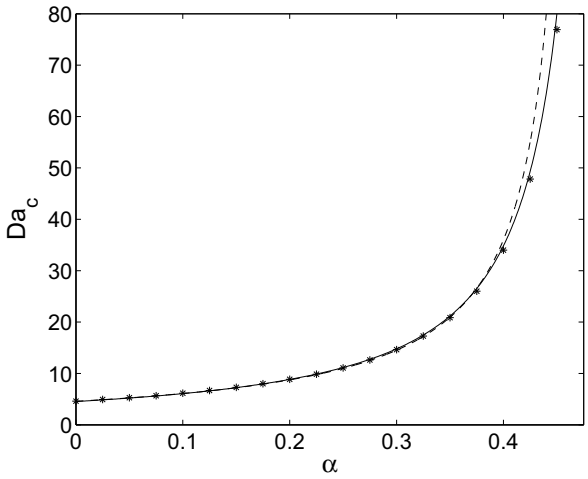

Figure 4.7: Comparison of the values of the critical Damköhler number obtained from a numerical simulation of the bistable system (4.3) with the analytic results for Da_c obtained using the nonperturbative method over a range of α. The results for Da_c obtained using a Gaussian test function (3.6) (from the expression (4.24)) are represented by a dashed line, while the results obtained using a tanh-based test function (3.8) are represented by a continuous line.

4.4 The solution far from the critical value

As discussed in Sec. 2.2, where we performed a general asymptotic analysis of 1-D lamellar reaction-diffusion systems for large Da, the chaotically stirred systems that we have considered behaves asymptotically like the corresponding (rescaled) unstirred system in the limit $Da \to \infty$. In the absence of stirring, both the autocatalytic and bistable system exhibits travelling wave solutions that move outwards with a constant speed. We recall from our phenomenological argument that stirring leads to stationary solutions with fronts located at $x = \pm\mu$, where μ is equal to the corresponding wave velocity. These stationary solutions have a plateau-like profiles and can be approximated using the tanh-based test function (3.8). In this section, we examine the solution behaviour of both systems in the case $Da \gg Da_c$ using the nonperturbative method with such a test function.

4.4.1 The autocatalytic system

We consider a tanh-based test function $T(\zeta)$ (3.8) with free parameters $\{q_i\} = \{g_0, \omega, \mu\}$, and where $\zeta = \omega\, x$. For large Da, the parameter μ represents the width of the solution profile measured from $x = 0$, and ω is its steepness. Restricting the solution space to that of the test function, and projecting onto the tangent space spanned by the basis functions $\partial T/\partial q_i$, we again obtain the conditions (4.13)-(4.15) for the free parameters $\{q_i\}$. As in the previous section, the parameters obtained by this method are those that minimise the error made by this restriction. However, for large Da we find that the solution does not converge. This can be explained by considering the asymptotic limit of large Da, and the phase space of the unstirred equation.

As discussed in Sec. 2.3.1, in the limit $Da \to \infty$ the system behaves like a spatially scaled unstirred system up to order $\mathcal{O}(Da^{-1})$. We first note that far from the critical value, the width μ of the solution profile obtained from the numerical solution of the full system (4.2) scales with $\sqrt{Da}$. The stationary front is therefore assumed to be located at $\mu = \sqrt{Da}\,\bar{\mu}$ where $\bar{\mu}$ is some $\mathcal{O}(1)$ term. As in Chapter 2, we introduce $\xi = \sqrt{Da}(x - \sqrt{Da}\,\bar{\mu})$ to obtain

$$\frac{d^2c}{d\xi^2} + \bar{\mu}\,\frac{dc}{d\xi} + c(1-c) = \mathcal{O}(Da^{-1})\,, \tag{4.29}$$

which is the unstirred system in a scaled spatial variable ξ, in a frame of reference moving with speed $v_0 = \bar{\mu}$.

A linear stability analysis of the system yields the eigenvalues

$$\lambda_\pm = \frac{-\bar{\mu} \pm \sqrt{\bar{\mu}^2 - 4}}{2}\,, \tag{4.30}$$

for the fixed point $(c(\xi), c_\xi(\xi)) = (0, 0)$, and

$$\lambda_\pm = \frac{-\bar{\mu} \pm \sqrt{\bar{\mu}^2 + 4}}{2}\,, \tag{4.31}$$

for the fixed point $(c(\xi), c_\xi(\xi)) = (1, 0)$. The fixed point $(1, 0)$ is a saddle, while $(0, 0)$ is a stable node (with two negative eigenvalues) for all $\bar{\mu} \geq 2$. For $\bar{\mu} < 2$ the fixed point $(0, 0)$ corresponds to a stable spiral.

There is one unique unstable manifold emanating from the saddle $(1, 0)$. However, since there are two stable eigendirections of the stable node $(0, 0)$, there exists a heteroclinic trajectory linking the two fixed points for any choice of the "velocity" $\bar{\mu} \geq 2$, excluding a unique wave speed. The unstirred system therefore exhibits travelling waves whose velocity depend on the initial condition [98]. We illustrate this in Fig. 4.8. Due to this degeneracy, the

nonperturbative method cannot find a unique set of free parameters $\{q_i\}$ for the large Da limit.

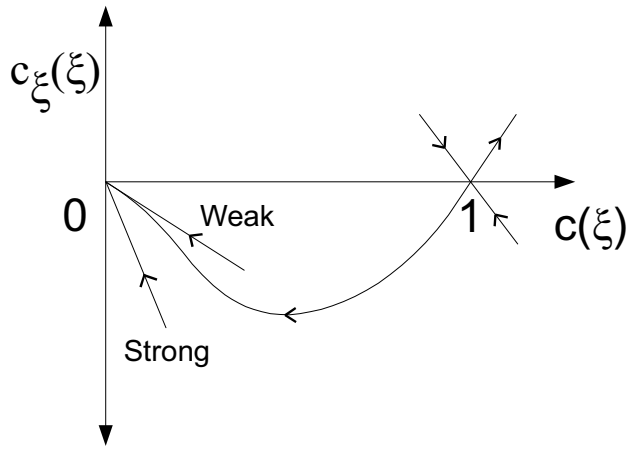

Figure 4.8: Sketch of a possible heteroclinic connection of the phase space of the autocatalytic system. We have a saddle at $(c(\xi), c_\xi(\xi)) = (1, 0)$ and a stable node at $(c(\xi), c_\xi(\xi)) = (0, 0)$. The weak and strong eigendirections of the stable node, as well as the stable and unstable manifolds of the saddle are shown

We may circumvent the problem of the degeneracy by fixing the value of $\bar{\mu}$ in our test function. We require a specific choice of $\bar{\mu}$ which closely approximates the width of the solution for large Da. It is known that for an initial condition with compact support, the unstirred autocatalytic system has travelling wave solutions which move with a constant speed $v_0 = 2$ [65]. As we restrict our attention to solutions that are nonzero within a finite domain, we may assume that the system (4.29) is in a frame of reference moving with this constant speed. We may therefore choose a value $\bar{\mu} = 2$, and shall fix the width of our test function in the original x-coordinate frame to

$$\mu = 2\sqrt{Da}\,. \tag{4.32}$$

The test function $T(\zeta)$ now has only two free parameters g_0 and ω which can be obtained numerically by fixing μ in (4.13)-(4.15).

As we see in Fig. 4.9a, (4.32) is a good approximation to the widths of the solution for large values of Da, thus validating our assumption that the width of the solution scales with $\sqrt{Da}$. A comparison between the results for ω obtained using the test function method (with the phenomenological argument) and the inverse widths of the numerical solutions of (4.2) is shown in Fig. 4.9b. There is a close agreement between the two sets of results. The

amplitudes of the numerical solutions of (4.2) quickly saturate at $c(x) = 1$, and this behaviour is observed from the values of $T(x = 0)$ obtained from the nonperturbative method as well.

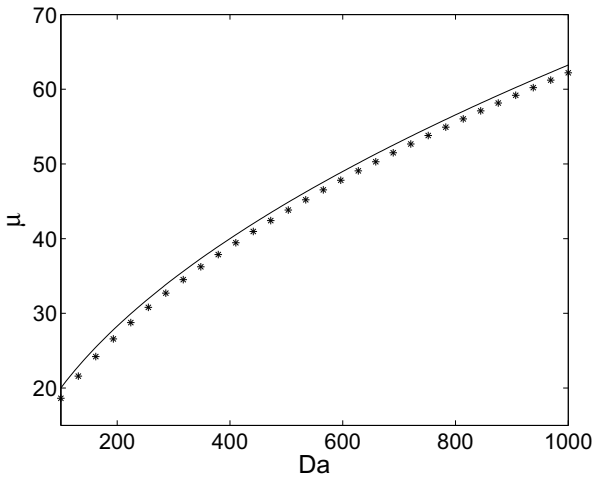

(a)

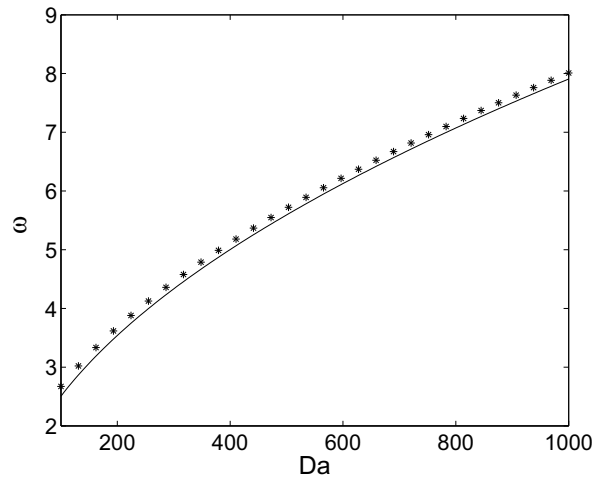

(b)

Figure 4.9: (a) Comparison of the width μ of the stationary solution of the autocatalytic system (4.2), represented by stars, with the phenomenological argument (4.32), represented by a continuous line. (b) Comparison of the inverse width ω of the stationary solutions obtained from the numerical solution of (4.2) with the values of ω obtained from the solution of (4.13)-(4.15) with μ fixed by the phenomenological argument (4.32).

4.4.2 The bistable system

We model the solution behaviour of the bistable system in the large-Da limit using a tanh-based test function $T(\zeta)$ (3.8). We use the same calculations as in Sec. 4.3.2 and solve the system (4.26)-(4.28) numerically to obtain the values of the free parameters $\{q_i\} = \{g_0, \omega, \mu\}$ at any given value of Da. We find that unlike the autocatalytic system, the bistable system does not have a degeneracy. This can be understood as follows.

We find that the width μ of the solution profile obtained from the numerical simulation of the full system (4.3) for $Da \gg Da_c$ scales with $\sqrt{Da}$. As in Sec. 4.4.1, we assume that the stationary front is located at a value $\mu = \sqrt{Da}\,\bar{\mu}$ where $\bar{\mu}$ is some $\mathcal{O}(1)$ term. Introducing the spatial scale $\xi = \sqrt{Da}(x - \sqrt{Da}\,\bar{\mu})$, we obtain

$$\frac{d^2c}{d\xi^2} + \bar{\mu}\,\frac{dc}{d\xi} + c(\alpha - c)(c - 1) = \mathcal{O}(Da^{-1})\,, \tag{4.33}$$

which is the corresponding unstirred system in the scaled variable ξ, in a frame of reference moving with speed $v_0 = \bar{\mu}$.

A linear stability analysis of the system yields the eigenvalues

$$\lambda_\pm = \frac{-\bar{\mu} \pm \sqrt{\bar{\mu}^2 + 4\alpha}}{2}\,, \tag{4.34}$$

for the fixed point $(c(\xi), c_\xi(\xi)) = (0, 0)$, and

$$\lambda_\pm = \frac{-\bar{\mu} \pm \sqrt{\bar{\mu}^2 - 4\alpha\,(1 - \alpha)}}{2}\,, \tag{4.35}$$

for the fixed point $(c(\xi), c_\xi(\xi)) = (\alpha, 0)$, and

$$\lambda_\pm = \frac{-\bar{\mu} \pm \sqrt{\bar{\mu}^2 + 4\,(1 - \alpha)}}{2}\,, \tag{4.36}$$

for the fixed point $(c(\xi), c_\xi(\xi)) = (1, 0)$. For all values of α in the range $0 < \alpha < 1$, the fixed points $(0, 0)$ and $(1, 0)$ are saddles, while $(\alpha, 0)$ is a stable spiral for $\bar{\mu} < 2\sqrt{\alpha\,(1 - \alpha)}$. A heteroclinic connection between the homogeneous steady-states $(0, 0)$ and $(1, 0)$ exists only for a unique value of $\bar{\mu}$. This is since each of these fixed points has a single stable and unstable eigendirection. Consequently, the nonperturbative method will always find a unique set of parameters $\{q_i\}$ for each value of Da.

As seen in Fig. 4.10, the parameters obtained via this method closely match up with the corresponding numerical results found from the simulation of (4.2). We find excellent agreement for both the width μ and the

inverse width ω of the profile. The values of $T(x = 0)$ obtained from the nonperturbative method are found to quickly settle around 1, thus matching the numerical observation well. This test function is therefore a very good approximation to the solution profile in the large Da limit (see Fig. 4.11).

We note that the behaviour of μ is extremely close to what we expect from the phenomenological argument for the location of the steady-state front, which we now describe. In the unstirred case travelling wave solutions move with a constant wave speed $v_0 = \sqrt{2}\,(1/2 - \alpha)$ [98]. In the stirred system the stationary solution is given by the balance between these outward moving fronts and the stirring (for all values of $0 < \alpha < 0.5$). We therefore have the phenomenological argument for the width of the solution

$$\mu = \sqrt{2\,Da}\,(1/2 - \alpha)\ , \tag{4.37}$$

where we have again used the scaling $\mu \sim \sqrt{Da}$. We can therefore fix this value of μ in our test function $T(\zeta)$ to obtain results for g_0 and ω from the nonperturbative method. As seen in Fig. 4.10a, (4.37) is an excellent approximation to the widths of the solution at large Da. The corresponding values of ω also match up well with the numerical results.

The time dependent problem has been analysed in [26], where explicit analytic formulae were found for tanh-solutions.

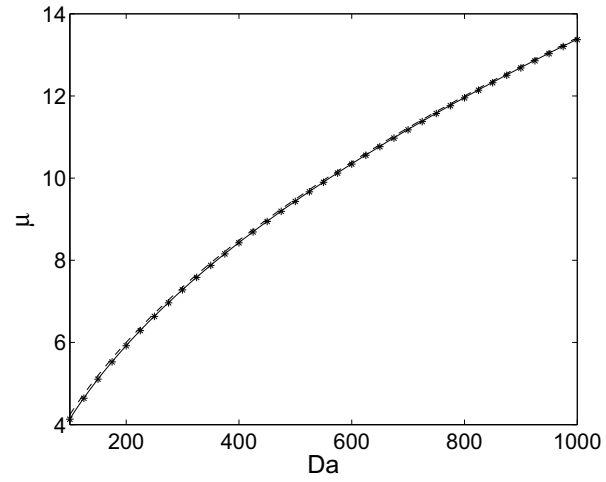

(a)

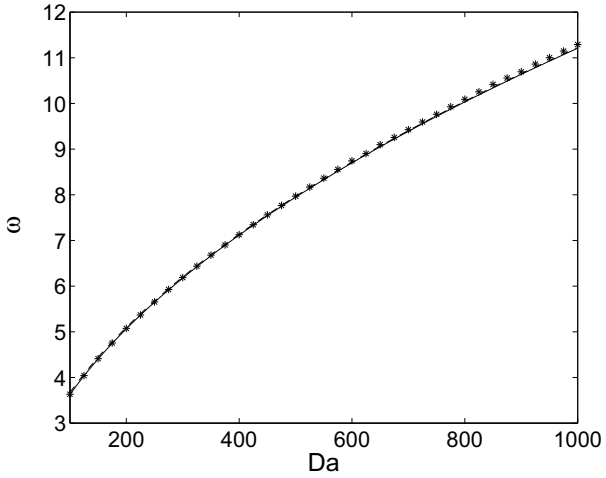

(b)

Figure 4.10: Comparison of the widths of the stationary solution of the bistable system (4.3) for $\alpha = 0.2$, represented by stars, with the corresponding values of the parameters obtained from the nonperturbative method. The values obtained from the numerical solution of (4.26)-(4.28) are represented by a continuous line. The results obtained using the phenomenological argument (4.37) with the nonperturbative method are represented by a dashed line. (a) The width μ of the solution. (b) The inverse width ω of the solution.

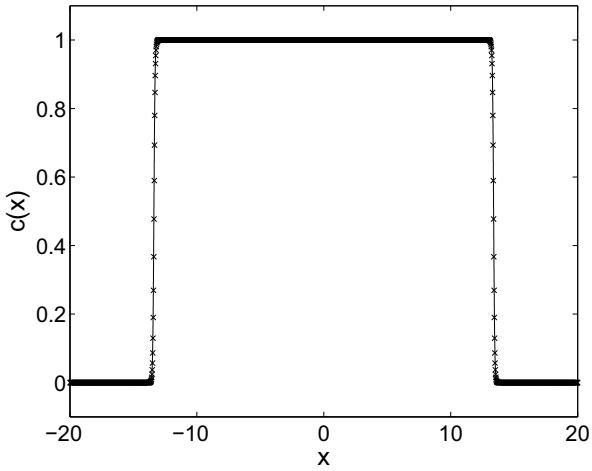

Figure 4.11: Comparison of the profile of the stable steady-state solution obtained from the numerical solution of the bistable system (4.3) for $\alpha = 0.2$, represented by crosses, with a front-like test function whose parameters are obtained from the numerical solution of (4.26)-(4.28), represented by a continuous line, at $Da = 1000$.

4.5 Summary

In this chapter, we studied the effect of chaotic stirring on two one-component models using the 1-D filamental model discussed in Chapter 2. We examined an autocatalytic system as well as a bistable system. The interplay of reaction dynamics with the chaotic stirring leads to stationary fronts in the 1-D model equation corresponding to filaments with a well-defined width in the full 2-D system. In both systems we observe that no nontrivial solutions exist below a sufficiently small value of Da. We applied the nonperturbative technique discussed in Chapter 3 to study the solution near Da_c. We determined the critical Damköhler number and described the solution close to the bifurcation point with good agreement with numerical simulations of the full partial differential equations.

By using a versatile test function which could describe plateau like solutions, we were able to apply the technique to describe fully developed fronts far away from the bifurcation point. However, we ran into a problem for the autocatalytic model for large values of Da. In this limit we find that the conditions given by the variational technique for the free parameters of such a stationary front are degenerate. On using a phenomenological argument

for the width of the solution, we could use the nonperturbative method to describe the autocatalytic model far from Da_c. A comparison with numerical simulations justified our approach.

Chapter 5

Two component systems: Excitable media

5.1 Introduction

Excitable media are abundant in nature, with many examples in biology and chemistry. Examples of excitable media in biological systems include action potential propagation along axons in neural tissue [55], action potential propagation in cardiac tissue [89, 28], cAMP waves in slime moulds [144], calcium waves on the surface of fertilised eggs [73] and plankton dynamics [161, 160]. Examples from chemistry include CO-oxidation on platinum [56] and the Belousov-Zhabotinsky reaction [143, 58]. However excitable media are not restricted to biological and chemical contexts and can be seen in a number of physical systems such as elastic excitable media [16], semiconductor lasers with optical feedback [43] and shock-driven star formation in spiral galaxies [82, 141].

The abundance of excitable media in biological systems is linked to two main characteristics of excitable media. First, excitable media exhibit threshold behaviour. Perturbations below a certain threshold immediately decay back to the rest state, whereas super-threshold perturbations grow and decay back to the rest state only after a long excursion. This is crucial for neural and cardiac systems, for example, which otherwise would constantly fire when triggered by small noisy fluctuations rather than by a large stimulus such as the coordinated stimulation from the sino-atrial node in cardiac dynamics. Second, the decay back to the rest state ensures that the same response of an excitable medium can be expected for a later stimulation, also vital for neural and cardiac function.

In 1-D media pulses and wave trains are generic solutions. It is well known that travelling pulses and wave trains in excitable media exhibit a

saddle-node bifurcation [95]. When approaching the saddle-node by varying a parameter (usually the excitability), the pulse becomes narrower until it becomes too narrow and small to activate the neighbouring medium. This saddle-node bifurcation is responsible for propagation failure in excitable media. Besides the saddle-node, a Hopf bifurcation and a spatial period-doubling bifurcation, which appear close to the saddle-node, were identified as generic bifurcations in excitable media [48].

It has been observed that in addition to this saddle-node relating to propagation failure, a chaotically stirred excitable system exhibits the generic flow-mediated saddle-node bifurcation related to excessive stirring of the system [111, 115, 112, 53]. If the stirring is too strong, the increased thinning of the filaments may again lead to a termination of the reaction for the same reasons as in the propagation failure in excitable media mentioned above. It was observed that the bifurcation scenario of chaotically stirred excitable media was much richer than that of the corresponding unstirred system. However, no systematic analysis of the observed bifurcation scenarios was given.

In this chapter we provide a systematic numerical and theoretical analysis of the bifurcation scenario for chaotically stirred excitable systems. In particular, we examine how the parameter space and the bifurcations are organised by the two different saddle-nodes corresponding to stirring and to the excitability respectively. Using a 1-D filament model (described in Sec. 5.2), we numerically investigate this system (in Sec. 5.3), and describe the various observed solution behaviours. Apart from the saddle-node bifurcations, we observe supercritical and subcritical Hopf bifurcations as well as a region of bistability characterised by a hysteresis loop. We then use the nonperturbative method described in Chapter 3 to obtain analytical conditions that allow us to describe the solution in several regimes of the system (in Sec. 5.4), and shall compare the results obtained via this method with those obtained from the numerical solution of the system (in Sec. 5.5). Part of this work has been submitted for publication [90].

5.2 Description of the model

We shall study the effect of chaotic stirring on an excitable system using the Barkley model [12]

$$\frac{\partial u}{\partial t} = \frac{\partial^2 u}{\partial x^2} + x\,\frac{\partial u}{\partial x} + Da\,u(1-u)(u-u_s-v)\,, \tag{5.1}$$

$$\frac{\partial v}{\partial t} = \delta\,\frac{\partial^2 v}{\partial x^2} + x\,\frac{\partial v}{\partial x} + Da\,\varepsilon\,(u-a\,v)\,, \tag{5.2}$$

where $u(x,t)$ is the activator and $v(x,t)$ is the inhibitor. Here we have used a slightly modified formulation of the Barkley model as in [47], although we expect other 1-D excitable media models such as the Fitzhugh-Nagumo model [39, 108] to behave similarly. Here, δ is the diffusion coefficient of the inhibitor, Da is the Damköhler number of the system, and the excitability parameters are ε, a and u_s. The decay rates towards the stable homogeneous rest state $(u,v) = (0,0)$ along the directions of the activator and inhibitor are determined by u_s and $\varepsilon\, a$ respectively. Note that in the absence of the inhibitor v this equation is a bistable equation. Moreover, the spatially homogeneous model which includes the inhibitor becomes bistable for $a > 1/(1-u_s)$.

In the following we assume $\delta \ll 1$. This case describes chaotically stirred excitable systems where the activator diffuses at a much faster rate than the inhibitor. A physical realisation of this condition may be a chaotically stirred chemical excitable medium such as a stirred Belousov-Zhabotinsky reaction [143, 58] in which the inhibitor is fixed to starch or a gel-like medium. The case $\delta = 0$ is the classic situation in cardiac dynamics. Here the inhibitor consists of (relatively) immobile ion channels. Constant advecting velocities for excitable media in the context of cardiac dynamics is well known for spiral wave drift when subjected to periodic wave trains [69, 32, 164, 49]. An imposed chaotic advecting velocity may be introduced in an analogous way to model the effect of spatially and temporarily random excitations. The source of such random excitations could be either local incoherent stimuli or the cumulative effect of spiral wave chaos.

In contrast to the unstirred system, the chaotically stirred system (5.1)-(5.2) supports stationary solutions (as discussed in Sec. 2.2). These are given by the steady state solutions ($\partial/\partial t = 0$) of the system,

$$\frac{d^2u}{dx^2} + x\,\frac{du}{dx} + Da\,u(1-u)(u-u_s-v) \;=\; 0\,, \tag{5.3}$$

$$\delta\frac{d^2v}{dx^2} + x\,\frac{dv}{dx} + Da\,\varepsilon\,(u - a\,v) \;=\; 0\,. \tag{5.4}$$

In the limiting case $\delta = 0$, the inhibitor $v(x)$ can be explicitly calculated for a given activator $u(x)$ as

$$v(x) = -\frac{2\alpha}{a}x^{2\alpha}\int_{-\infty}^{x}\zeta^{-1-2\alpha}\,u(\zeta)d\zeta\,, \tag{5.5}$$

with $\alpha = Da\,\varepsilon\,a/2$. We consider an infinite domain and require $v(-\infty) = v(\infty) = 0$.

5.3 Numerical simulations of the 1-D filament model

In this Section we present results from a numerical investigation of the full system (5.1)-(5.2). This system exhibits two saddle-nodes, one induced by increasing the excitability ε over a threshold value ε_c for fixed (large enough) Damköhler number, and one induced by the stirring when decreasing the Damköhler number Da below a critical value Da_c for a given (small enough) excitability ε. We therefore study the solution behaviour in the Da-ε parameter space to investigate the effect of stirring and excitability. We find that interesting bifurcations and solution behaviours arise due to the way these two saddle-nodes connect.

We numerically integrate the system (5.1)-(5.2) using a semi-implicit Crank-Nicolson scheme where the nonlinearities are solved by an Adams-Bashforth method. These numerical methods are described in Appendix A. We fix $u_s = 0.1$ for all simulations, and shall use $a = 0$ unless stated otherwise. However, the dynamical scenarios we report are robust with respect to changes in these parameters.

The case of a non-diffusive inhibitor $\delta = 0$ is numerically problematic as it implies a discontinuous derivative of the inhibitor at $x = 0$ when the activator u is a bell-shaped function which is the case near the stirring induced saddle-node. In Fig. 5.1 we illustrate this with a plot of an activator $u(x) = f_0 \exp(-(w\,x)^2)$, whose parameters f_0 and w are chosen so as to approximate the solution in a regime where the activator is bell-shaped, and the corresponding inhibitor $v(x)$ (5.5) for the case $\delta = 0$.

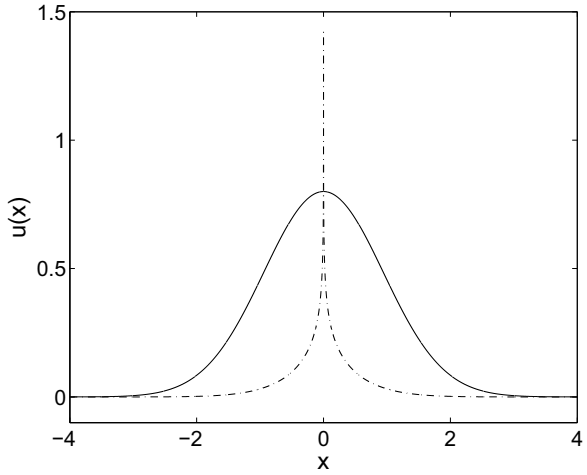

Figure 5.1: Profiles of a Gaussian activator $u(x) = 0.8\exp(-(0.75\,x)^2)$ (represented by a continuous line), which was constructed to closely approximate the numerically obtained stable stationary solution of the full system (5.1)-(5.2) at $Da = 8$, $a = 0$ and $\varepsilon = 0.02$ for $\delta = 0.001$, and the corresponding inhibitor $v(x)$ for the case $\delta = 0$, obtained from the numerical solution of (5.5) (represented by a dashed-dotted line), for the aforementioned values of the system parameters.

We therefore choose for our numerical simulations a value of $\delta = 0.001$ to avoid numerical instabilities. To justify the use of a small nonzero diffusion coefficient, we investigate

$$\rho(\delta) = \left| \sum_j \left(u_{\delta_j} - u_{ref_j} \right) \right|, \tag{5.6}$$

where u_{δ_j} is the stationary solution of $u(x)$ for a specific value of δ at a spatial location $x_j = -L + j\,dx$, and where L and dx represent the box length and grid spacing of our numerical simulation respectively (see Appendix A for more details on the simulations of 1-D filament models). The field u_{ref} is a reference solution for $\delta = 0.00005$. We obtain both solutions by numerically simulating the full set of partial differential equations (5.1)-(5.2) at a specified value of Da and ϵ. In Fig. 5.2 we show that the error $\rho(\delta)$ converges to zero for decreasing δ. This suggests that u_δ approaches the solution of the case $\delta \to 0$.

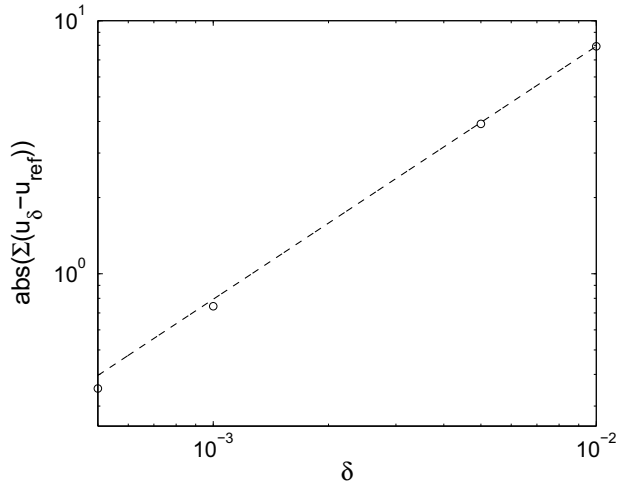

Figure 5.2: Logarithmic plot of $\rho(\delta)$ (5.6) for $Da = 15$ and $\epsilon = 0.01$ (represented by circles). A reference line with slope 1 (represented by a dashed line) is also shown.

A comprehensive picture of the solution behaviour in the Da-ε parameter space is sketched in Fig. 5.3. The profiles of the activator in the various regions of the $Da - \varepsilon$ parameter space are also shown. The results obtained from the full numerical simulation of the system are shown in Fig. 5.4. In the following we explore in detail the different dynamical regions depicted in Figs. 5.3 and 5.4.

In the next section we apply the nonperturbative method to this system, and in Sec. 5.5 we use this method to analyse and describe the observed dynamics. The figure caption of Fig. 5.4 gives an overview of the rich and complex bifurcation behaviour we encounter in this system.

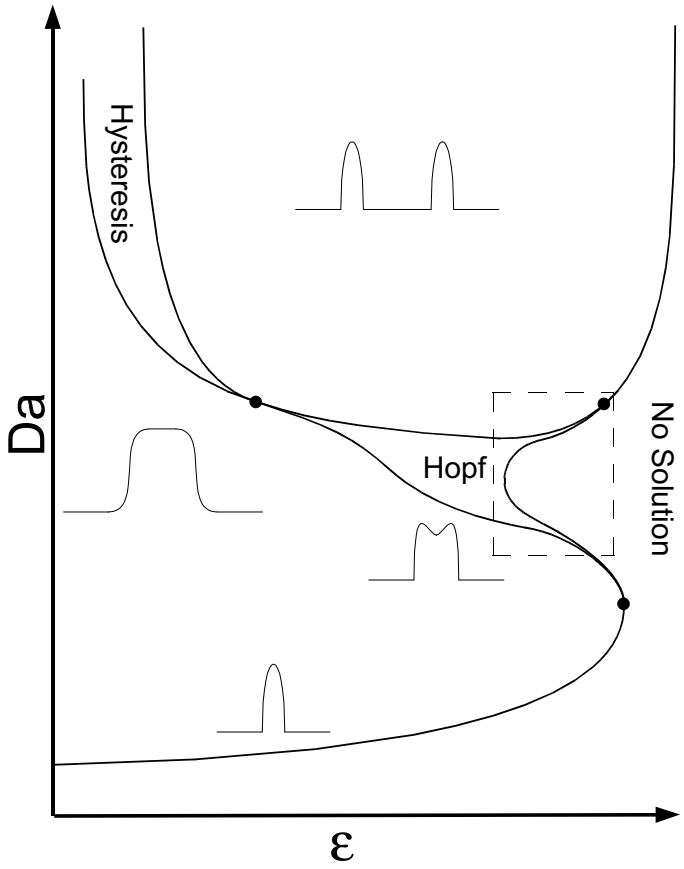

Figure 5.3: Sketch of the behaviour of the system (5.1)-(5.2) in the Da-ε parameter space including the approximate profiles of the activator $u(x)$ in the various regions. The corresponding numerical results are shown in Fig. 5.4. We observe a region of hysteresis (discussed in Sec. 5.3.3) which connects with a region of stable oscillatory solutions arising from a supercritical Hopf bifurcation (discussed in Sec. 5.3.4). The lower and upper stability boundaries correspond to saddle-node bifurcations arising from the stirring (discussed in Sec. 5.3.2) and propagation failure (discussed in Sec. 5.3.1) respectively. The dots represent some of the high codimension points observed in this system. The box encloses a region with a number of different solution behaviours, as well as another high codimension point, which is not detailed in this sketch. The numerical results from this enclosed region are shown in Fig. 5.15.

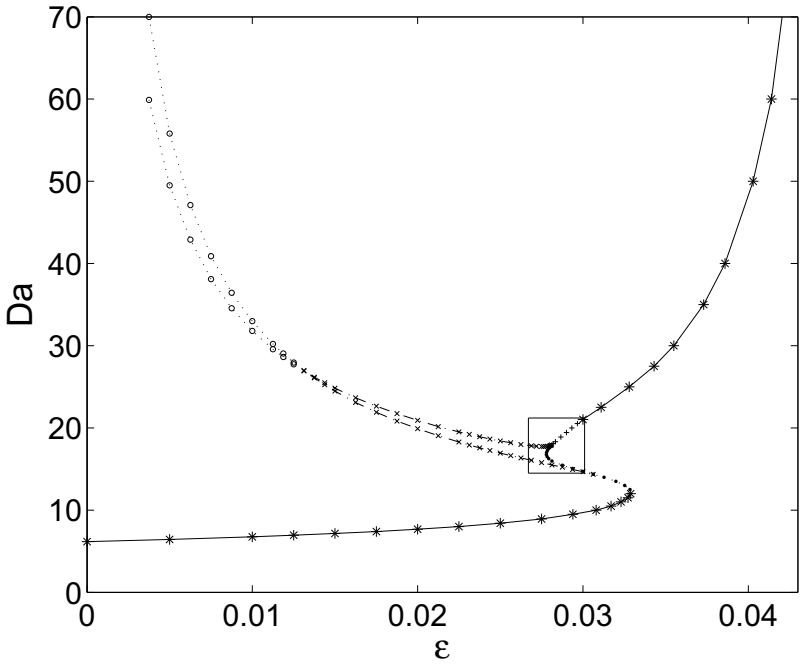

Figure 5.4: Solution behaviour in Da-ε parameter space obtained from the numerical investigation of the system (5.1)-(5.2) for $a = 0$. The lower and upper stability branches, which are represented by stars, correspond to the saddle-node bifurcations arising from the stirring and propagation failure respectively. The branch of the stirring induced saddle-node is found to end at around $\varepsilon \approx 0.0329$, while the branch of the saddle-node due to propagation failure asymptotes for $Da \to \infty$ to $\varepsilon \approx 0.044$, which is the critical value for unstirred media. There are two high codimension points at $\varepsilon_{H_1} = 0.013$ and $\varepsilon_{H_2} \approx 0.028$ which demarcate a region of stable oscillatory solutions arising from a Hopf bifurcation (represented by crosses). In the region $\varepsilon \in (0, \varepsilon_{H_1})$, we find two branches, represented by circles, which enclose a region of hysteresis where two stable stationary solutions coexist. These two branches connect with the two branches of the Hopf bifurcation at $\varepsilon = \varepsilon_{H_1}$. These Hopf branches connect with the lower and upper saddle-node branches in a Bogdanov-Takens bifurcation at $\varepsilon \approx 0.0329$ and $\varepsilon \approx 0.03$ respectively. The box around ε_{H_2} encloses a region with a number of different solution behaviours, which is seen in more detail in Fig. 5.15.

5.3.1 Solution behaviour for large Damköhler numbers

We first discuss the case of large Damköhler numbers. In Section 2.3 we showed that the solution of the stirred system behaves asymptotically like the unstirred system. Far away from the saddle-node, the solution for large Damköhler numbers consists of two well separated pulses as seen in Fig. 5.5.

As discussed in Sec. 2.2, in the limit $Da \to \infty$ the solution of the system behaves asymptotically like the corresponding rescaled unstirred system

$$D_1 \frac{d^2u}{d\xi^2} + \bar{w} \frac{du}{d\xi} + u(1-u)(u-u_s-v) = 0\,, \tag{5.7}$$

$$D_2 \frac{d^2v}{d\xi^2} + \bar{w} \frac{dv}{d\xi} + \varepsilon\,(u - a\,v) = 0\,, \tag{5.8}$$

where $D_{1,2}$ are the diffusion coefficients of the activator and inhibitor respectively and $\bar{w}$ is the speed of the propagating pulse in the scaled variable $\xi = \sqrt{Da}\,x$. We observe that the profiles of these stationary solutions are close to that of the unstirred case when shifted and spatially scaled according to (2.5) (see Fig. 5.6). We find that the profiles of the inhibitor in either case also match up extremely well.

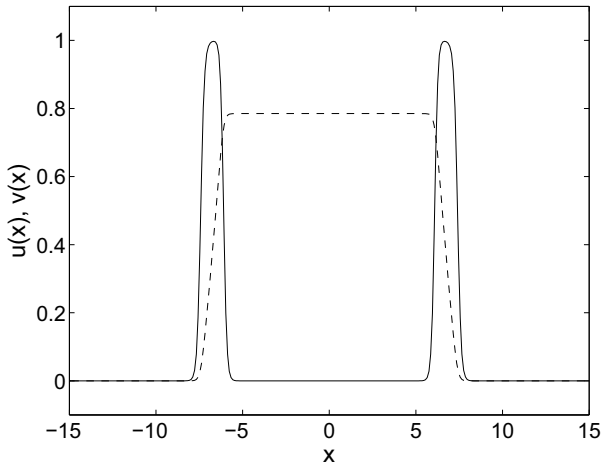

Figure 5.5: Profiles of the stable stationary solutions of the activator $u(x)$ (represented by a continuous line) and the inhibitor $v(x)$ (represented by a dashed line) at $a = 0$, $\varepsilon = 0.02$ and $Da = 200$ obtained from the numerical simulation of (5.1)-(5.2).

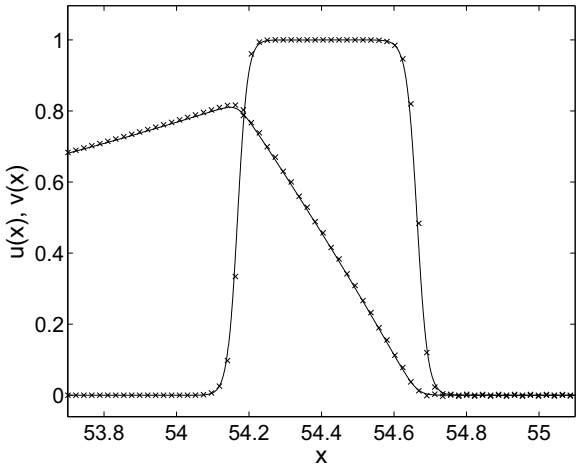

Figure 5.6: Profiles of the stable stationary solutions of the plateau like activator $u(x)$ and the inhibitor $v(x)$ at $Da = 10,000$, $u_s = 0.1$, $a = 0.22$ and $\varepsilon = 0.01$. The crosses depict the solution obtained from the numerical simulation of the stirred system (5.1)-(5.2). The continuous line represents the solution of the unstirred system (5.7)-(5.8) (derived in Sec.5.5.2) at the same parameters, confirming the asymptotic limit for large Da.

Since the system (5.1)-(5.2) behaves for large Damköhler numbers like the unstirred system we expect in this regime the generic saddle-node bifurcation of excitable media [48]. For each sufficiently large Damköhler number there exists a critical value $\varepsilon_c(Da)$ such that there are no solutions for $\varepsilon > \varepsilon_c(Da)$. Close to this saddle-node the solution profile is characterised by two slightly separated bell-shaped pulses centred around $x = 0$ (see Fig. 5.7). As we approach $\varepsilon_c(Da)$, the separation between the two pulses decreases. The stability boundary corresponding to this saddle-node is shown in Fig. 5.4. This saddle-node has been extensively studied [173, 95, 47].

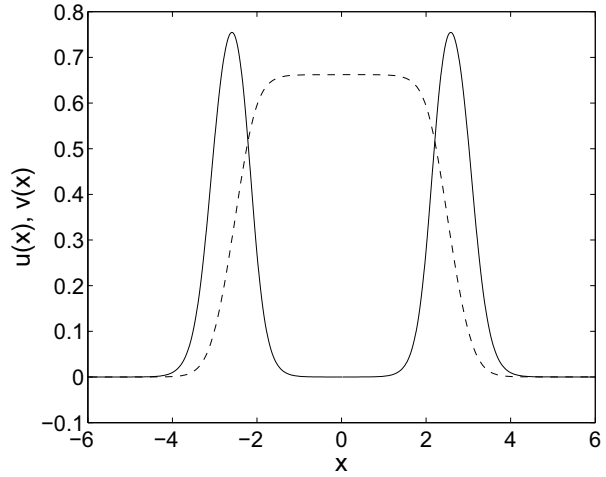

Figure 5.7: Profiles of the stable stationary solutions of the activator $u(x)$ (represented by a continuous line) and the inhibitor $v(x)$ (represented by a dashed line) obtained from the numerical solution of the system (5.1)-(5.2) at $Da = 50$, $\varepsilon = 0.0402$ ($\approx \varepsilon_c(Da)$) and $a = 0$ close to the saddle-node bifurcation arising from propagation failure.

5.3.2 Saddle-node at small Damköhler numbers

Besides the saddle-node for large Damköhler numbers which is inherent to excitable media, an additional saddle-node occurs which is induced by the compressive effects of the stirring. For each $\varepsilon \in (0, 0.0329)$ there exists a critical Damköhler number $Da_c(\varepsilon)$ such that there are no solutions for $Da < Da_c(\varepsilon)$. The stability boundary is shown in Fig. 5.4.

In Fig. 5.8, we see a comparison of the stationary profiles of the activator and inhibitor near Da_c with a Gaussian test function, confirming the asymptotic analysis in Sec. 2.3. For small values of ε near this saddle-node bifurcation, the solution profile of $u(x)$ is approximately bell-shaped for both stable and unstable solutions. Upon increasing Da the solution shape of the stable solution becomes plateau-like, while the unstable solution remains bell-shaped (as seen in Fig. 5.9a). For larger values of ε, the stable and unstable solutions near the saddle-node split into a pair of slightly separated pulses due to the increased influence of the inhibitor $v(x)$. On increasing Da the profiles for both solutions split further into a pair of slightly separated pulses (as seen in Fig. 5.9b). This behaviour has previously been observed in the case of equal diffusion coefficients for activator and inhibitor [53].

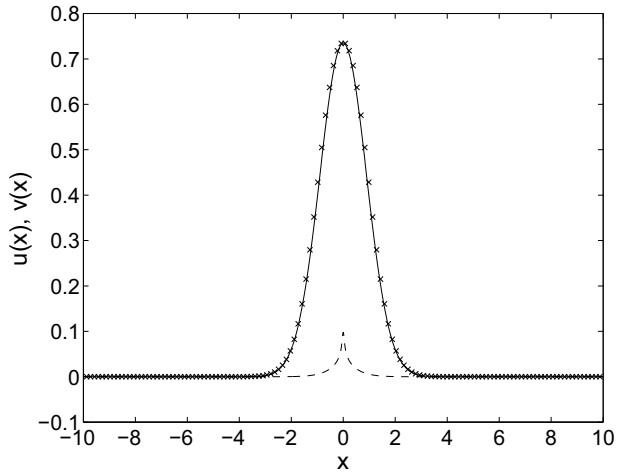

Figure 5.8: Profiles of the stable stationary solutions of the activator $u(x)$ (represented by stars) and the inhibitor $v(x)$ (represented by a dashed line) obtained from the numerical solution of (5.3)-(5.4) at $Da = 6.5$ ($\approx Da_c(\varepsilon)$), $u_s = 0.1$, $a = 0$ and $\varepsilon = 0.005$. A Gaussian fit to $u(x)$ is represented by a continuous line.

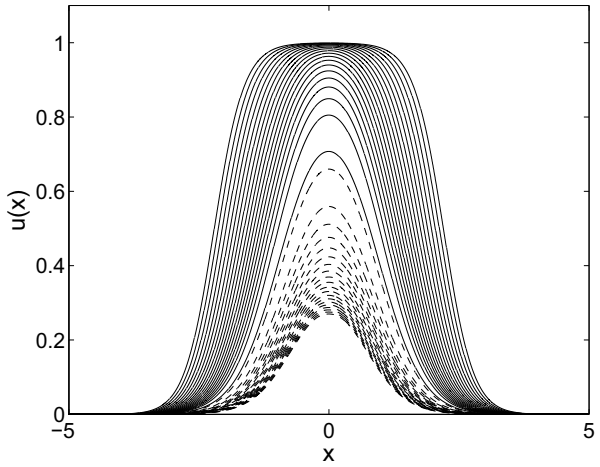

(a)

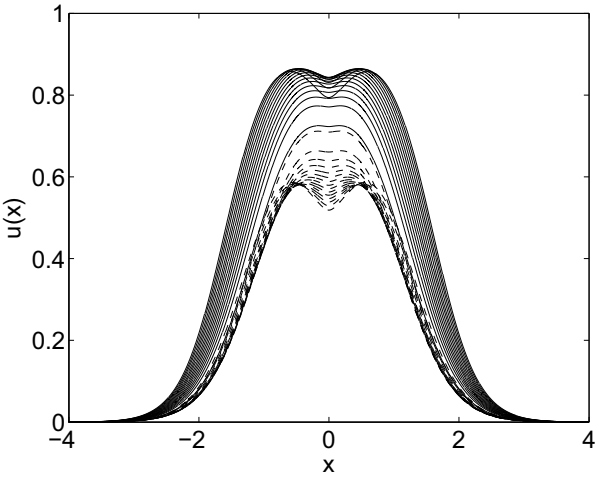

(b)

Figure 5.9: Profiles of the stationary solutions of the activator $u(x)$ obtained from the numerical solution of (5.3)-(5.4) for $a = 0$. Both the stable solutions (represented by continuous lines) and the unstable solutions (represented by dashed lines) are shown for logarithmically spaced values of Da. (a) Profiles for $\varepsilon = 0.005$ for values of Da between $Da = 25$ and $Da = 6.44$ ($\approx Da_c(\varepsilon)$). (b) Profiles for $\varepsilon = 0.03$ for values of Da between $Da = 14$ and $Da = 9.65$ ($\approx Da_c(\varepsilon)$).

5.3.3 The hysteresis loop

At moderate to large Damköhler numbers we observe for $\varepsilon \in (0, 0.013)$ a hysteresis loop between two critical values of the Damköhler number, which we denote as $Da_{hys_1}(\varepsilon)$ and $Da_{hys_2}(\varepsilon)$ for the lower and upper values respectively. In this region, represented by circles in Fig. 5.4, we find that two distinct stable solutions coexist (as shown in Fig. 5.10). For $Da \lesssim Da_{hys_1}(\varepsilon)$ the solution consists of one single pulse centred at $x = 0$, while for $Da \gtrsim Da_{hys_2}(\varepsilon)$ the solution consists of two separated pulses. The hysteresis manifests itself as follows: Increasing the Damköhler number from $Da < Da_{hys_1}(\varepsilon)$ the solution remains plateau-like until $Da = Da_{hys_2}(\varepsilon)$ above which the solution rapidly changes to a pair of two separated plateaus. Conversely, decreasing the Damköhler number from $Da > Da_{hys_2}(\varepsilon)$ a pair of separated plateaus is observed until $Da = Da_{hys_1}(\varepsilon)$ at which point we find a rapid transition to the single plateau-like solution. We find that both Da_{hys_1} and Da_{hys_2} are asymptotic to $\varepsilon = 0$, and the difference between Da_{hys_1} and Da_{hys_2} increases as we approach $\varepsilon = 0$.

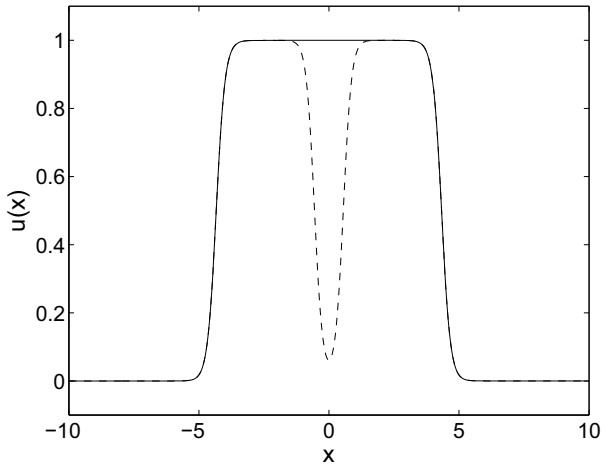

Figure 5.10: Profiles of the two stable stationary solutions of the activator $u(x)$ obtained from the numerical solution of (5.1)-(5.2) at $a = 0$, $\varepsilon = 0.0375$ and $Da = 65$. The solution with a plateau like profile (represented by a continuous line) is obtained using an initial condition with a profile of a stable solution below Da_{hys_1}. The solution with a profile of two separated pulses (represented by a dashed line) is obtained using an initial condition with a profile of a stable solution above Da_{hys_2}.

The existence of a hysteresis loop is robust against changes of the parame-

ters a and u_s, and in fact becomes increasingly pronounced as we approach the bistable limit $a = 1/(1-u_s)$. Comparing the extent of the hysteresis loop in Fig. 5.4 and Fig. 5.11, we see that the difference between the critical values $Da_{hys_1}(\varepsilon)$ and $Da_{hys_2}(\varepsilon)$ for $a = 1$ is much larger than for corresponding values of ε for $a = 0$.

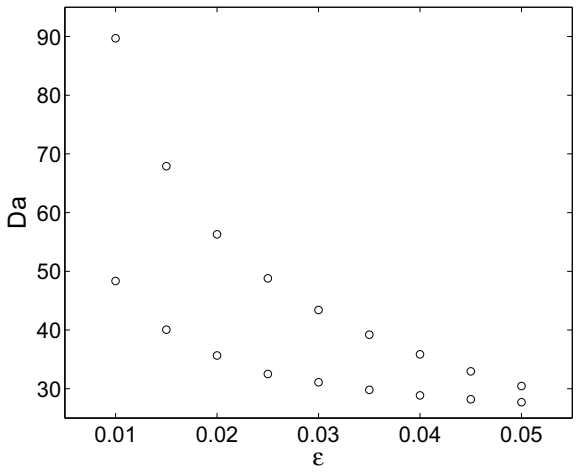

Figure 5.11: The two branches of the hysteresis loop for $a = 1$ in the Da-ε parameter space obtained from the numerical solution of the system (5.1)-(5.2) (represented by circles). A comparison with the corresponding branches seen for $a = 0$ (in Fig. 5.4) shows the effect of increasing a.

The coexistence of two stable solutions in a stirred excitable medium can be explained by the simultaneous limits of $Da \to \infty$, in which the system (5.1)-(5.2) becomes an unstirred excitable medium, and of $\varepsilon \to 0$, in which the system becomes bistable. The two solutions within the hysteresis loop approach the limiting solution types of each limit, with the single plateau-like solution being associated with the bistable equation and the two separated solutions being associated with the unstirred excitable medium.

We note that the term "bistable" is used in two ways. We refer to the hysteresis region, where two stable stationary solutions coexist, as the region of "bistability", whereas we say that this excitable system becomes "bistable" in the limits $a \to 1/(1-u_s)$ or $\epsilon \to 0$, where the observed solution behaviour is that of the bistable system (whose behaviour has been described in Chapter 4).

5.3.4 The Hopf bifurcation

For moderate Damköhler numbers and $\varepsilon \in (0.013, 0.03)$ we observe stable oscillations. For fixed ε the oscillations occur for a finite range of Damköhler numbers between Da_{H_1} and $Da_{H_2} > Da_{H_1}$. Unlike in unstirred excitable media these oscillations arise through a supercritical Hopf bifurcation [48].

The Hopf bifurcation is mediated through the interaction of the inhibitors of the two pulses across the $x = 0$ centre. Close to the Hopf bifurcation the solution consists of two closely neighbouring pulses (see Fig. 5.12). At $\varepsilon = 0.013$ the region of stable oscillations connects with the hysteresis loop in a higher codimension bifurcation. At larger values of ε the Hopf bifurcation connects in two Bogdanov-Takens bifurcations with the saddle-nodes described above (see Fig. 5.15).

In Fig. 5.13 we show the time periodic amplitudes for different values of ε and Da. We see clearly that when approaching the high-codimension point at $\varepsilon = 0.013$, where the Hopf bifurcation coalesces with the hysteresis loop, the period of the oscillations diverge indicating a homoclinic bifurcation. In Fig. 5.14, the profiles of the solution of $u(x)$ at the crest and trough of the oscillations in Fig. 5.13 are shown. We see that the outer sides of the solution are virtually unaffected during the oscillations, while the region near the origin at $x = 0$ changes significantly, indicating the weak interaction with the tails of the inhibitor.

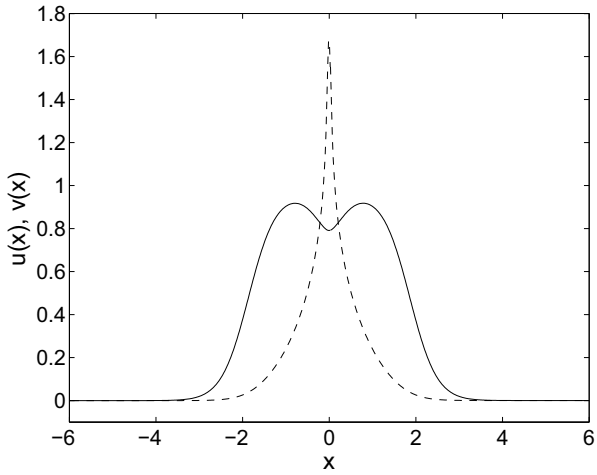

(a)

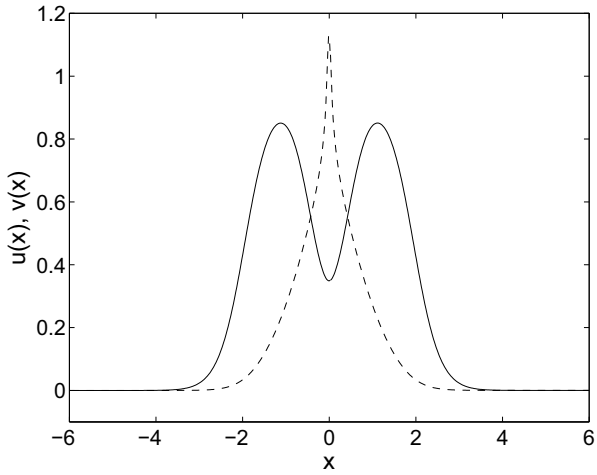

(b)

Figure 5.12: Profiles of the stable stationary solutions of the activator $u(x)$ (represented by a continuous line) and the inhibitor $v(x)$ (represented by a dashed line) obtained from the numerical solution of the system (5.1)-(5.2) at $a = 0$, $\varepsilon = 0.025$ close to the Hopf bifurcations. (a) Profiles at $Da = 16.9 \lesssim Da_{H_1}$. (b) Profiles at $Da = 18.5 \gtrsim Da_{H_2}$.

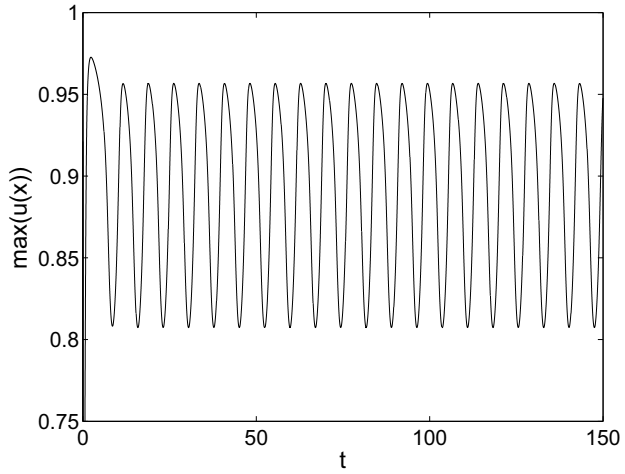

(a)

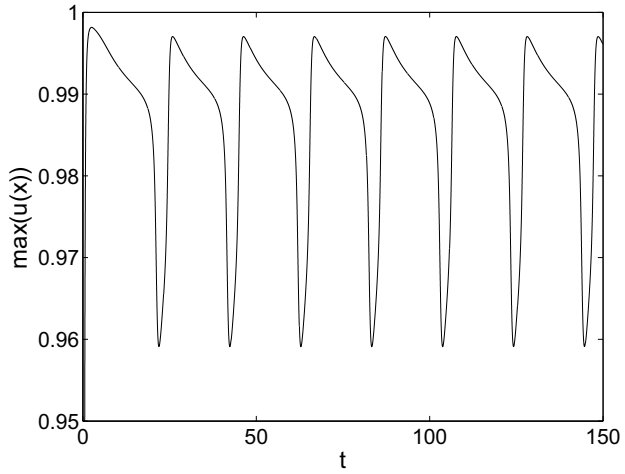

(b)

Figure 5.13: Behaviour of the maximal amplitude of the stable oscillatory solution of the activator $u(x)$ as a function of time, obtained from the numerical solution of (5.1)-(5.2), at $a = 0$. Note the transient behaviour at the beginning and the fast convergence to the solution. (a) Maximal amplitude behaviour for $\varepsilon = 0.025$, $Da = 17.5$. (b) Maximal amplitude behaviour for $\varepsilon = 0.015$, $Da = 24.5$.

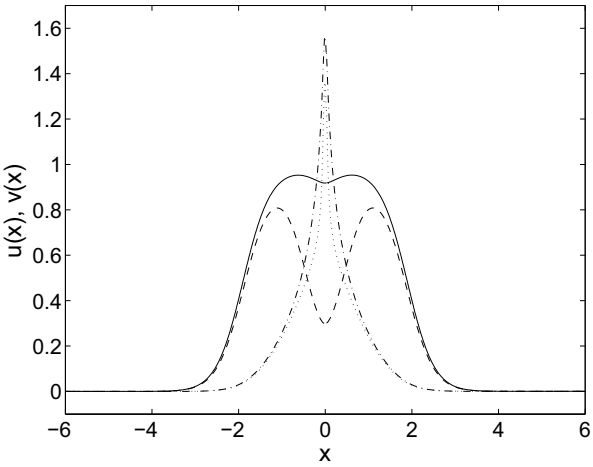

Figure 5.14: Snapshots in time of the profiles of the stable oscillatory solutions of the activator $u(x)$ and the inhibitor $v(x)$, obtained from the numerical solution of (5.1)-(5.2) at $a = 0$, $\varepsilon = 0.025$ and $Da = 17.5$. The profiles of $u(x)/v(x)$ are shown at the crest (continuous/dashed-dotted line) and trough (dashed/dotted line) of the oscillation of the solution represented in Fig. 5.13.

5.3.5 The bifurcation scenario near the high codimension points

In the region where the Hopf bifurcation coalesces with the saddle-node bifurcations we observe a complex unfolding of bifurcations, as illustrated in Fig. 5.15. In this region we observe two Bogdanov-Takens points where the two branches of the Hopf bifurcation meet the two saddle-node branches. We find that a number of different solution behaviours are possible in this region, and here we present some of the main observed behaviours. We note that this list is non-exhaustive, and we expect that this system exhibits even more regions of different solution behaviour near the high-codimension points.

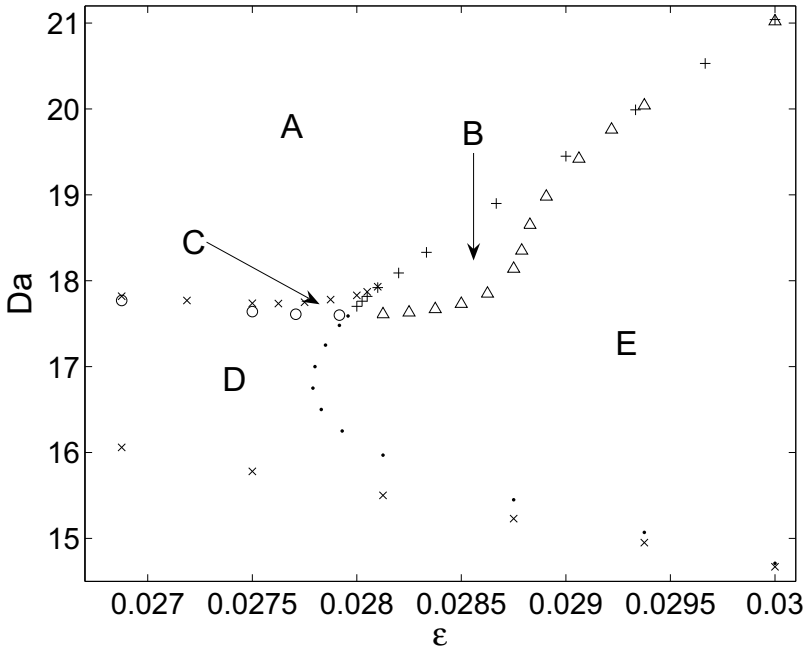

Figure 5.15: Close up of the region $\varepsilon \in (0.0265, 0.031)$ of the $Da-\varepsilon$ parameter space shown in Fig. 5.4. Region A contains stable stationary solutions, region D contains stable oscillatory solutions and region E contains no solutions (these three regions have been depicted in Fig. 5.4). The branches of a supercritical Hopf bifurcation are represented by crosses. In region B we have a strong dependence on initial conditions. At the stability boundary between regions B and E (represented by triangles), we observe a subcritical Hopf bifurcation. In region C, we find that stable stationary solutions coexist with stable oscillatory solutions. At the boundary between regions C and D (represented by circles) we observe a second supercritical Hopf bifurcation. The oscillatory solutions in D and C flatten out to $u = 0$ in a homoclinic bifurcation represented by plus signs and dots respectively.

We first note that near $\varepsilon \approx 0.028$ a small region exists where stable oscillatory solutions coexist with stable stationary solutions. This region of bistability is labelled C in Fig. 5.15 and is characterised by a hysteresis loop. If we start with the profile of the stable stationary solution obtained at a value of Da just above this region (i.e. from region A in Fig. 5.15), then we obtain stable stationary solutions within region C. If, on the other hand, we start with the profile of a snapshot of the stable oscillatory solution obtained at a value of Da just below this region (i.e. from region D in Fig. 5.15), then

we obtain stable oscillatory solutions within the region C. So in fact, region C exhibits bistability where for every value of Da and ε, the stable solution behaviour is either stationary or oscillatory.

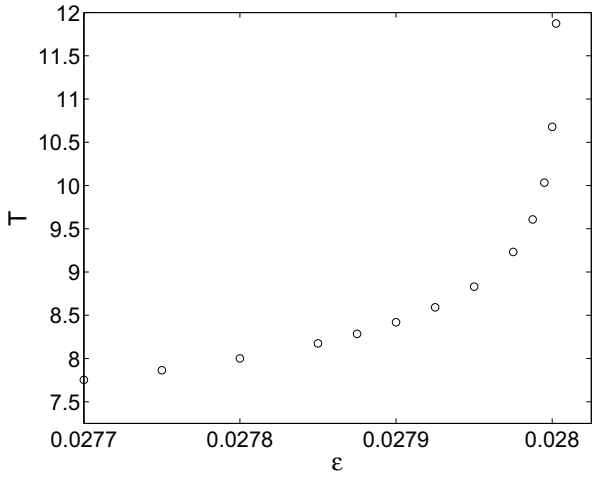

Figure 5.16: Time periods T of the stable oscillatory solutions in region C of Fig. 5.15 at $Da = 17.7$, obtained from the numerical solution of the full system (5.1)-(5.2) (represented by circles).

Next to this region of bistability, we find a region labelled B in Fig. 5.15 in which the observed solution behaviour again depends strongly on the initial condition. If we start with the profile of the stable stationary solution obtained at a value of Da just above this region (i.e. from region A), we obtain stable stationary solutions in this region. If we start from region C, then the observed behaviour depends on the nature of the solution type as described above. Specifically, if the initial condition is that of the stable stationary solution in C, the solution behaviour in B is also stable and stationary. On the other hand, if we choose an initial condition given by the profile of a stable oscillatory solution in C, then we find that the solution flattens out to $u = 0$ as we cross the boundary between the two regions. This is indicative of a homoclinic bifurcation, which is seen from the fact that the time periods of the oscillations in region C rapidly increase close to the boundary with B (see Fig. 5.16).

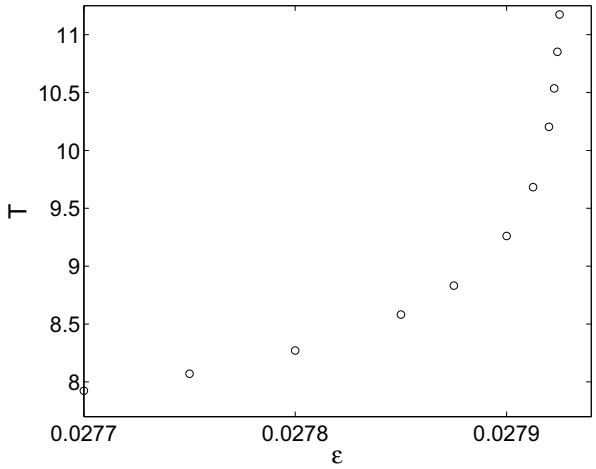

Figure 5.17: Time periods T of the stable oscillatory solutions in region D of Fig. 5.15 at $Da = 17.5$, obtained from the numerical solution of the full system (5.1)-(5.2) (represented by circles).

We further observe that region B has a stability boundary with region E where no solutions are observed. As we move from B to E we observe that the solution flattens out to $u = 0$ via a subcritical Hopf bifurcation. This is reminiscent of the generic case in unstirred excitable systems for weakly interacting pulses [46]. As we move from region D to E we see that the time period of the oscillations increases rapidly, and the solution goes to zero. This is again indicative of a homoclinic bifurcation (see Fig. 5.17). The two homoclinic bifurcations, i.e between D and E and between C and B, join up at the high codimension point $\varepsilon \approx 0.028$. The homoclinic bifurcation branches between C and B coalesces with the subcritical Hopf bifurcation as well as the saddle-node branch of the propagation failure at $\varepsilon \approx 0.03$. We also find that the homoclinic bifurcation branch between D and E coalesces with the lower branch of the supercritical Hopf bifurcations, Da_{H_1}, and the saddle-node branch due to stirring at a Bogdanov-Takens point $\varepsilon \approx 0.0329$.

5.4 Analysis using the nonperturbative variational method

We use the nonperturbative method described in Chapter 3 to study the solution behaviour of the activator and inhibitor in various regimes of the $Da - \varepsilon$ parameter space. We restrict the solution space to that of the general

test functions

$$u(x,t) = U(x, p_i(t))\,, \quad i = 1, \ldots, n\,, \tag{5.9}$$

$$v(x,t) = V(x, q_j(t))\,, \quad j = 1, \ldots, m\,, \tag{5.10}$$

where U and V are parameterised by $p_i(t)$ and $q_j(t)$ respectively. The tangent space of these test functions is spanned by the basis functions $\partial U/\partial p_i$ and $\partial V/\partial q_j$. We determine the parameters by setting the condition that the error made by restricting our solution space to the subspace of the test function is orthogonal to the tangent space. We therefore have the following conditions

$$\langle -U_t + U_{xx} + x\,U_x + Da\,U(1-U)(U - u_s - V) \mid \partial U/\partial p_i \rangle_x = 0\,, \tag{5.11}$$

$$\langle -V_t + \delta\,V_{xx} + x\,V_x + Da\,\varepsilon\,(U - a\,V) \mid \partial V/\partial q_j \rangle_x = 0\,. \tag{5.12}$$

To study the time-dependent behaviour of the solution, we substitute the derivatives

$$\frac{\partial U}{\partial t} = \sum_{i=1}^{n} \frac{\partial U}{\partial p_i}\,\dot{p}_i\,, \qquad \frac{\partial V}{\partial t} = \sum_{j=1}^{m} \frac{\partial V}{\partial q_j}\,\dot{q}_j\,, \tag{5.13}$$

into (5.11)-(5.12) to get a system of $m + n$ coupled ordinary differential equations for $p_i(t)$ and $q_j(t)$.

The behaviour of the stationary solutions in the various regions can be studied by taking $\partial/\partial t = 0$ in (5.11)-(5.12). In this case, we can find the stationary solution of the inhibitor explicitly in terms of the activator from (5.4). Moreover, as we are interested in the limit of slow diffusion of the inhibitor, we can explicitly find $v(x)$ in terms of $u(x)$ from (5.5) by considering $\delta = 0$. We can therefore describe the stationary solutions using a single test function U, and find its parameters from the single condition (5.11).

We use two different test function types to study the behaviour of this system. Near the saddle-node arising from stirring, the activator profile is bell shaped, as described in Sec. 5.3.2. From the asymptotic analysis in the limit of small Da, we find that the solution can be approximated by a Gaussian (see Sec. 2.2). This motivates the use of a Gaussian test function

$$U(\eta, t) = f_0(t)\exp(-\eta^2) \qquad \text{with} \qquad \eta = w(t)\,x\,, \tag{5.14}$$

with free parameters $\{p_i\} = \{f_0, w\}$, where f_0 is the amplitude and w is the inverse pulse width. The tangent space of this test function is spanned by

$$\frac{\partial U}{\partial f_0} = \frac{1}{f_0}\,U \qquad \text{and} \qquad \frac{\partial U}{\partial w} = \frac{1}{w}\,\eta\,U'\,. \tag{5.15}$$

As we shall see in Sec. 5.5.3 (and as detailed in Appendix B), for such a test function we can find an exact expression for V in the stationary case and we can obtain explicit analytic formulae for the parameters.

The other test function that we shall use is

$$\begin{aligned} U(\eta,t) = \frac{g_0}{2}\,&(\tanh\left(\eta-\omega(\mu-\nu)\right)+\tanh\left(\eta+\omega(\mu+\nu)\right) \\ &-\tanh\left(\eta-\omega(\mu+\nu)\right)-\tanh\left(\eta+\omega(\mu-\nu)\right))\ , \end{aligned} \tag{5.16}$$

where the parameters are $\{p_i\} = \{g_0, \omega, \nu, \mu\}$ and $\eta = \omega\, x$, and which has basis functions

$$\begin{aligned} \frac{\partial U}{\partial g_0} &= \frac{1}{g_0}U\ , \quad \frac{\partial U}{\partial \nu} = \frac{g_0\,\omega}{2}\left(s_1+s_2+s_3+s_4\right)\ , \\ \frac{\partial U}{\partial \mu} &= \frac{g_0\,\omega}{2}\left(-s_1+s_2+s_3-s_4\right)\ , \\ \frac{\partial U}{\partial \omega} &= \frac{g_0}{2\omega}\left((\eta-\omega(\mu-\nu))s_1^2-(\eta-\omega(\mu+\nu))s_2^2\right. \\ &\qquad \left.+(\eta+\omega(\mu+\nu))s_3^2-(\eta+\omega(\mu-\nu))s_4^2\right)\ , \end{aligned} \tag{5.17}$$

where $s_1 = \mathrm{sech}^2(\eta-\omega(\mu-\nu))$, $s_2 = \mathrm{sech}^2(\eta-\omega(\mu+\nu))$, $s_3 = \mathrm{sech}^2(\eta+\omega(\mu+\nu))$ and $s_4 = \mathrm{sech}^2(\eta+\omega(\mu-\nu))$. This test function can describe a variety of profiles, and can in fact be used to approximate almost all solution behaviours observed in Section 5.3, as illustrated in Figs. 5.18 and 5.19. We note that such a test function is particularly useful for the description of the time-varying profile of the solution in the region near the Hopf bifurcation. Here the solution shape resembles that of two slightly separated pulses which, as seen in Fig. 5.19, can be well approximated by such a test function.

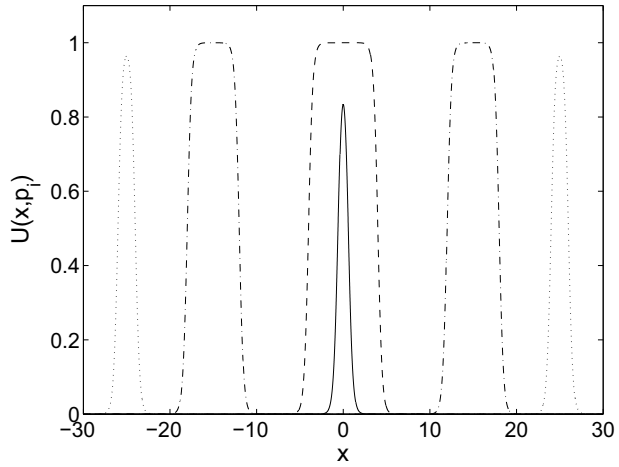

Figure 5.18: Examples of the types of profiles that can be obtained using the test function (5.16) with different values of the parameters $\{p_i\} = \{f_0, \omega, \nu, \mu\}$, which can approximate the solution behaviour close to (and far away from) the saddle-node due to stirring. Profiles are displayed for $\{p_i\} = \{1, 2, 0.3, 0.3\}$ (pulse-like shape represented by a continuous line), $\{p_i\} = \{1, 2, 2, 2\}$ (plateau like shape represented by a dashed line), $\{p_i\} = \{1, 2, 3, 15\}$ ("double-plateau" shape represented by a dashed-dotted line) and $\{p_i\} = \{1, 2, 1, 25\}$ ("double-bell" shape represented by a dotted line).

The parameter ω of the test function (5.16) measures the steepness of the profile, while μ and ν can be understood by considering the case where the test function describes two separated pulses (illustrated in Fig. 5.18). Here, μ is the distance of the maximal amplitudes of each of the pulses from $x = 0$, and ν is the half-width at half-maximum of each pulse. The maximal amplitude of each pulse is given by $U(\mu, t)$. For such a test function, we calculate V numerically from (5.5). However, as we shall discuss in Sec. 5.5.5, to analyse the time-varying behaviour of the solution near the Hopf bifurcation, we shall in fact use a test function to approximate V and solve the full system (5.11)-(5.12). In the next section we use this method to analyse the solution behaviour in various regions of the $Da - \varepsilon$ parameter space.

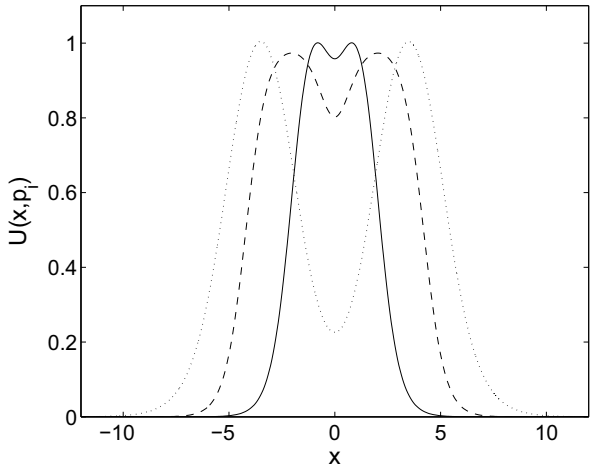

Figure 5.19: Examples of the types of profiles that can be obtained using the test function (5.16) with different values of the parameters $\{p_i\} = \{f_0, \omega, \nu, \mu\}$, which can approximate the solution behaviour near the Hopf bifurcations. Profiles are displayed for $\{p_i\} = \{1.25, 1, 0.9, 1.1\}$ (continuous line), $\{p_i\} = \{1, 1, 2, 2.2\}$ (dashed line) and $\{p_i\} = \{1.4, 0.6, 1.5, 3.5\}$ (dotted line).

5.5 Results obtained with the nonperturbative variational method

In this section we compare the results obtained using the nonperturbative method with those obtained from the numerical solution of the full system (5.1)-(5.2) and its steady-state formulation (5.3)-(5.4), as presented in Sec. 5.3. We use the nonperturbative method to study the solution behaviour for large Damköhler numbers, the saddle-node associated with propagation failure (seen for large values of Da), the stirring-induced saddle-node (seen for small values of Da) and the hysteresis loop (seen for low ε). The Hopf bifurcation is analyzed by a time-dependent version of the nonperturbative method.

5.5.1 Solutions far from the saddle-node

For large enough values of Da the solution of (5.1)-(5.2) consists of two stationary pulses, symmetric around $x = 0$, as discussed in Sec. 5.3.1 (and as illustrated in Fig. 5.5). Far away from the saddle-node reported in Sec-

tion 5.3, for small values of ε the pulses consist of a plateau, while for larger values of ε approaching $\varepsilon_c(Da)$ they become bell-shaped. We perform the nonperturbative variational approach using the tanh-based test function U (5.16) which is able to capture both solution types. We numerically solve the four algebraic equations for the projections (5.11) to obtain values of the parameters $\{g_0, \omega, \mu, \nu\}$. In Fig. 5.20, we show a comparison of these results with numerical results of the full system (5.1)-(5.2). Fig. 5.20a reveals that in the limit $Da \to \infty$ the amplitude approaches the constant value 0.9989, corresponding to the amplitude of the unstirred system. (Note that the maximal amplitude of the tanh-based test function (5.16) is not given by g_0 but rather by $U(x = \mu)$. The distance from the centre $x = 0$ is roughly measured by μ which scales with $\sqrt{Da}$, as illustrated in Fig. 5.20b, consistent with the asymptotic theory of Section 2.3.

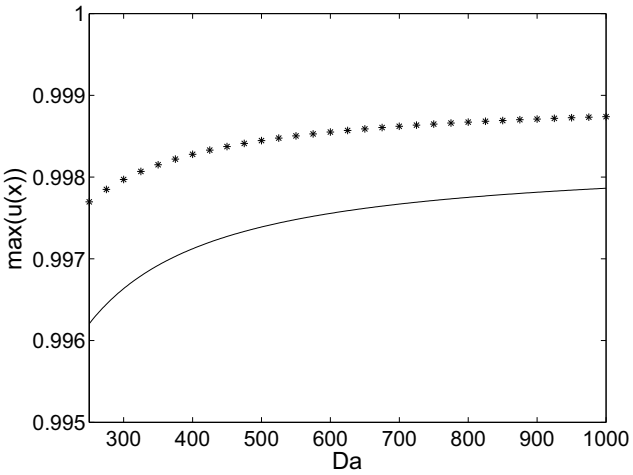

(a)

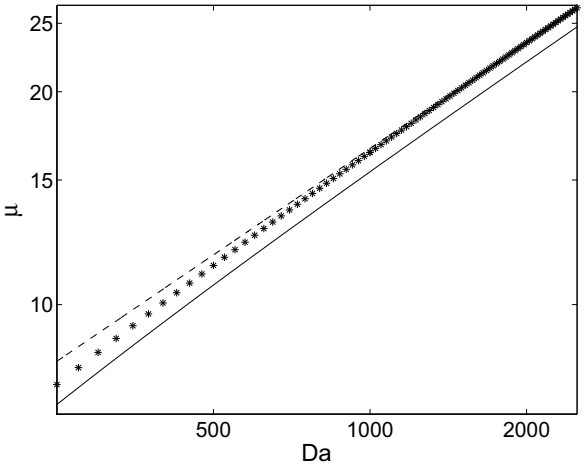

(b)

Figure 5.20: Comparison of the results obtained from the numerical solution of (5.1)-(5.2) (represented by stars) with the corresponding results obtained using the nonperturbative method with the tanh-based test function (5.16) (represented by a continuous line) at $\varepsilon = 0.02$ and $a = 0$ over a range of Da. (a) Maximal amplitude of the profile of the solution. (b) Logarithmic plot of the distance of the pulses from $x = 0$. A reference line with slope $1/2$ (represented by a dashed line) is also shown.

5.5.2 Solutions near the large Damköhler number saddle-node

As discussed in Sec. 5.3.1, at large Damköhler numbers there exists a critical value $\varepsilon_c(Da)$ above which propagation failure sets in. This corresponds to a saddle-node bifurcation, and in this region the profile of the stable stationary solution of the activator $u(x)$ can be characterised by two separated bell shaped pulses as shown in Fig. 5.7. We perform the nonperturbative approach in this region using two different test functions.

We shall first use a tanh-based test function (5.16) which, as seen in Fig. 5.19, can approximate the solution profiles observed in this region. This test function has free parameters $\{p_i\} = \{g_0, \omega, \nu, \mu\}$ and its tangent space is spanned by (5.17). Performing the nonperturbative approach with this test function we obtain four conditions (5.11), which are solved numerically to obtain values for the free parameters over a range of ε.

Next, we recall from the asymptotic analysis in Section 5.3.1 that in the limit $Da \to \infty$, the system (5.1)-(5.2) is equivalent to the unstirred system (5.7)-(5.8). This allows us to directly use the results of [47] for excitable unstirred media as a comparison. As we consider the limiting case where the activator diffuses slowly, we set $D_2 = 0$ in (5.8). The pulse was described using a bell shaped test function $\tilde{U} = \exp(-\eta^2)$. Using the nonperturbative method the amplitude f_0 could be formulated as [47]

$$A\, f_0^2 + B\, f_0 + C = 0\,, \tag{5.18}$$

where

$$\begin{aligned} A &= \frac{3}{4}\langle \tilde{U}^4 \rangle - \frac{5}{6}\langle \tilde{U}^3\, V \rangle - \frac{a\,\Theta}{3}\langle \eta\, \tilde{U}^3\, V \rangle\,, \\ B &= -\frac{5}{6}(1+u_s)\langle \tilde{U}^3 \rangle + \langle \tilde{U}^2\, V \rangle + \frac{a\,\Theta}{2}\langle \eta\, \tilde{U}^2\, V \rangle\,, \quad C = u_s \langle \tilde{U}^2 \rangle\,. \end{aligned} \tag{5.19}$$

and where $\Theta = \varepsilon Da/\mu\, w$. The inhibitor is defined as $v(\eta) = f_0\, V(\eta)$, given explicitly by the solution of (5.8). We therefore solve

$$V_\eta = -\frac{\varepsilon Da}{\mu\, w}(U - a\, V)\,. \tag{5.20}$$

The expression for the inverse width found by this method is given by

$$\begin{aligned} w^2 = \frac{1}{D\langle \tilde{U}_\eta^2 \rangle}\Big[& f_0^2(-\langle \tilde{U}^4 \rangle + \langle \tilde{U}^3\, V \rangle) + \\ & f_0((1+u_s)\langle \tilde{U}^3 \rangle - \langle \tilde{U}^2\, V \rangle) - u_s \langle \tilde{U}^2 \rangle \Big]\,. \end{aligned} \tag{5.21}$$

The velocity $\bar{w}$ can be found by integrating the product of (5.7) and u_x over x, giving the expression

$$\bar{w} = -\frac{f_0\Theta}{w\langle\tilde{U}_\eta^2\rangle}\left[\frac{f_0}{3}(\langle\tilde{U}^4\rangle - a\langle\tilde{U}^3\,V\rangle) - \frac{1}{2}(\langle\tilde{U}^3\rangle - a\langle\tilde{U}^2\,V\rangle)\right]. \tag{5.22}$$

From the phenomenological argument described in Sec. 2.2, the width of the stationary solution in the rescaled system can be understood as the balance of this velocity with the stirring, and so $\mu \approx \bar{w}\sqrt{Da}$.

In Fig. 5.21 we show a comparison of the two different test functions comparing with results obtained from the numerical solution of the full system (5.1)-(5.2). We find that the results for the amplitudes as well as the distance of the pulses from $x = 0$ obtained from these two sets of results yield equally good agreement with the results obtained from the full system. We observe that the form of the approximate solution agrees well with that of the numerical solution since the generic quadratic behaviour of a saddle-node is recovered (compare (5.18)). However, since this is only an approximation, the actual amplitudes of the test functions do not closely agree with the corresponding numerical results.

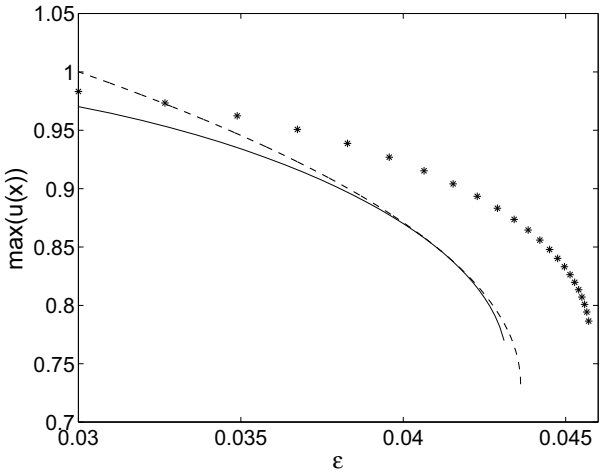

(a)

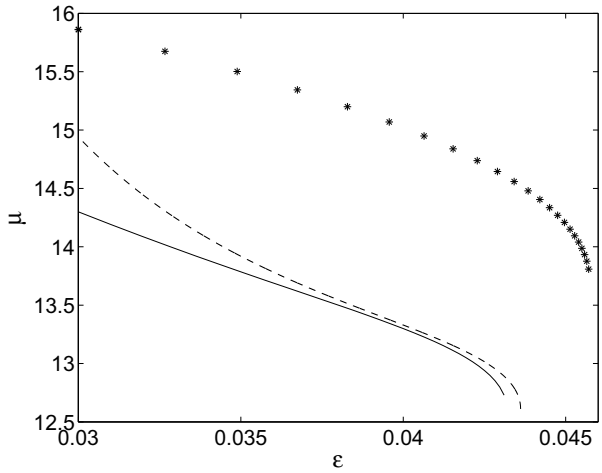

(b)

Figure 5.21: Comparison of the results obtained from the numerical solution of (5.1)-(5.2) at $Da = 1000$ and $a = 0$ (represented by stars) with the corresponding results obtained using the nonperturbative method. The results obtained with the analytical formulae (5.18) and (5.22) for a Gaussian test function (5.14) are represented by a dashed line. The results obtained from the solution of (5.11) for the tanh-based test function (5.16) are represented by a continuous line. (a) Maximal amplitude of the solution profiles. (b) Distance of the pulses from $x = 0$.

5.5.3 Solutions near the low Damköhler number saddle-node

We now examine the saddle-node associated with excessive stirring of the system. As discussed in Sec. 5.3.2, for values of the Damköhler number less than a critical value Da_c the pulses become too quenched and cannot sustain excitation anymore. This corresponds to a saddle-node bifurcation, which we shall describe explicitly using our nonperturbative variational method. Guided by our asymptotic analysis in Section 2.3 and numerical observation (see Fig. 5.8), we use a Gaussian test function $U(\eta)$ (5.14). The inhibitor $v(x)$ can then be given explicitly via (5.5) as

$$V(\eta) = \frac{f_0\,\alpha}{a}\,\eta^{2\alpha}\Gamma(-\alpha,\eta^2)\,, \tag{5.23}$$

which is in terms of the incomplete Gamma function

$$\Gamma\left(\alpha,x\right) = \int_x^\infty \varsigma^{\alpha-1}e^{-\varsigma}d\varsigma\,, \tag{5.24}$$

and where we introduce $\alpha = Da\,\varepsilon\,a/2$.

Projecting onto the tangent space of the restricted subspace, we obtain the conditions

$$\langle w^2\,U_{\eta\eta} + \eta\,U_\eta + Da\,U(1-U)(U-u_s-V)\;\mid\;U\rangle_\eta = 0\,, \tag{5.25}$$
$$\langle w^2\,U_{\eta\eta} + \eta\,U_\eta + Da\,U(1-U)(U-u_s-V)\;\mid\;\eta U_\eta\rangle_\eta = 0\,, \tag{5.26}$$

where $V(\eta)$ is given by (5.23).

This system is solved analytically to obtain expressions for the free parameters f_0 and w (see Appendix B). The expression for the amplitude f_0 has a quadratic form, and is given by

$$f_0 = \frac{-B \pm \sqrt{B^2 - 4\,A\,C}}{2A}\,, \tag{5.27}$$

where

$$\begin{aligned} A =& \frac{9\,a+8\,\alpha}{24\,a}\sqrt{\pi} - \frac{5+4\,\alpha}{6}K(3)\,,\\ B =& -\frac{5\,a\,(1+u_s)+6\,\alpha}{6\,a}\sqrt{\frac{\pi}{3}} + (\alpha+1)\,K(2)\,,\\ C =& \sqrt{\frac{\pi}{2}}\left(u_s+\frac{1}{Da}\right)\,, \end{aligned} \tag{5.28}$$

and the inverse width is given by the algebraic expression

$$w = \sqrt{Da}\left[f_0^2 \left(\sqrt{\frac{2}{\pi}} K(3) - \frac{1}{\sqrt{2}} \right) - f_0 \left(\sqrt{\frac{2}{\pi}} K(2) - (1-u_s)\sqrt{\frac{2}{3}} \right) - \left(u_s + \frac{1}{2\,Da} \right) \right]^{1/2} . \tag{5.29}$$

Here we have defined a function $K(n)$ as

$$K(n) = \frac{\alpha}{a}\Gamma(-\alpha)\,\Gamma\left(\alpha+\frac{1}{2}\right) n^{-\frac{1}{2}-\alpha} + \frac{1}{a}\sqrt{\frac{\pi}{n}}\,{}_2F_1\left(\left\{ \frac{1}{2}, -\alpha \right\}; \{1-\alpha\}; -\frac{1}{n} \right) . \tag{5.30}$$

which in the limit $a \to 0$ becomes

$$K(n) = Da\,\varepsilon \sqrt{\frac{\pi}{n}}\,\mathrm{arcsinh}\big(\sqrt{n}\big) . \tag{5.31}$$

The quadratic equation (5.27) for the amplitude f_0 yields the stable and unstable solutions. For $B^2 - 4\,A\,C = 0$ these solutions coalesce and then subsequently vanish in a saddle-node bifurcation. The condition $B^2 - 4\,A\,C = 0$ determines the bifurcation point Da_c. Once the amplitude f_0 is determined we may calculate the inverse width w using (5.29).

The expressions for the amplitude f_0 simplify in certain limits. In Appendix B, we describe in detail how the bistable case of [91, 26] is recovered in the limit $\varepsilon \to 0$ when the inhibitor is constant and the system (5.1)-(5.2) is no longer excitable, but bistable. In the limit of $Da \to \infty$ we find that in accordance with the asymptotic calculation of Section 2.3 we recover the results for the unstirred Barkley model found in [47] and used in Section 5.5.2.

In addition to these expressions for a Gaussian test function, we shall also numerically obtain results for the parameters $\{p_i\} = \{g_0, \omega, \nu, \mu\}$ of the tanh-based test function (5.16). As seen in Fig. 5.18, this test function can also be used to describe a bell shaped profile. We will perform the nonperturbative method with such a test function to obtain conditions (5.11) for $\{p_i\}$ which are solved numerically over a range of Da.

In the following we show how well the nonperturbative variational method captures the actual dynamics of the full system (5.1)-(5.2). In Fig. 5.22, we compare the analytical results for the amplitude of a Gaussian as well as the tanh-based test function with those of a numerical simulation of (5.3)-(5.4). For larger values of ε, the comparison is clearly better for the tanh-based test

function than for the Gaussian test function. Although the solution close to the saddle-node bifurcation is well approximated by a Gaussian test function, as evidenced by Fig. 5.9a and 5.9b, for larger values of ε the solution develops rapidly into two separate interacting pulses with increasing Damköhler number, as seen in Fig. 5.9b. This explains the better performance of the more versatile tanh-based test function (5.16) when compared to the simpler Gaussian test function (5.14). Fig. 5.22 also reveals that the unstable solution is well approximated by a Gaussian, typical for these systems [26].

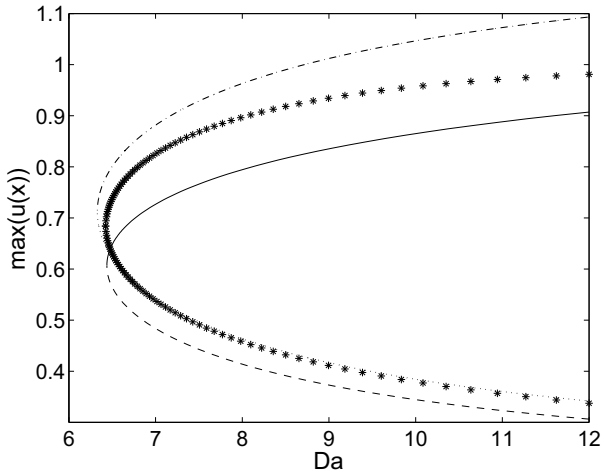

(a)

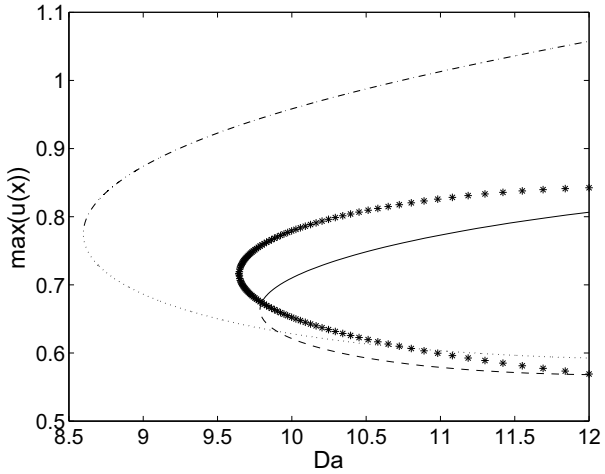

(b)

Figure 5.22: Comparison of the amplitudes of the stable and unstable stationary solutions over a range of Da at $a = 0$. The results obtained from the numerical solution of (5.3)-(5.4) are represented by stars. The results obtained with the analytical formula (5.27) for a Gaussian test function (5.14) are represented by dashed-dotted and dotted lines for the stable and unstable branches respectively. The results obtained using the nonperturbative method with the tanh-based test function (5.16) are represented by continuous and dashed lines for the stable and unstable branches respectively. (a) $\varepsilon = 0.005$. (b) $\varepsilon = 0.03$.

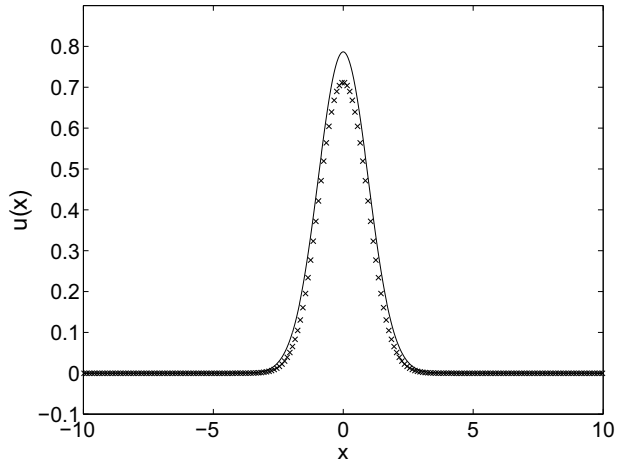

Figure 5.23: The profile of the stationary solution of the activator $u(x)$ obtained from the numerical simulation of the system (5.3)-(5.4) (represented by crosses) at $Da = 6.45$, $a = 0$ and $\varepsilon = 0.005$ superimposed with a Gaussian test function (represented by continuous line) whose parameters f_0 and w are calculated using (5.27) and (5.29) at the corresponding values of the system variables.

In Fig. 5.23 we show a comparison between the activator $u(x)$ calculated from the numerical solution of the full system (5.3)-(5.4) and a Gaussian test function whose parameters f_0 (5.27) and w (5.29) are calculated using the nonperturbative method. We see in Fig. 5.24 that the critical Damköhler number $Da_c(\epsilon)$ for a Gaussian test function, as calculated from the criterion $B^2 - 4\,A\,C = 0$, closely approximates the corresponding numerical solution of the system at low ϵ but is a poor fit at large ϵ. Again this is due to the stronger deviation of the solution from a Gaussian shape for larger values of ε. The results obtained for the nonperturbative method with the tanh-based test function (5.16) show excellent agreement with the numerical results of the full system for all ϵ.

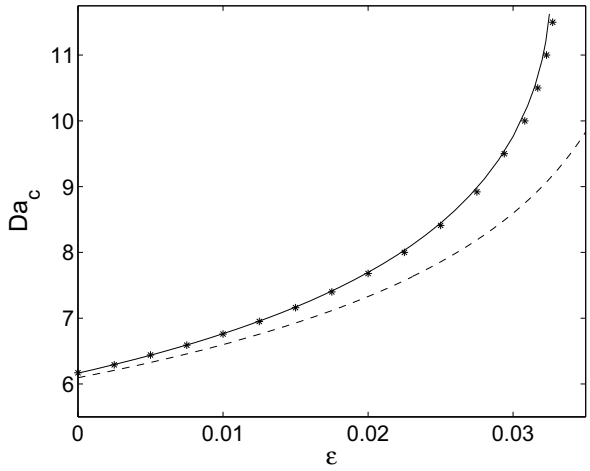

Figure 5.24: Comparison of the critical values of the Damköhler number $Da_c(\varepsilon)$ for $a = 0$ obtained from the numerical solution of the system (5.3)-(5.4) (represented by stars) with the corresponding values calculated using the nonperturbative method with a Gaussian test function (5.14) from the condition $B^2 - 4\,A\,C = 0$ (represented by dashed line) and the tanh-based test function (5.16) (represented by a continuous line).

5.5.4 Solution behaviour in the hysteresis loop

We now examine the region of bistability observed for small values of ϵ and sufficiently large values of Da. As described in Sec. 5.3.3, this bistability is linked to the different asymptotic solutions at the respective limits of $\epsilon \to 0$ and $Da \to \infty$. In the limit $\epsilon \to 0$ the system (5.1)-(5.2) is not excitable anymore but bistable and the solution consists of a single plateau-like solution. In the limit $Da \to \infty$ the stirred system behaves like an unstirred excitable medium and has two well separated pulses symmetrically arranged around the origin at $x = 0$. In the simultaneous limit $\epsilon \to 0$ and $Da \to \infty$ we find the coexistence of both solution types (see Fig. 5.25). As this region is more pronounced for larger values of a approaching the bistable limit $a = 1/(1 - u_s)$ (see Fig. 5.11), we shall take $a = 1$ in the following.

This region is characterised by a hysteresis loop, illustrated in Fig. 5.26, and the observed solution behaviour of the system (5.1)-(5.2) depends on the initial condition. In Fig. 5.26 we show the hysteresis loop and provide a comparison of our nonperturbative test function approach using the tanh-based test function (5.16) with results from the simulation of the full system (5.1)-(5.2). The test function approach clearly captures both solution types ex-

hibiting bistability. The nonperturbative method approximates the solution well and is able to detect the bifurcation at Da_{hys_1}. The upper bifurcation point Da_{hys_2} is largely overestimated by the test function approach as can be clearly seen from Fig. 5.27. This can be linked to the near-degeneracy of the stable and unstable branches at large Damköhler numbers. In the test function approach the unstable solution of the "double-plateau" solution coincides for large Da with the stable branch of the single plateau solution. The kink of the unstable branch of the single plateau solution as seen in Fig. 5.27 stems from the functional change of the unstable solution at this point from a single pulse solution to that of two separated pulses.

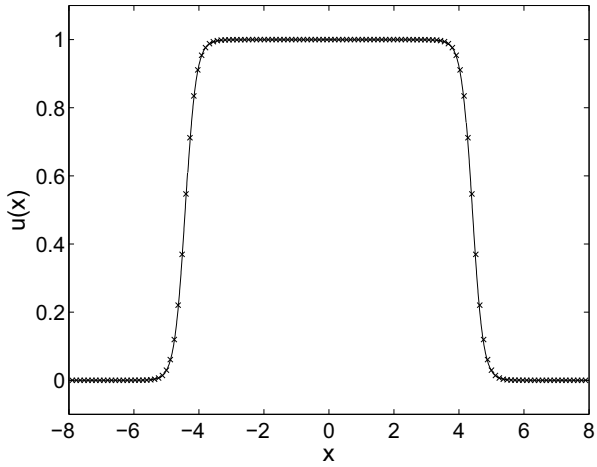

(a)

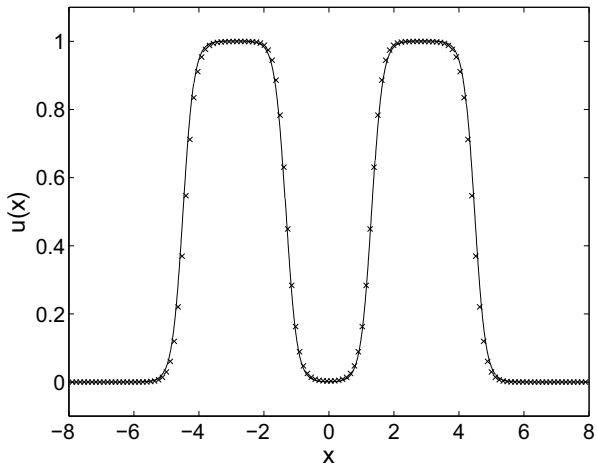

(b)

Figure 5.25: The profiles of the stable stationary solutions of the activator $u(x)$ in the bistable region at $Da = 70$, $a = 1$ and $\varepsilon = 0.01$. The solutions obtained by numerically integrating the full system (5.1)-(5.2) are represented by crosses and the profiles of the tanh-based test function (5.16) whose parameters are obtained using the nonperturbative method at the corresponding system variables represented by a continuous line. (a) The plateau like solution at these values of the system parameters. (b) The "double-plateau" like solution at these values of the system parameters.

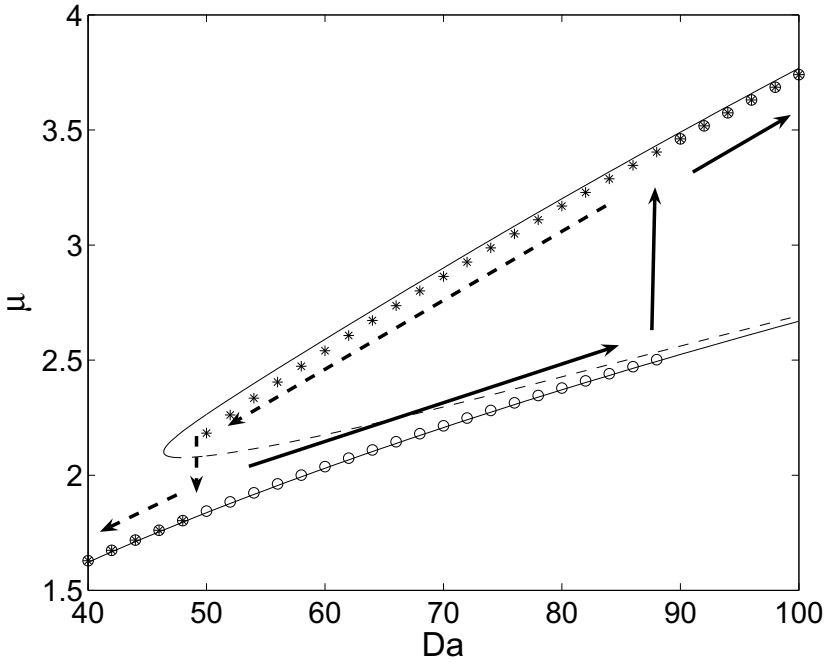

Figure 5.26: Comparison of the distance of the pulses from the centre, μ, obtained from the numerical simulation of (5.1)-(5.2) with the corresponding values obtained from the nonperturbative approach over a range of Da for $\varepsilon = 0.01$ and $a = 1$. The results obtained using the nonperturbative method are represented by continuous lines for the two stable branches, while the unstable branch is represented by a dashed line. The arrows indicate the hysteresis loop. The numerical results obtained when starting with the plateau like profile at $Da = 40$ and slowly increasing Da are represented by circles. The numerical results obtained when starting with the "double-plateau" like solution at $Da = 100$ and slowly decreasing Da are represented by stars. Note the near-degenerate behaviour of the stable and unstable branches.

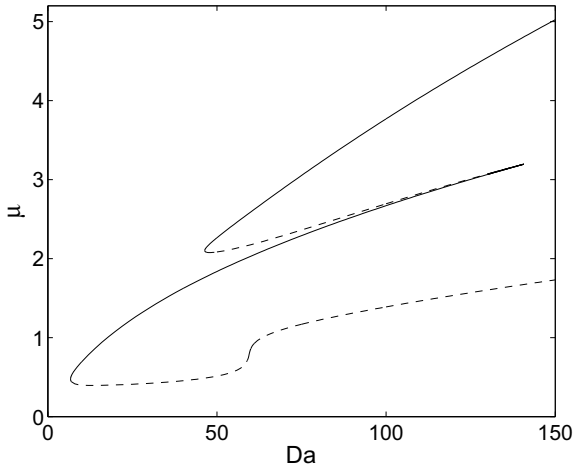

Figure 5.27: Distance of the pulses from the centre, μ, over a range of Da for $\varepsilon = 0.01$ and $a = 1$ obtained using nonperturbative method by evaluating (5.11) for the tanh-based test function (5.16). The stable branches are represented by continuous lines while the unstable branches are represented by dashed lines.

5.5.5 Solution behaviour near the Hopf bifurcation

The stable oscillatory solutions near the Hopf bifurcation can be described using a time-dependent version of the nonperturbative method. The solution profile of the activator in this oscillatory region is that of two slightly separated bell shaped pulses whose separation width and maximal amplitude vary in time (as described in Sec. 5.3.4). Profiles of this type can be approximated using the tanh-based test function (5.16), (as seen in Fig. 5.19). We now consider time-dependent parameters for the test function, $\{p_{u_i}(t)\} = \{g_0(t), \omega(t), \mu(t), \nu(t)\}$, to describe the behaviour of $u(x,t)$. In the time-dependent case, the behaviour of the inhibitor cannot be described through the explicit solution of the equation (5.4) and we shall therefore consider a time-varying test function V. From numerical simulations in this regime, we observe that a test function of the type

$$V(x,t) = h_0(t)\exp(-|\zeta|) \;\text{ with }\; \zeta = \kappa(t)\,x\,, \tag{5.32}$$

is a good approximation to the behaviour of $v(x,t)$. This test function has free (time-dependent) parameters $\{p_{v_i}(t)\} = \{h_0(t), \kappa(t)\}$, and is spanned by the set of basis functions

$$\frac{\partial V}{\partial h_0} = \frac{V}{h_0}\,, \quad \frac{\partial V}{\partial \kappa} = \frac{\zeta\, V_\zeta}{\kappa}\,. \tag{5.33}$$

In our calculations we shall only consider positive nonzero values of x, and perform our calculations for values of $x \geq 10^{-20}$. This introduces a small (negligible) error in not taking the $x = 0$ region of the integrals. However, this approach avoids difficulties arising with the derivative of (5.32) which is not defined at $x = 0$.

As described in Section 5.4, the projection of the equations (5.1)-(5.2) onto the tangent space of these test functions yields a system of $4 + 2$ first order ordinary differential equations for the set of parameters $\{p_i(t)\} = \{p_{u_i}(t), p_{v_i}(t)\} = \{g_0(t), \omega(t), \mu(t), \nu(t), h_0(t), \kappa(t)\}$, (5.11) and (5.12), which we write here as

$$\sum_{j=1}^{4} \left\langle \dot{p}_j \frac{\partial U}{\partial p_j} \,\middle|\, \frac{\partial U}{\partial p_i} \right\rangle_\eta = \left\langle \omega^2 U_{\eta\eta} + \eta U_\eta + Da\, U(1-U)(U - u_s - V) \,\middle|\, \frac{\partial U}{\partial p_i} \right\rangle_\eta , \tag{5.34}$$

$$\sum_{j=1}^{2} \left\langle \dot{q}_j \frac{\partial V}{\partial q_j} \,\middle|\, \frac{\partial V}{\partial q_i} \right\rangle_\zeta = \left\langle \delta\kappa^2 V_{\zeta\zeta} + \zeta V_\zeta + Da\, \varepsilon\, (U - a\, V) \,\middle|\, \frac{\partial V}{\partial q_i} \right\rangle_\zeta . \tag{5.35}$$

The critical Damköhler numbers of the Hopf bifurcation Da_{H_1} (and Da_{H_2}) for the system (5.34)-(5.35) are found by locating the values of Da above which (and below which) the parameters $\{p_i(t)\}$ are oscillatory. The values obtained with this nonperturbative method are found to be close to the corresponding values obtained by numerically solving the full system (5.1)-(5.2) (see Fig. 5.28). The observed time period T of the oscillations at the critical values in both cases show good agreement (see Fig. 5.29).

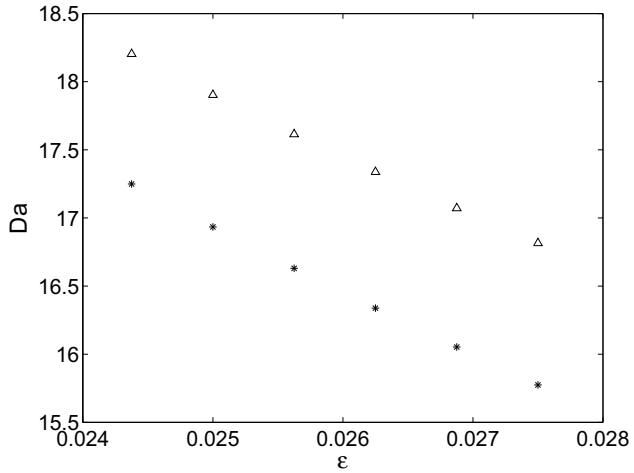

(a)

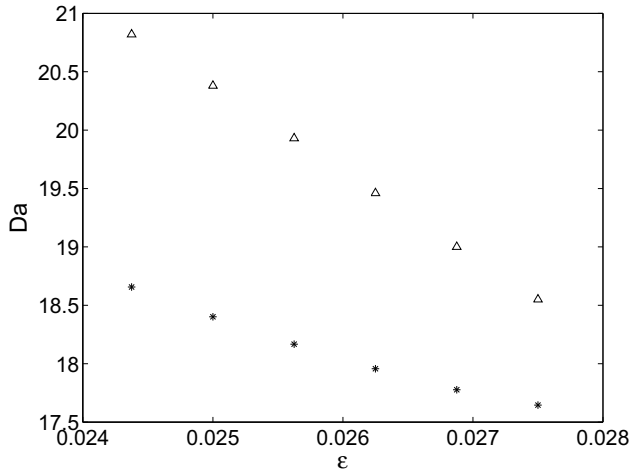

(b)

Figure 5.28: Comparison of the values of the critical Damköhler number of the Hopf bifurcation $\varepsilon_c(Da)$ obtained from the numerical solution of the system (5.1)-(5.2) (represented by stars) with the corresponding results obtained using the nonperturbative method with test functions (5.16) and (5.32) for the activator and inhibitor (represented by triangles) over a range of ε for $a = 0$. (a) Comparison of results along the lower branch Da_{H_1}. (b) Comparison of results along the upper branch Da_{H_2}.

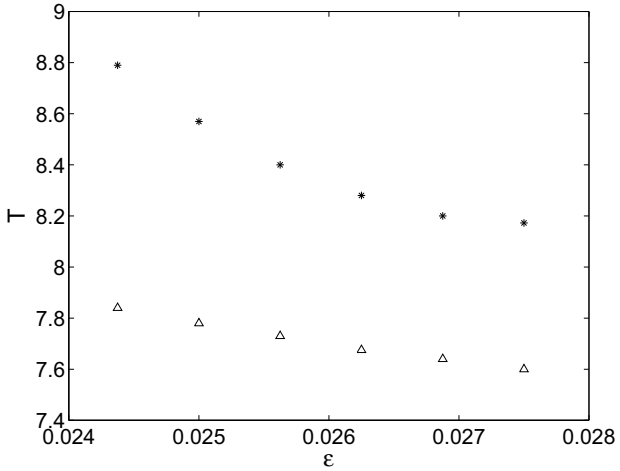

(a)

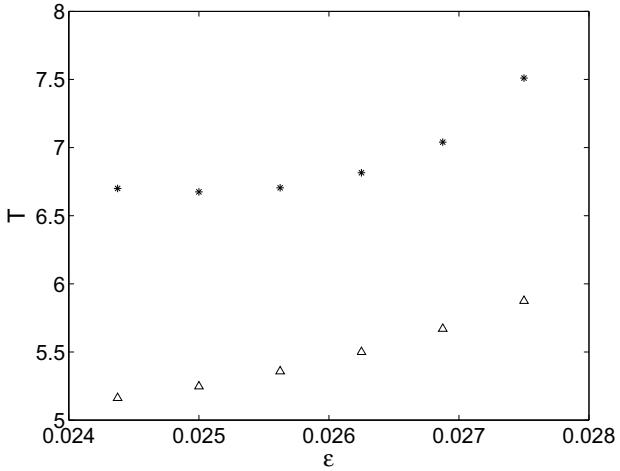

(b)

Figure 5.29: Comparison of the values of the time period T of the oscillations at the critical Damköhler number of the Hopf bifurcation $\varepsilon_c(Da)$ obtained from the numerical solution of the system (5.1)-(5.2) (represented by stars) with the corresponding results obtained using the nonperturbative method with test functions (5.16) and (5.32) for the activator and inhibitor (represented by triangles) over a range of ε for $a = 0$. (a) Comparison of results along the lower branch Da_{H_1}. (b) Comparison of results along the upper branch Da_{H_2}.

5.6 Summary

In this chapter, we studied the effect of chaotic stirring on an excitable system using a 1-D filamental model discussed in Chapter 2. In particular, we examined a system where the diffusion coefficient of the activator is much larger than that of the inhibitor. We found that the bifurcation scenarios are organised around two saddle-node bifurcations separating the Da-ε parameter space into a part with no solutions and a part with various steady and unsteady pulse solutions. We identified one of the saddle-nodes as the generic saddle-node for excitable media, and another saddle-node as the generic saddle-node for chaotically stirred reaction-diffusion systems. We also found a region of bistable behaviour and an associated hysteresis loop. Within this bistable region we find the two solution types characteristic for the limit $Da \to \infty$ and $\varepsilon \to 0$. Connecting to the bistable region in a homoclinic bifurcation we find two Hopf branches. Unlike in unstirred excitable media the Hopf bifurcation is supercritical. However, close to the high codimension bifurcation points where the supercritical Hopf branches collide with the saddle-node bifurcations, we found a subcritical Hopf bifurcation as well as complex unfoldings including bistability between stable stationary and stable oscillatory solutions.

We applied a nonperturbative method discussed in Chapter 3 to describe the bifurcation behaviour. This nonperturbative approach allowed us to reduce the steady-state equations (5.3)-(5.4) to a set of algebraic equations for the parameters of the test function to describe the steady solution, and the partial differential equations (5.1)-(5.2) to a set of ordinary differential equations to describe oscillatory solutions. We showed that the nonperturbative approach captures well the bifurcation scenarios and the solution behaviour, and hence allows for an effective reduced description of the full system.

Chapter 6

Two component systems: Flame filaments in a combustion system

6.1 Introduction

Combustion reactions are found to be affected by fluid mixing processes [128, 125, 136, 22, 23, 1, 62, 64, 63]. In particular, excessive stirring may induce an unwanted termination of the combustion reaction. This arises through the removal of heat from the resulting flame filaments due to stirring. Beyond a critical stirring rate, a travelling combustion front will therefore not contain enough heat to ignite the fuel and the flame will be quenched.

A combustion system under the influence of chaotic mixing gives rise to elongated flame filamental structures, and such a system can be analysed using the 1-D cross-filament model discussed in Chapter 2. It was observed in [64, 63], that the quenching of the flame depends on the Damköhler number Da of the stirred system. If the Damköhler number is below a critical value Da_c, the reaction cannot spread and a flame will be extinguished. This propagation failure corresponds to a saddle-node bifurcation of the underlying reaction-advection-diffusion equations.

In this chapter, we study the influence of chaotic stirring on combustion waves. A combustion wave can be (at least for low stirring rates) divided into three distinct regions [165]. Ahead of the combustion waves, in the so called preheat zone, the temperature is low and the reactant has not been burnt. When the temperature increases and becomes sufficiently high, the reaction rate increases exponentially and the reactant is quickly burnt under heat release. This takes place in a narrow steep region called the reaction zone. Behind the front there is the product zone where all reactant is burnt,

no reaction occurs and the temperature is constant. One particularity for problems involving combustion waves is the strong dependence of the reaction rate on the temperature. As we shall discuss in Sec. 6.2, this is usually modelled by an Arrhenius term [167].

Besides the Damköhler number, the behaviour of these combustion waves is characterised by a dimensionless variable known as the Lewis number Le. The Lewis number is defined as

$$Le = \frac{\kappa}{\rho\, C_p\, D}\,, \tag{6.1}$$

and depends on the diffusion coefficient D, the density of the fuel ρ, the specific heat capacity C_p and the thermal conductivity κ [167], and can be understood as a relative measure of the diffusivities of the temperature and reactant. Systems with a large Lewis number are often called "solid" whereas systems with low Lewis numbers are called "gaseous" [165].

The system behaviour depends strongly on the value of the Lewis number. In particular, combustion waves propagate faster in systems with large values of Le. A system with a relatively small diffusion coefficient (and hence a larger value of Le) has less fuel transport between burnt and unburnt regions of the system and therefore allows faster wave propagation. The combustion speed also increases in systems with larger thermal conductivities, lower fuel densities (where less heat is needed for fuel ignition) or smaller specific heat capacities (where relatively less heat is needed to raise the temperature of the fuel).

For very small values of Le, the steepness of the profile of the solution in the reaction zone varies rapidly as we move from the inner to outer regions. This behaviour arises due to an increase in the preheat zone. The steady-state solutions of the system have been analysed asymptotically in the limits of small and large Lewis numbers, as well as the limit $Da \to \infty$ [64]. In addition, the behaviour of the critical Damköhler number was investigated numerically using a 1-D filament model. However, the solution behaviour near the saddle-node has not been previously studied.

In this chapter, we shall examine the behaviour of a combustion system under the influence of chaotic stirring, and demonstrate the applicability of the nonperturbative method to such a model. We shall analyse the behaviour of this system near the bifurcation point, and far away from it for a range of values of the Lewis number. In addition, we shall present an empirical formula for the speed of a travelling wave in the unstirred system. Part of this work has been published in [92].

6.2 Description of the model

We shall consider a simple combustion system in which a fuel A, of concentration c and absolute temperature T, is converted into an inert product P. This can be modelled as a first order process through the reaction $A \to P$. When such a system is subjected to a chaotic stirring flow, it exhibits filamental structures (as described in Sec. 2.1). We analyse these flame filaments again using a 1-D model proposed in [64, 63], which describes the cross-filament behaviour of the temperature and concentration of the fuel. The temperature dependence of the reaction rate is given by

$$k(T) = \begin{cases} k_0 \exp\left(-\dfrac{E}{R\,T}\right) & \text{if} \quad T > T_i\,, \\ 0 & \text{if} \quad T \le T_i\,, \end{cases} \tag{6.2}$$

where T_i is the ignition temperature of the reaction, E is the activation energy, R is the universal gas constant and k_0 is a constant factor. A nonzero cutoff temperature T_i allows for a simple solution to a typical problem encountered in such systems, the "cold boundary problem" [167]. Large preheat zones may arise, especially for small Lewis numbers, which imply a nonzero temperature at the boundary, far from the reaction zone. Hence a nonzero cutoff allows for a finite box with a cold boundary $T = 0$. Although a purely Arrhenius term should lead to qualitatively similar results, we shall use the reaction term (6.2) to simplify our numerical simulations.

The model is then given by

$$\rho\, C_p \left(\frac{\partial T}{\partial t} - \lambda\, x\, \frac{\partial T}{\partial x}\right) = \kappa \frac{\partial^2 T}{\partial x^2} + q\, c\, k(T)\,, \tag{6.3}$$

$$\frac{\partial c}{\partial t} - \lambda\, x\, \frac{\partial c}{\partial x} = D\, \frac{\partial^2 c}{\partial x^2} - c\, k(T)\,, \tag{6.4}$$

in the region $-\infty < x < \infty$, where the reaction rate $k(T)$ is given by (6.2) and q is the exothermicity of the reaction. The constant λ, which measures the chaotic stirring, is again given by the Lagrangian mean strain or the topological entropy associated with the ambient chaotic flow (as described in Chapter 2). We apply the boundary conditions

$$T \to T_a\,, \quad c \to c_0\,, \tag{6.5}$$

as $|x| \to \infty$, where c_0 is the concentration of the unburnt fuel, and the temperature at the boundary is given by the ambient temperature T_a. We nondimensionalise the model by introducing the variables $T' = (T - T_a)/(T_b - T_a)$, $c' = c/c_0$, $t' = \lambda\, t$ and $x' = x\sqrt{\lambda/D}$. Here, c_0 is the maximum concentration

and T_b is the burnt temperature given by $T_b = T_a + (q\,c_0/\rho\,C_p)$. Substituting these variables into (6.3)-(6.4) and omitting the primes, we get

$$\frac{\partial T}{\partial t} - x\,\frac{\partial T}{\partial x} = Le\frac{\partial^2 T}{\partial x^2} + Da\,c\,K(T)\,, \tag{6.6}$$

$$\frac{\partial c}{\partial t} - x\,\frac{\partial c}{\partial x} = \frac{\partial^2 c}{\partial x^2} - Da\,c\,K(T)\,, \tag{6.7}$$

where we have introduced the Lewis number (6.1). As in Chapter 2, the ratio of the time scales of reaction and stirring is given by the Damköhler number $Da = k_0/\lambda$. The boundary conditions of this system are

$$T \to 0\,, \quad c \to 1\,, \tag{6.8}$$

as $|x| \to \infty$, and its reaction rate is given by

$$K(T) = \begin{cases} \exp\left(-\dfrac{1}{\epsilon\,((1-\beta)T+\beta)}\right) & \text{if} \quad T > \bar{T}_i\,, \\ 0 & \text{if} \quad T \le \bar{T}_i\,, \end{cases} \tag{6.9}$$

where we now have the parameters

$$\epsilon = \frac{RT_b}{E}\,, \qquad \beta = \frac{T_a}{T_b}\,, \qquad \bar{T}_i = \frac{T_i - T_a}{T_b - T_a}\,. \tag{6.10}$$

We shall use the values $\beta = 0.1$, $\epsilon = 1$ and $\bar{T}_i = 0.001$ for our numerical simulations.

A chaotically stirred system of this type exhibits stationary solutions which, as discussed in Sec. 2.2, arise from the balance between stirring and diffusion. The steady state solutions of the system are given by

$$Le\,\frac{d^2T}{dx^2} + x\,\frac{dT}{dx} + Da\,c\,K(T) = 0\,, \tag{6.11}$$

$$\frac{d^2c}{dx^2} + x\,\frac{dc}{dx} - Da\,c\,K(T) = 0\,. \tag{6.12}$$

This system exhibits the generic saddle-node bifurcation of lamellar models at a certain critical Damköhler number Da_c. For all values of $Da > Da_c$, a stable nontrivial stationary solution coexists with an unstable one. These solution branches collide at the saddle-node, and for all $Da < Da_c$ we find that nontrivial solutions do not exist.

We shall use the nonperturbative method described in Chapter 3 to study the behaviour of the steady-state solutions of this system over a range of Da and Le. We will describe the solution at the saddle-node and far away from it.

6.3 Analysis using the nonperturbative variational method

The profiles of the steady-state solutions of $T(x)$ (and $1-c(x)$), obtained from (6.11)-(6.12) via shooting methods, are found to be either bell-shaped or plateau-like depending on the value of Da and Le (see Fig. 6.2, 6.6 and 6.8). In particular, close to the saddle-node the profiles are bell-shaped for all values of Le, while the solution far away from the saddle-node is plateau-like. For larger values of Le, the transition in profile from a bell-shaped solution to a plateau like solution occurs quicker upon increasing Da.

To examine some of these trends, we shall use appropriately shaped test functions for the nonperturbative method. We shall consider the general form

$$T(x) = \Theta(x, p_{T_i}) \qquad \text{and} \qquad c(x) = 1 - \Omega(x, p_{c_i})\,, \tag{6.13}$$

where $\Theta(x, p_{T_i})$ and $\Omega(x, p_{c_i})$ are chosen according to the behaviour of the solution at the corresponding values of Da and Le.

Near the critical Damköhler number Da_c the solutions are bell-shaped. This numerical observation is consistent with our asymptotic analysis for small Da in Chapter 2. This motivates the use of Gaussian test functions (3.6),

$$\begin{aligned} \Theta(x, p_{T_i}) =& f_0 \, \exp\left(-\eta^2\right), \\ \Omega(x, p_{c_i}) =& g_0 \, \exp\left(-\zeta^2\right), \end{aligned} \tag{6.14}$$

with $\eta = w\,x$ and $\zeta = v\,x$. The complete set of parameters are given by $\{p_i\} = \{p_{T_i}, p_{c_i}\} = \{f_0, w, g_0, v\}$. Here, the parameters f_0 and g_0 are the amplitudes of the test functions, while w and v are the corresponding inverse pulse widths. One may equally use other bell-shaped test functions such as sech^2-functions and, as we shall see in Sec. 6.4.1, the exact choice of bell-shaped function does not significantly alter the results. Hence, we may alternatively describe the solution in this region using

$$\begin{aligned} \Theta(x, p_{T_i}) &= f_0 \, \text{sech}^2\eta\,, \\ \Omega(x, p_{c_i}) &= g_0 \, \text{sech}^2\zeta\,, \end{aligned} \tag{6.15}$$

with $\eta = w\,x$ and $\zeta = v\,x$. The complete set of parameters are again given by $\{p_i\} = \{p_{T_i}, p_{c_i}\} = \{f_0, w, g_0, v\}$.

For larger values of Da the stable solutions are plateau-like, and can be described using front-like test functions (3.8),

$$\begin{aligned} \Theta(x, p_{T_i}) =& \frac{f_0}{2}\left(\tanh\left(\eta + \mu\, w\right) - \tanh\left(\eta - \mu\, w\right)\right), \\ \Omega(x, p_{c_i}) =& \frac{g_0}{2}\left(\tanh\left(\zeta + \phi\, v\right) - \tanh\left(\zeta - \phi\, v\right)\right), \end{aligned} \tag{6.16}$$

with $\eta = w\,x$ and $\zeta = v\,x$. The complete set of parameters is given by $\{p_i\} = \{p_{T_i}, p_{c_i}\} = \{f_0, w, \mu, g_0, v, \phi\}$. The parameters μ and ϕ represent the widths of the corresponding test functions measured from $x = 0$ to the turning points. Here, the parameters w and v give a measure of the steepness of the solution in the reaction zone.

By choosing (6.16) we ignore the problem of a preheat zone which would requires us to take two composite tanh-based functions as test functions, each equipped with two different widths $\mu_{1,2}$ and $\phi_{1,2}$ and two different inverse widths $w_{1,2}$ and $v_{1,2}$. This is observed numerically for large Damköhler numbers and also for small Lewis numbers, when the reaction zone becomes narrow (see Fig. 6.1). In this work, we shall restrict our attention to test functions of the type (6.16) to describe the solution behaviour far from the saddle-node.

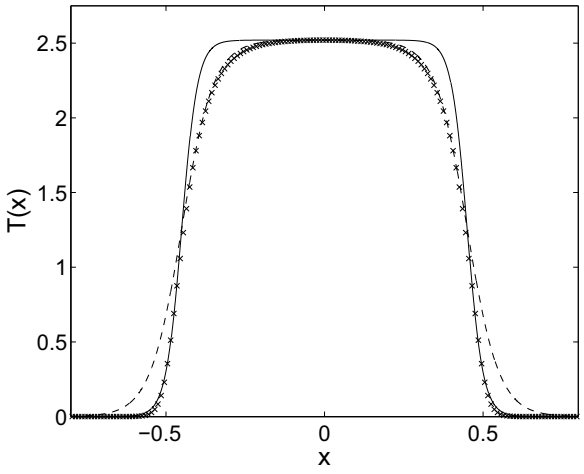

(a)

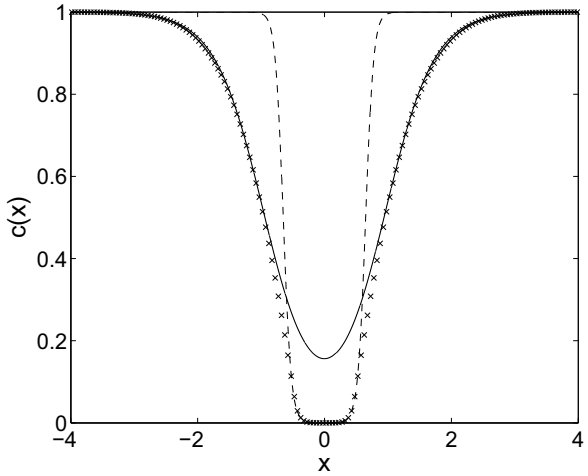

(b)

Figure 6.1: The profiles of the stable steady-state solutions of the flame filament system obtained from the numerical solution of (6.6)-(6.7) for $Le = 0.01$ and $Da = 500$ (represented by crosses). Two fits to each profile using tanh-based test functions (6.16) for a choice of parameters $\{p_{T_i}\} = \{f_0, w, \mu\}$ for the temperature and $\{p_{c_i}\} = \{g_0, v, \phi\}$ for the concentration are also represented. (a) Profile of the temperature $T(x)$ with fits obtained using parameters $\{2.52, 20, 0.45\}$ (represented by a continuous line) and $\{2.52, 10, 0.45\}$ (represented by a dashed line). (b) Profile of the concentration $c(x)$ with fits obtained using parameters $\{1, 1.3, 0.95\}$ (represented by a continuous line) and $\{1, 8, 0.65\}$ (represented by a dashed line).

On substituting the ansatz (6.13) into the steady state equations (6.11)-(6.12), we obtain

$$w^2\,Le\,\Theta_{\eta\eta} + \eta\,\Theta_\eta + Da\;(1-\Omega)\;K(\Theta) \;=\; \varkappa_1(\eta)\,, \tag{6.17}$$

$$v^2\,\Omega_{\zeta\zeta} + \zeta\,\Omega_\zeta + Da\;(1-\Omega)\;K(\Theta) \;=\; \varkappa_2(\zeta)\,. \tag{6.18}$$

where $\varkappa_1(\eta)$ and $\varkappa_2(\zeta)$ are the errors made by this restriction. The free parameters $\{p_i\}$ are determined by minimising these errors. We do this as described in Chapter 3 by projecting (6.17) and (6.18) onto the tangent spaces spanned by $\partial T/\partial p_{T_i}$ and $\partial c/\partial p_{c_i}$ respectively, and setting the projections to zero. The number of basis functions depends on our choice of test function. If we take Θ and Ω to be bell-shaped test functions of the type (6.14) or (6.15), which are parameterised by $\{p_i\} = \{f_0, w, g_0, v\}$, we have four basis functions

$$\frac{\partial T}{\partial f_0} = \frac{\Theta}{f_0}\,, \qquad \frac{\partial T}{\partial w} = \frac{\eta\,\Theta_\eta}{w}\,, \tag{6.19}$$

and

$$\frac{\partial c}{\partial g_0} = -\frac{\Omega}{g_0}\,, \qquad \frac{\partial c}{\partial v} = -\frac{\zeta\,\Omega_\zeta}{v}\,, \tag{6.20}$$

For the combination of test functions of the type (6.16), which are parameterised by $\{p_i\} = \{f_0, w, \mu, g_0, v, \phi\}$, we have six basis functions

$$\begin{aligned} &\frac{\partial T}{\partial f_0} = \frac{\Theta}{f_0}\,, \qquad \frac{\partial T}{\partial \mu} = \frac{f_0\,w}{2}\,(s_1+s_2)\;, \\ &\frac{\partial T}{\partial w} = \frac{f_0}{2\,w}\,(\eta\,(s_1-s_2) + \mu\,w\,(s_1+s_2))\;, \end{aligned} \tag{6.21}$$

where we have defined $s_1 = \operatorname{sech}^2(\eta + \mu\,w)$ and $s_2 = \operatorname{sech}^2(\eta - \mu\,w)$, and

$$\begin{aligned} &\frac{\partial c}{\partial g_0} = -\frac{\Omega}{g_0}\,, \qquad \frac{\partial c}{\partial \phi} = -\frac{g_0\,v}{2}\,(s_3+s_4)\;, \\ &\frac{\partial c}{\partial v} = -\frac{g_0}{2v}\,(\zeta\,(s_3-s_4) + \phi\,v\,(s_3+s_4))\;, \end{aligned} \tag{6.22}$$

where $s_3 = \operatorname{sech}^2(\zeta + \phi\,v)$ and $s_4 = \operatorname{sech}^2(\zeta - \phi\,v)$.

Setting the projections of (6.17) and (6.18) onto the respective tangent space to zero, we have the conditions

$$\langle w^2\,Le\,\Theta_{\eta\eta} + \eta\,\Theta_\eta + Da\;(1-\Omega)\;K(\Theta) \mid \partial\Theta/\partial p_{T_i}\rangle_\eta \;=\; 0\,, \tag{6.23}$$

$$\langle v^2\,\Omega_{\zeta\zeta} + \zeta\,\Omega_\zeta + Da\;(1-\Omega)\;K(\Theta) \mid \partial\Omega/\partial p_{c_i}\rangle_\zeta \;=\; 0\,, \tag{6.24}$$

These are four (in the case of bell-shaped functions) or six (in the case of the test function (6.16)) algebraic equations for the respective four or six parameters. We however find that for any choice of test functions these conditions cannot give explicit analytical results because of the complicated nature of the $K(\Theta)$ term. We therefore apply iterative root finding methods to obtain the parameters $\{p_i\}$ numerically.

In the next section, we will use this method to study the solution behaviour near the saddle-node bifurcation. The accuracy of the results obtained via this method will be examined for different values of Le. We shall then examine the solution behaviour far away from the saddle-node in Sec. (6.5).

6.4 Solution behaviour near the saddle-node

Close to the bifurcation point the solution profiles obtained from a numerical solution of the full system (6.11)-(6.12) are found to be bell-shaped and, as discussed in the previous section, can be approximated by various test functions. In this section we shall examine the solution behaviour in this regime using the nonperturbative method. We shall numerically solve the conditions (6.23)-(6.24) to obtain values for the parameters of the test functions over a range of the Damköhler and Lewis numbers. We shall compare these results with those obtained by numerically solving the system (6.11)-(6.12) at the corresponding values of Da and Le.

6.4.1 Small Lewis numbers

In the small Lewis number or "gaseous" regime, where the heat conduction is much less than the diffusivity of the reactant, the reaction zone is narrow and we can obtain values of $T(x)$ greater than 1 within the product zone without much consumption of the reactant (i.e. we can have temperatures greater than the burnt temperature T_b in the unscaled system (6.3)-(6.4)). However, on increasing Da the temperature within the product zone approaches the burnt temperature from above. Simultaneously, the central value of the stable branch of the concentration reaches $c(x) = 0$.

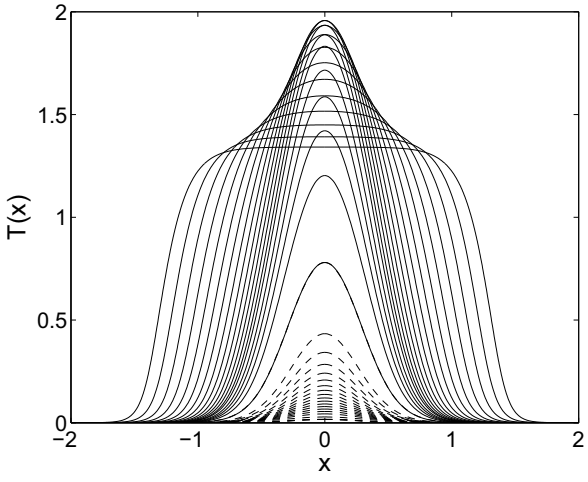

(a)

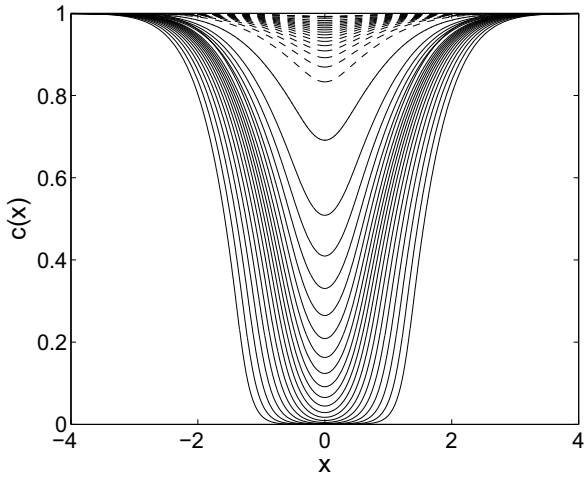

(b)

Figure 6.2: The profiles of the steady-state solutions of the flame filament system (6.11)-(6.12) for $Le = 0.1$. The system is evaluated at logarithmically spaced values of Da between $Da = 4.62\,(\approx Da_c)$ and $Da = 150$. The stable solutions are represented by continuous lines and the unstable solutions are represented by dashed lines. (a) Profiles of the temperature $T(x)$. (b) Profiles of the concentration $c(x)$.

The behaviour of the solution for small values of the Lewis number ($Le = 0.1, 0.01$) was investigated numerically. We found that for $Le = 0.01$ there are two different exponential decay rates in the region of the reaction

zone, one linking the product zone with the reaction zone, and another linking the preheat zone with the reaction zone (see Fig. 6.1). As discussed in Sec. 6.3, in order to fully describe the behaviour in this regime we would therefore require two composite tanh-based test functions, each with two different widths $\mu_{1,2}$ and $\phi_{1,2}$ and two different inverse widths $w_{1,2}$ and $v_{1,2}$. This behaviour is also observed in the case $Le = 0.1$, albeit much less pronounced than for smaller values of Le. Nevertheless, we find that for this value of Le the simpler tanh-based test function (6.16) is sufficient to describe the solution near the saddle-node fairly accurately.

In Fig. 6.2, we show profiles of the temperature and concentration obtained from the numerical simulation of the full system (6.11)-(6.12) using a shooting method for $Le = 0.1$. We find that both the stable and unstable solutions of $T(x)$ and $1 - c(x)$ are bell shaped near Da_c, and becomes plateau-like for larger values of Da. We see that the transition of the profiles from bell-shaped to plateau-like is very slow. As we move away from the critical value Da_c, we find that the stable solution for $T(x)$ first increases in amplitude, and then decreases slowly. The largest change of $T(x)$ with respect to the Damköhler number occurs close to Da_c. We find that the unstable solution remains bell-shaped (with decreasing steepness) even far from the saddle-node.

We describe the bell-shaped solution behaviour near the saddle-node using Gaussian test functions (6.14) as well as sech^2-functions (6.15). We shall therefore solve the conditions (6.23)-(6.24) over a range of Da using these test functions, and obtain values for the amplitudes f_0 and $1 - g_0$ and the inverse widths w and v for each case.

In Fig. 6.3a, we see a comparison between the results for f_0 obtained using the nonperturbative method (for each of the test functions) and the amplitudes of $T(x)$ obtained from numerical simulations of the full system (6.11)-(6.12). The corresponding results for the amplitudes of $1 - c(x)$ are shown in Fig. 6.3b. The results are obtained over a range of Da, and we see that we have good agreement between the numerical and test function results near the saddle-node. The results obtained using Gaussian test functions (6.14) are a good fit to the solution, in accordance with the asymptotic analysis of Sec. 2.3. Moreover, these results closely match up with the results obtained using sech^2-functions (6.15), thus validating our assertion that in this system the exact choice of bell-shaped test function for the nonperturbative method will not greatly affect the results. For the remaining calculations, we restrict to Gaussian test functions to describe bell-shaped profiles.

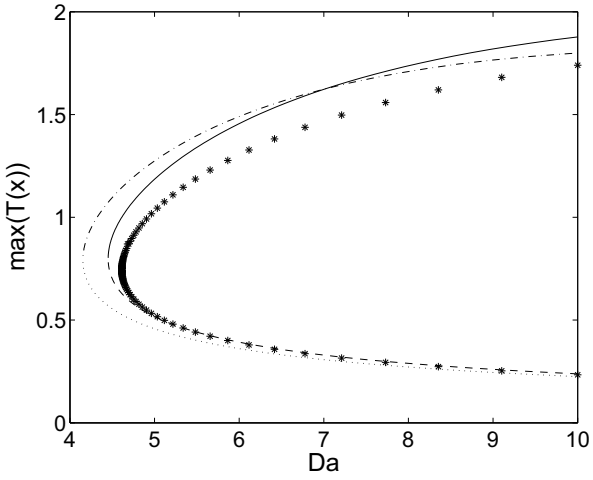

(a)

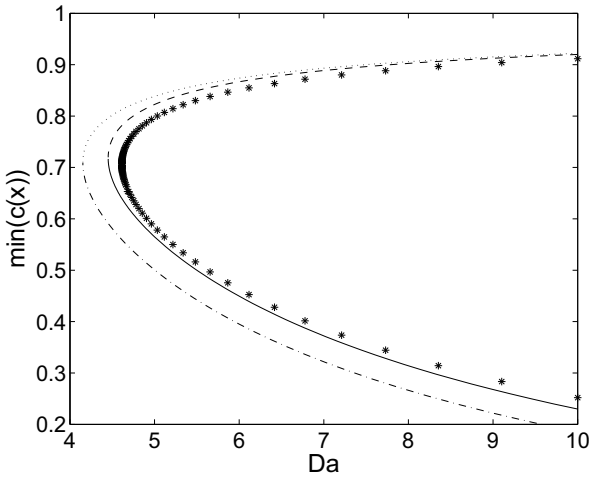

(b)

Figure 6.3: Comparison of the amplitudes of the profiles of the stationary solutions, obtained from the full system of ordinary differential equations (6.11)-(6.12) via shooting methods (represented by stars), with the corresponding results obtained using the nonperturbative method with bell-shaped test functions over a range of Da for $Le = 10$. We use a Gaussian test function (6.14) (represented by a continuous line and a dashed line for the stable and unstable branches respectively) and a sech^2-function (6.15) (denoted by a dash-dotted line and a dotted line for the stable and unstable branches respectively). (a) The maximal values of $T(x)$. (b) The minimal values of $c(x)$.

The fit of the test function to the numerical results remains good along the unstable branch as we increase Da, which is to be expected from the fact that the profiles of the unstable solutions remains bell-shaped for all Da. However, the fit along the stable branch slowly gets worse as we increase Da. This corresponds to the fact that the profiles of both $T(x)$ and $1-c(x)$ become plateau-like as we move away from the saddle-node.

To compare results for the inverse widths of a Gaussian test function obtained using the nonperturbative method with the corresponding results obtained from the numerical simulations, the values of w and v of the solutions of the full system (6.11)-(6.12) need to be measured. To do this, we locate the half-width at half-maximum $\bar{x}$ of each of the profiles of $T(x)$ and $1-c(x)$. Assuming a Gauss-like behaviour, this implies

$$w = \frac{\sqrt{\ln(2)}}{\bar{x}}\,. \tag{6.25}$$

We observe that the test function results for w and v match up closely with the results obtained from the numerical simulations (see Fig. 6.4). We note that the results for v are not as good as those for w, which can be understood from the aforementioned change of functional behaviour in the reaction zone (see Fig. 6.2b).

We now describe the behaviour of the maximal amplitude of the stable solution of the temperature as a function of the Damköhler number, as we move away from the saddle-node. From Fig. 6.2 we see that the amplitude of the stable solution of the temperature first increases and then subsequently decreases. This can be captured by the nonperturbative method. In Fig. 6.5 we show a comparison of the nonperturbative method with numerical results obtained from the solution of (6.6)-(6.7) over a range of Da for which this behaviour is observed. We show results for a Gaussian test function and also for the more versatile tanh-based test function (6.16). For values of Da greater than $Da \approx 18.82$ the nonperturbative method will not yield a real solution with a Gaussian test function, and hence this test function cannot fully describe this region. We find that the tanh-based test function captures the behaviour much better over the range of Da since it allows for more functional flexibility (see Fig. 3.1) and can describe the transition from a bell-shaped to a plateau like functional form. This versatile test function could also be used for the description of the solution behaviour near the saddle-node. However, as root finding methods become increasingly sensitive to correct initial guesses in higher dimensions and require much greater computational effort, we shall restrict our attention to bell-shaped test functions close to the saddle-node.

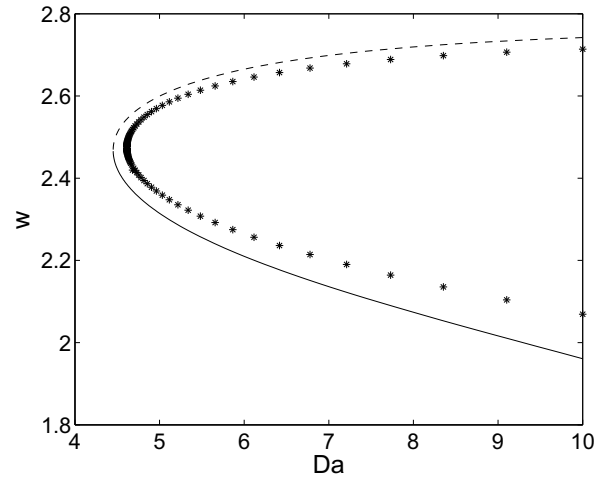

(a)

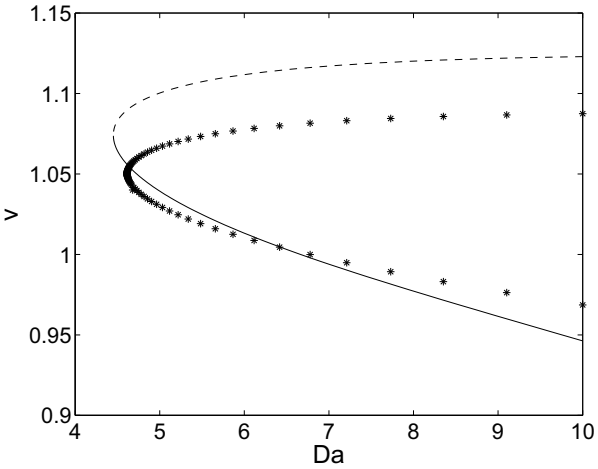

(b)

Figure 6.4: Comparison of the inverse widths of the profiles of the stationary solutions, obtained from the full system of ordinary differential equations (6.11)-(6.12) via shooting methods (represented by stars), with the corresponding results obtained using the nonperturbative method with a Gaussian test function (6.14) (represented by a continuous line and a dashed line for the stable and unstable branches respectively) over a range of Da for $Le = 0.1$. (a) The inverse widths of the profiles of the temperature w. (b) The inverse widths of the profiles of the concentration v.

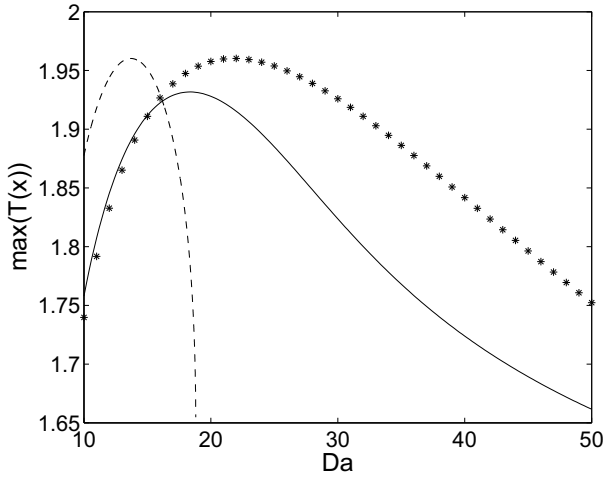

Figure 6.5: Comparison of the amplitudes of the profiles of the stable stationary solutions of $T(x)$, obtained from the full system of ordinary differential equations (6.11)-(6.12) via a shooting method (represented by stars), with the corresponding results obtained using the nonperturbative method with a tanh-based test function (6.16) (represented by a continuous line) and a Gaussian test function (represented by a dashed line) over a range of Da for $Le = 0.1$.

6.4.2 Equal diffusion: $Le = 1$

In the case $Le = 1$ the system can be simplified to give $c(x) = 1 - T(x)$. Consequently, the equations (6.11)-(6.12) collapse into a single equation, allowing us to use a single test function to describe the behaviour of the system. The profiles of the solution in this case are shown in Fig. 6.6. The solution near the saddle-node is again found to be bell-shaped. For this case, we find that the transition of the profile shape of the stable solutions from bell-shaped to plateau-like is much quicker and the reaction zone is wider than it is for smaller Le. As before, the unstable solution profiles remain bell-shaped as we increase Da.

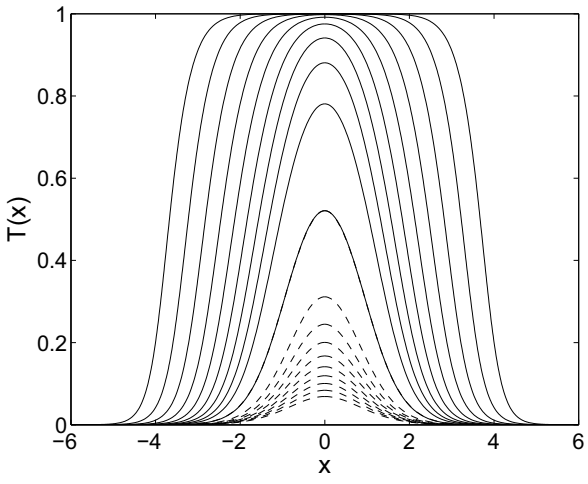

(a)

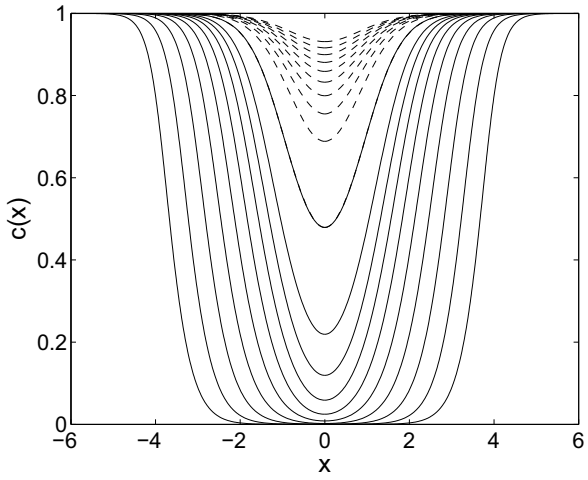

(b)

Figure 6.6: The profiles of the steady-state solutions of the flame filament system (6.11)-(6.12) for $Le = 1$. The system is evaluated at logarithmically spaced values of Da between $Da = 6.963\,(\approx Da_c)$ and $Da = 50$. The stable solutions are represented by continuous lines and the unstable solutions are represented by dashed lines. (a) Profiles of the temperature $T(x)$. (b) Profiles of the concentration $c(x)$.

To capture the solution behaviour in this regime we shall again use Gaussian test functions (6.14). From the above relation $c(x) = 1 - T(x)$, we have $g_0 = f_0$ and $v = w$. We compare the values of f_0 obtained from

the nonperturbative method with the corresponding amplitudes of $T(x)$ in Fig. 6.7a. In Fig. 6.7b, we compare the results for w with the corresponding values for the inverse width of $T(x)$ (calculated using (6.25)). In both cases, we find good agreement between the two sets of results near the saddle-node. However we see that the fit quickly deviates from the solution for the stable branch, in accordance with the numerical observation that the stable solutions quickly become plateau-like as we move away from the saddle-node. In further agreement with our numerical observation, we find that the fit along the unstable solution branch is good even at larger values of Da.

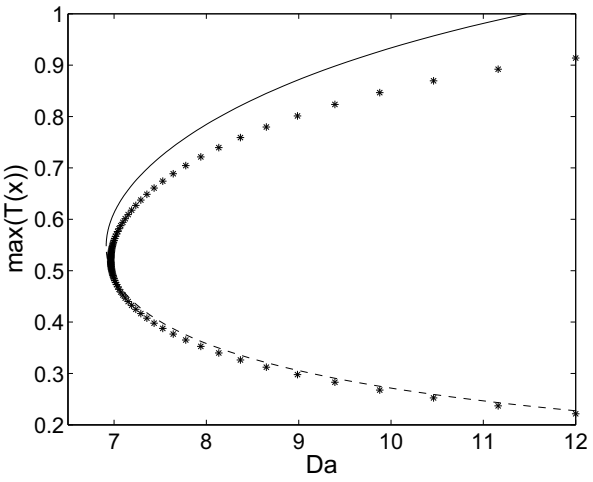

(a)

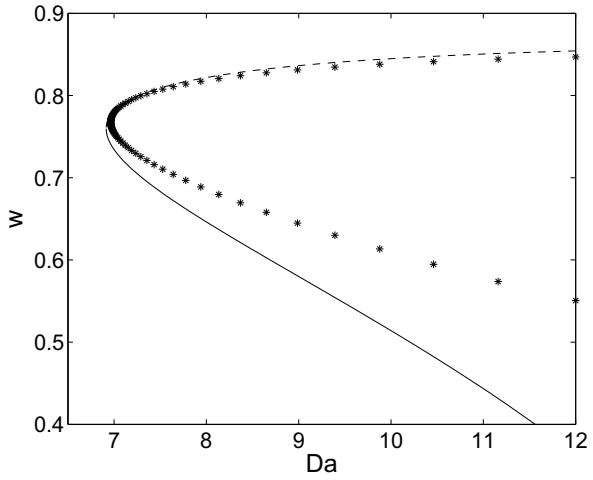

(b)

Figure 6.7: Comparison of the amplitudes and inverse widths of the profiles of the stationary solutions, obtained from the full system of ordinary differential equations (6.11)-(6.12) via shooting methods (represented by stars), with the corresponding results obtained using the nonperturbative method with a Gaussian test function (6.14) (represented by a continuous line and a dashed line for the stable and unstable branches respectively) over a range of Da for $Le = 1$. (a) The maximal values of $T(x)$. (b) The inverse widths of the temperature profiles w.

6.4.3 Large Lewis numbers

In the large Lewis number or "solid" regime, where the heat conduction is much larger than the diffusivity of the reactant, we obtain values of $T(x)$ less than 1 in the reaction zone (i.e. we have temperatures less than the burnt temperature T_b in the unscaled system (6.3)-(6.4)). Systems of this type have a much broader reaction zone than those corresponding to smaller Le, and require more consumption of fuel to increase the temperature. On increasing Da, the central temperature slowly increases to the burnt temperature from below, while the central value of the concentration quickly moves to $c(x) = 0$.

The behaviour of the solution for a range of large values of Lewis numbers ($Le = 10, 100, 1000$) was investigated numerically. We find that for large Lewis numbers, the extent of the product zone is extremely large and the reaction zone is very wide even for relatively small values of Da. We find that a value of $Le = 10$ exhibits important features observed in the large Le limit, and that a smaller box length is sufficient in this case. We shall therefore use the nonperturbative method to analyse the solution near the saddle-node for this value of Le.

In Fig. 6.8, we show profiles of the temperature and concentration. As we move away from the saddle-node we find that the solution profile along the stable branch very quickly moves from bell-shaped to plateau-like. As a result, the range for which a bell-shaped test function is a good fit is greatly diminished. The solution close to the bifurcation point can therefore be better approximated by a plateau-like test function. The tanh-based test function (6.16) is particularly useful in this regard, as it allows us to capture bell-shaped as well as plateau-like profiles (see Fig. 3.1). In this region we shall consider both Gaussian test functions (6.14) as well as the tanh-based test function to describe the solution behaviour near Da_c. We solve the conditions (6.23)-(6.24) to obtain results for the parameters $\{p_i\} = \{f_0, w, g_0, v\}$ (in the case of a Gaussian) or $\{p_i\} = \{f_0, w, \mu, g_0, v, \phi\}$ (in the case of the tanh-based test function (6.16) over a range of Da near the saddle-node.

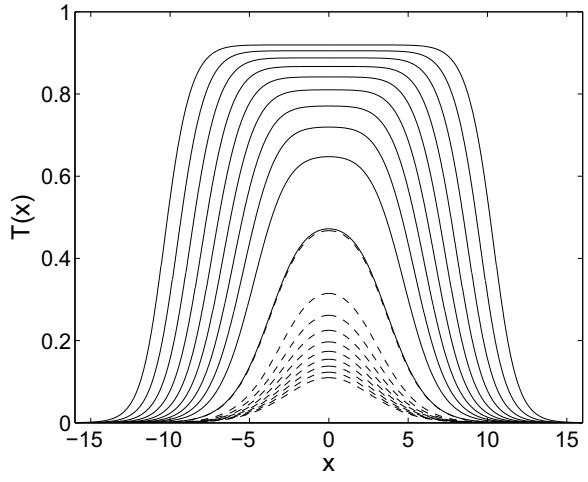

(a)

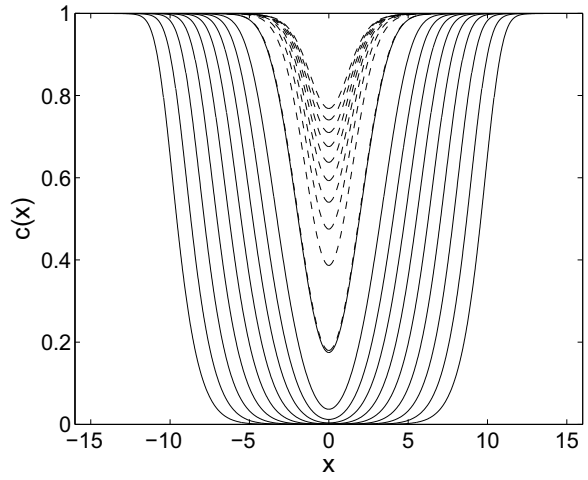

(b)

Figure 6.8: The profiles of the steady-state solutions of the flame filament system (6.11)-(6.12) for $Le = 10$. The system is evaluated at logarithmically spaced values of Da between $Da = 8.462\,(\approx Da_c)$ and $Da = 30$. The stable solutions are represented by continuous lines and the unstable solutions are represented by dashed lines. (a) Profiles of the temperature $T(x)$. (b) Profiles of the concentration $c(x)$.

In Fig. 6.9a, we see a comparison between the amplitudes of the profiles of $T(x)$ and $1 - c(x)$ obtained from numerical simulations of the full system (6.11)-(6.12) and the corresponding results obtained using the nonperturba-

tive method (with each of the test functions). Again, the solution along the unstable branch is well approximated by a Gaussian, and this fit improves further as we increase Da. However, a Gaussian test function does not approximate the solution near the saddle-node as well as it does for smaller values of Le, and the fit of this test function along the stable branch is not as good. This is to be expected from the fact that the solution along the stable branch is no longer bell-shaped (see Fig. 6.8), and is further illustrated in Fig. 6.10, where the values of w obtained with a Gaussian test function are compared with the corresponding numerical results (calculated using (6.25)). We find that test functions of the type (6.16) provide much better fits to the amplitudes of the solution near the saddle-node as well as along both branches (see Fig. 6.9). This is due to the fact that the more versatile tanh-based test functions can capture both bell-shaped and plateau-like profiles, as discussed in Sec. 6.4.1.

To compare results for the remaining four parameters of test function (6.16) obtained using the nonperturbative method with the corresponding results obtained from the numerical simulations, the values of w, v, μ and ϕ of the solutions of the full system (6.11)-(6.12) need to be measured. To do this, we locate the values of x where $T(x)$ and $1-c(x)$ are three quarters and one quarter of their maximal values at $x=0$. This yields two equations for the temperature

$$\tanh\left(w(x_1+\mu)\right)-\tanh\left(w(x_1-\mu)\right)=\frac{3}{2}\tanh\left(w\,\mu\right)\,, \tag{6.26}$$

$$\tanh\left(w(x_2+\mu)\right)-\tanh\left(w(x_2-\mu)\right)=\frac{1}{2}\tanh\left(w\,\mu\right)\,, \tag{6.27}$$

where x_1 and x_2 are the values of x where $T(x)=3T(0)/4$ and $T(x)=T(0)/4$ respectively, and two for the concentration

$$1-\frac{g_0}{2}\left(\tanh\left(v(x_3+\phi)\right)-\tanh\left(v(x_3-\phi)\right)\right)=\frac{3}{4}\left(1-g_0\tanh\left(\phi\,v\right)\right)\,, \tag{6.28}$$

$$1-\frac{g_0}{2}\left(\tanh\left(v(x_4+\phi)\right)-\tanh\left(v(x_4-\phi)\right)\right)=\frac{1}{4}\left(1-g_0\tanh\left(\phi\,v\right)\right)\,, \tag{6.29}$$

where x_3 and x_4 are the values of x where $1-c(x)=3(1-c(0))/4$ and $1-c(x)=(1-c(0))/4$ respectively. These implicit equations for w, v, μ and ϕ can be solved numerically using iterative root finding methods. We compare the values of the inverse widths of the solution profiles, w and v, in Figs. 6.11, and the widths of the solutions, μ and ϕ, in Fig. 6.12. We observe that the results obtained using the test function (6.16) are again much better fits to the solution than the corresponding results obtained using Gaussian test functions.

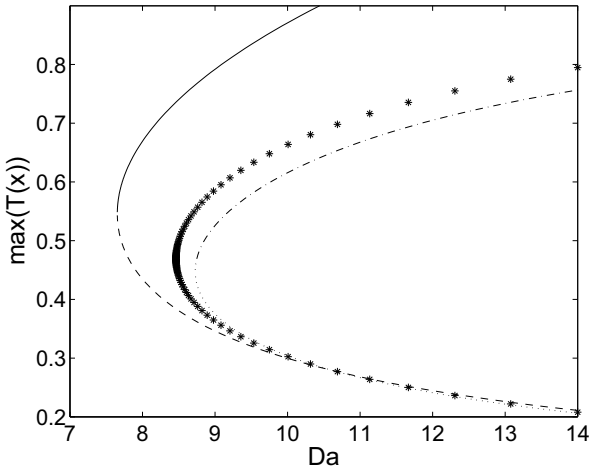

(a)

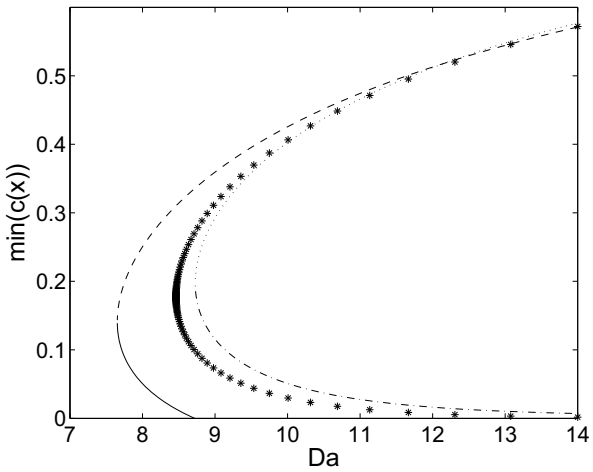

(b)

Figure 6.9: Comparison of the amplitudes of the profiles of the stationary solutions, obtained from the full system of ordinary differential equations (6.11)-(6.12) via shooting methods (represented by stars), with the corresponding results obtained using the nonperturbative method with two different test functions over a range of Da for $Le = 10$. We use a Gaussian test function (6.14) (represented by a continuous line and a dashed line for the stable and unstable branches respectively) and the test function (6.16) (denoted by a dash-dotted line and a dotted line for the stable and unstable branches respectively). (a) The maximal values of $T(x)$. (b) The minimal values of $c(x)$.

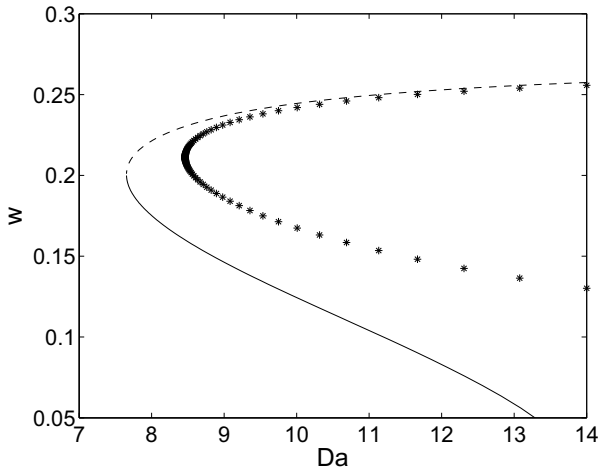

(a)

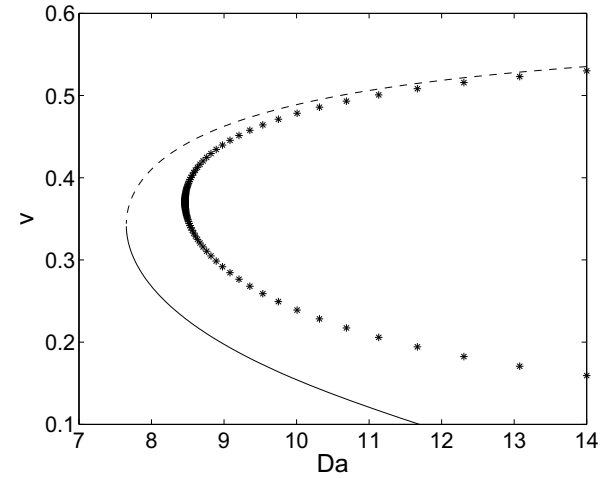

(b)

Figure 6.10: Comparison of the inverse widths of the profiles of the stationary solutions, obtained from the full system of ordinary differential equations (6.11)-(6.12) via shooting methods (represented by stars), with the corresponding results obtained using the nonperturbative method with a Gaussian test function (6.14) (represented by a continuous line and a dashed line for the stable and unstable branches respectively) over a range of Da for $Le = 10$. (a) The inverse widths of the profiles of the temperature w. (b) The inverse widths of the profiles of the concentration v.

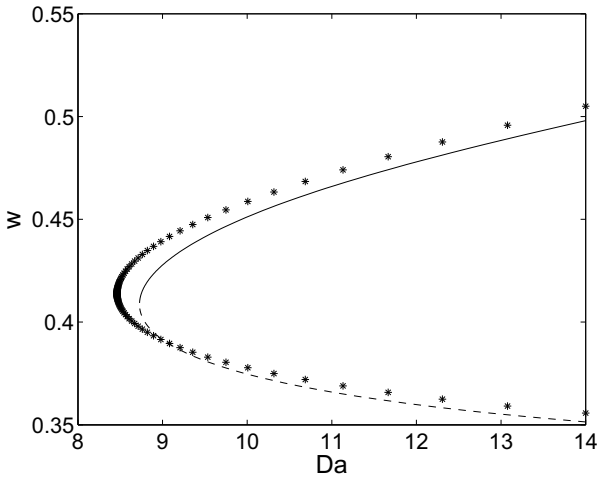

(a)

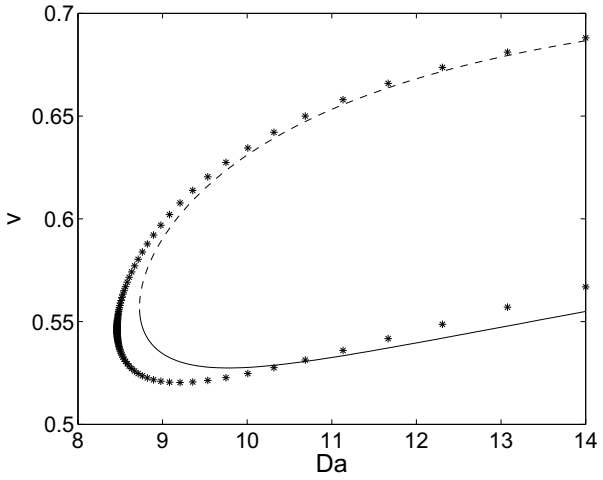

(b)

Figure 6.11: Comparison of the inverse widths of the profiles of the stationary solutions, obtained from the full system of ordinary differential equations (6.11)-(6.12) via shooting methods (represented by stars), with the corresponding results obtained using the nonperturbative method with the test function (6.16) (represented by a continuous line and a dashed line for the stable and unstable branches respectively) over a range of Da for $Le = 10$. (a) The inverse widths of the profiles of the temperature w. (b) The inverse widths of the profiles of the concentration v.

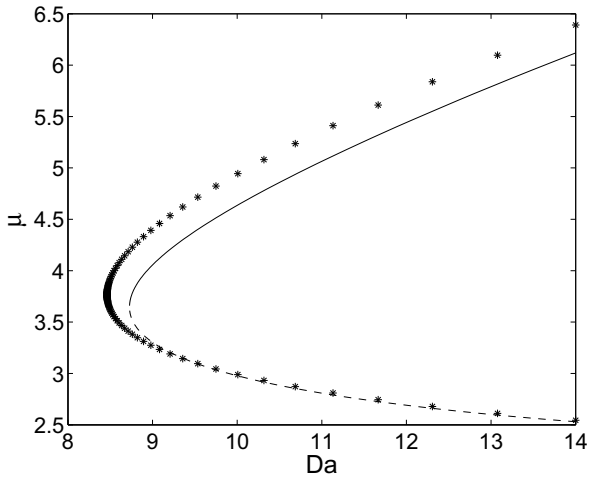

(a)

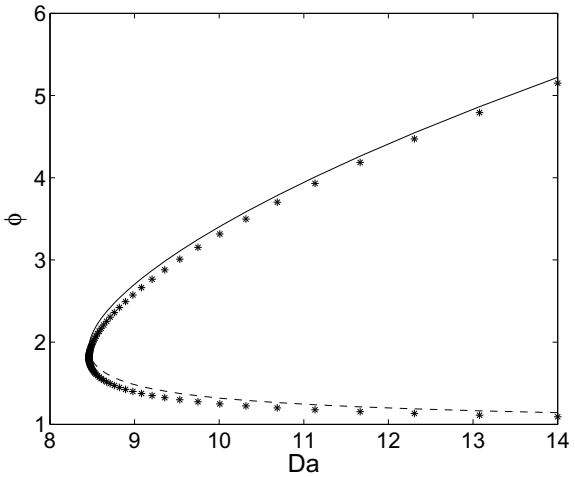

(b)

Figure 6.12: Comparison of the widths of the profiles of the stationary solutions, obtained from the full system of ordinary differential equations (6.11)-(6.12) via shooting methods (represented by stars), with the corresponding results obtained using the nonperturbative method with the test function (6.16) (represented by a continuous line and a dashed line for the stable and unstable branches respectively) over a range of Da for $Le = 10$. (a) The widths of the profiles of the temperature μ. (b) The widths of the profiles of the concentration ϕ.

6.4.4 The solution at the saddle-node

The solution behaviour of this system at the saddle-node bifurcation depends strongly on the value of Le. A numerical analysis of the system (6.6)-(6.7) reveals that the critical Damköhler increases with the Lewis number. In the limit of large Le, the value saturates around $Da_c \approx 8.5$. In Fig. 6.13, we compare these values of Da_c with the corresponding critical values of Da obtained using the nonperturbative method (with different test functions) over a range of Le. For low values of Le we find that the critical Damköhler number can be well approximated with both a Gaussian test function (6.14) as well as a tanh-based test function (6.16) which, as discussed in Sec. 6.4.1, is more versatile. For larger values of Le, the tanh-based test function ansatz is better suited to calculate Da_c, as we have already seen in Sec. 6.4.3, due to the rapid transition in solution profile from bell-shaped to plateau-like as we move away from the saddle-node.

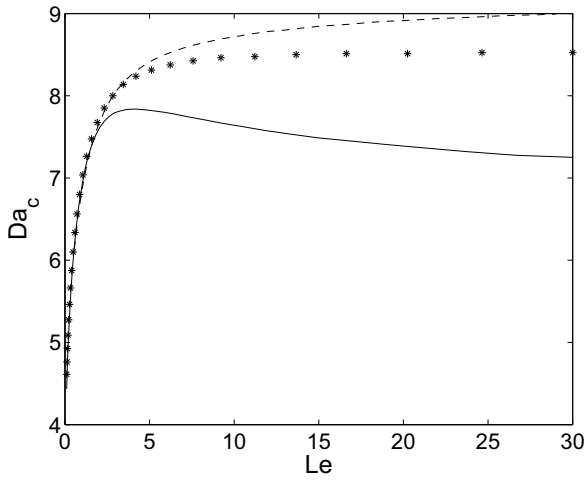

Figure 6.13: Comparison of the values of the critical Damköhler number, obtained by numerically integrating the full system (6.6)-(6.7) (represented by stars), with the corresponding results obtained using the nonperturbative method with different test functions over a range of Le. We use a Gaussian test function (6.14) (represented by a continuous line) and the test function (6.16) (represented by a dashed line).

The critical Damköhler number is also found to depend on the system parameter ϵ [63]. From (6.10), we see that this parameter is proportional to the inverse of the activation energy. A comparison between the numerically obtained values of Da_c and those obtained using the nonperturbative method

with a Gaussian test function (6.14) over a range of ϵ at $Le = 0.1$ reveals that a Gaussian test function is an excellent fit to the solution, and improves further for higher values of ϵ (see Fig. 6.14). This corresponds to our result in Sec. 6.4.1, where we observed that Gaussian test functions provided a good fit to the solution near Da_c for $Le = 0.1$ and $\epsilon = 1$.

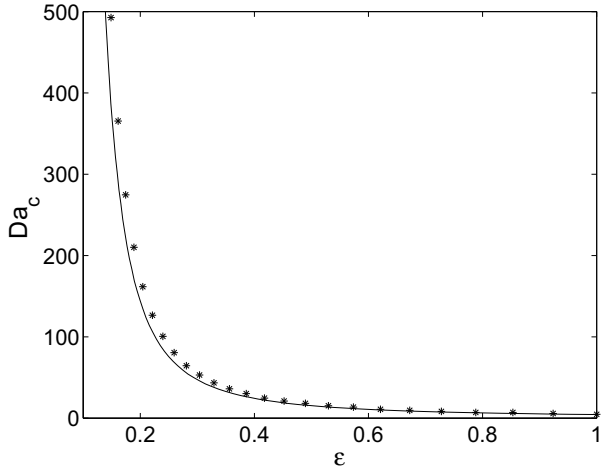

Figure 6.14: Comparison of the values of the critical Damköhler number, obtained by numerically integrating the full system (6.6)-(6.7) (represented by stars), with the corresponding results obtained using the nonperturbative method with a Gaussian test function (6.14) (represented by a continuous line) over a range of the parameter ϵ for $Le = 0.1$.

6.5 Comparison of results far from the saddle-node

For large values of Da we observe plateau-like profiles for the stable solutions of both $T(x)$ and $c(x)$, while the unstable solutions are found to decrease in amplitude and steepness while remaining bell-shaped (as seen in Figures 6.2, 6.6 and 6.8). As described in Sec. 6.4, unstable solutions are well approximated by bell-shaped test functions and this fit remains good even for large Da. In this section we shall analyse the solutions along the stable branch.

The solution in this regime can be described using test functions of the type (6.16). In the limiting case of large Da, we can make some approximations which greatly simplify the calculations. Firstly, we note that far

away from the saddle-node ($Da \gg Da_c$) the concentration of the fuel in the product zone is $c(x) = 0$ as the reactant is completely used up, while the temperature in this region is a constant maximum value $T(x) = 1$. We can therefore fix $f_0 = g_0 = 1$ for our test functions (6.16). Secondly, we note that for all values of Le there is a large central region in which the reactant is fully consumed. The extent of this product zone is found to increase with $\sqrt{Da}$. This relates to our asymptotic theory in Sec. 2.3. Moreover, the widths of the profiles of $T(x)$ and $c(x)$ become closer as Da increases. We can therefore fix $\phi = \mu$ for our test functions (6.16). A final simplification can be made by using the phenomenological argument discussed in Sec. 2.2. The stationary solutions of the system are obtained when there is a balance between the velocity of the travelling front V_0 and the chaotic stirring x. A solution with a product zone of width μ is therefore obtained when $\mu = V_0$, and we shall make this assumption. This value of v_0 is undetermined and has to be calculated. This leaves two free parameters w and v, which can be determined using the nonperturbative method.

We now present an empirical formula for the wave speed V_0 of unstirred combustion fronts. For simplicity, we denote by Da the reaction kinetics for the unstirred case as well. We determined the wave speed of the unstirred version of the system (6.6)-(6.7) using a shooting algorithm. We observe that V_0 exhibits a $\sqrt{Da}$ behaviour, which is consistent with our asymptotic theory in Chapter 2 where we consider the scaling $\mu \sim \sqrt{Da}$. In particular we find that for large Lewis numbers $V_0 \sim \sqrt{Da\, Le}$ is a good approximation. We note that the scaling behaviour is reminiscent of an underlying autocatalytic structure for large Da. From numerical simulations of the stirred system (6.6)-(6.7), we find that one can crudely approximate $c \approx 1 - T$ and $K(T) \approx \alpha\, T$, where α is a (Lewis number dependent) constant. We determined $V_0(Le)$ numerically for several values of Da ($Da = 100, 500, 1000, 5000, 10000$). A plot of $V_0(Le)$ for $Da = 1000$ is shown in Fig. 6.15.

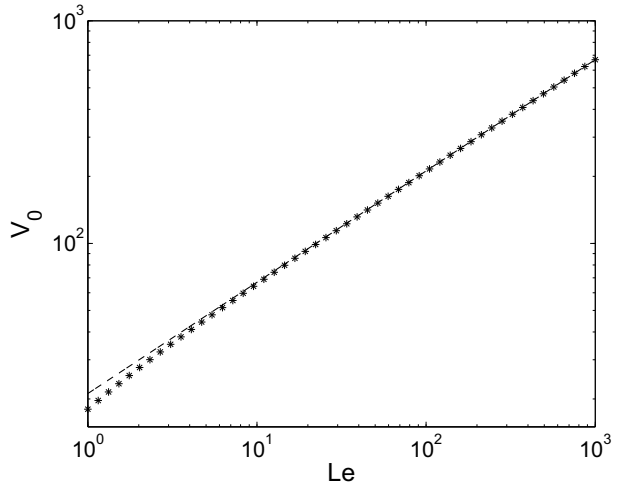

Figure 6.15: Logarithmic plot of the wave speed V_0 obtained from the numerical solution of the unstirred version of the system (6.6)-(6.7) (with reaction kinetics in terms of Da) at $Da = 1000$ (represented by stars). A reference line with slope 1/2 (represented by a dashed line) is also shown.

For large Le the quotient $V_0/\sqrt{Da\,Le}$ reaches a constant value of 0.669 with only very small deviation for the smaller values of the Damköhler number indicating that there is no Da-correction to the square-root behaviour of the velocity. However we can find a Lewis-number correction by employing linear regression. We find as an empirical formula for V_0,

$$V_0 = 0.669\sqrt{Da\,Le}\left(1 - \frac{0.158}{Le}\right) . \tag{6.30}$$

A comparison between the values of V_0 obtained numerically from the solution of the unstirred system over a range of Da for a fixed Le with the corresponding results obtained with this empirical formula reveals that this is an excellent approximation (see Figs. 6.16). This has been verified using several values of a fixed Lewis number ($Le = 1, 10, 25, 50, 1000, 5000, 10000$). A plot of $V_0(Da)$ for $Le = 10$ is shown in Fig. 6.17. This formula is similar in construction to the formula for a different solution branch recently derived analytically in [11].

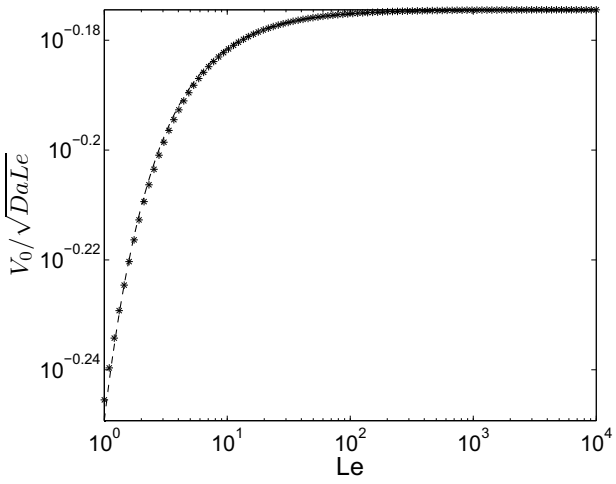

Figure 6.16: Logarithmic plot of $V_0/\sqrt{Da\,Le}$ at $Da = 10000$ (represented by stars). The values of the wave speed V_0 are obtained from the numerical solution of the unstirred version of the system (6.6)-(6.7) (with reaction kinetics in terms of Da). We also plot $0.669(1 - 0.158/Le)$ which arises from our empirical formula (6.30) (represented by a dashed line). Note that this is a close fit for small values of Le as well.

Hence we obtain the following expression for the width from our phenomenological argument

$$\mu = 0.669\sqrt{Da\,Le}\left(1 - \frac{0.158}{Le}\right). \tag{6.31}$$

As seen in Figs. 6.18, 6.19 and 6.20, this phenomenological formula is found to be a good approximation to the widths of the profiles of both $T(x)$ and $c(x)$ for a range of Le. We observe that widths of both profiles tend to the same value in the limit of large Da.

We notice that V_0 decreases (for a fixed Damköhler number) on decreasing the Lewis number (see Fig. 6.15). From (6.1) we see that decreasing the Lewis number is equivalent to increasing the relative importance of D, ρ and C_p in relation to κ. Reducing κ obviously decreases the ability of heat to propagate, and hence the combustion speed. Higher densities result in increased fuel mass in each location, which means more heat is needed in a given area to ignite all of the fuel before the wave moves on. Fuels with increased C_p require more heat to increase the temperature by the a specified amount. Finally, increasing D increases the transport of burnt fuel into the unburnt region and vice-versa, interfering with front propagation.

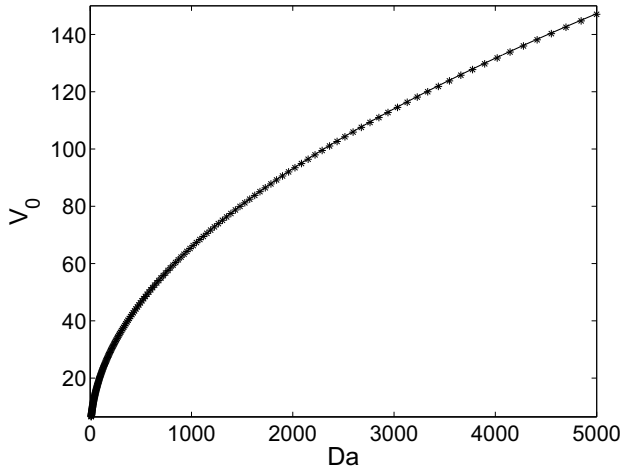

Figure 6.17: Comparison between the values of the wave speed V_0 obtained from the numerical solution of the unstirred version of the system (6.6)-(6.7) (with reaction kinetics in terms of Da) at $Le = 10$ (represented by stars) and the corresponding values obtained from the empirical formula for the wave speed (6.30) (represented by a continuous line).

These simplifications significantly reduce the number of free parameters for the test function (6.16). We have set $f_0 = g_0 = 1$ and $\phi = \mu$ is given by our phenomenological argument (6.31). We can therefore use the nonperturbative method to determine the remaining free parameters w and v of the test functions. From (6.23)-(6.24), we have the projections

$$\langle w^2\, Le\, \Theta_{\eta\eta} + \eta\, \Theta_\eta + Da\ (1-\Omega)\ K(\Theta) \mid \partial\Theta/\partial w \rangle_\eta \ = \ 0\,, \qquad (6.32)$$

$$\langle v^2\, \Omega_{\zeta\zeta} + \zeta\, \Omega_\zeta + Da\ (1-\Omega)\ K(\Theta) \mid \partial\Omega/\partial v \rangle_\zeta \ = \ 0\,, \qquad (6.33)$$

which can be solved to obtain values for w and v. In Fig. 6.21, we compare the profile of the solution obtained from the numerical solution of the system at $Le = 1$ with the corresponding profile of the test function (6.16) whose parameters are obtained by this method. We find a close agreement between the two sets of results.

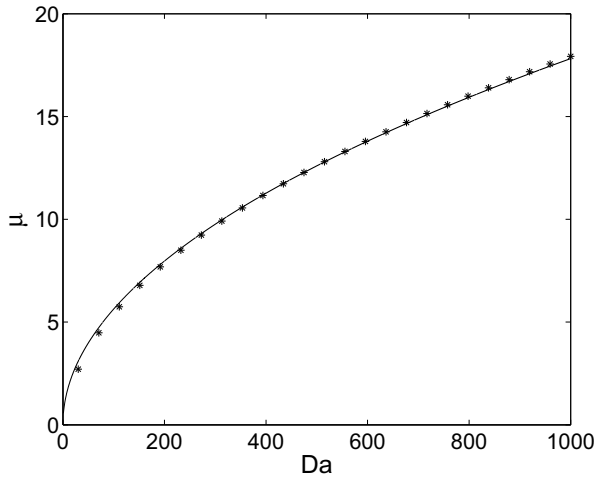

(a)

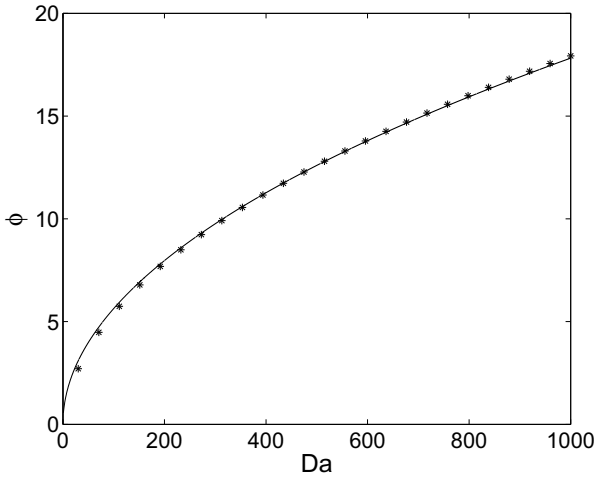

(b)

Figure 6.18: Comparison of the widths of the profiles of the stationary solutions, obtained by numerically integrating the full system (6.6)-(6.7) (represented by stars), with the phenomenological formula for the widths (6.31) (represented by a continuous line) over a range of Da for $Le = 1$. (a) The widths of the profiles of the temperature, μ. (b) The widths of the profiles of the concentration, ϕ.

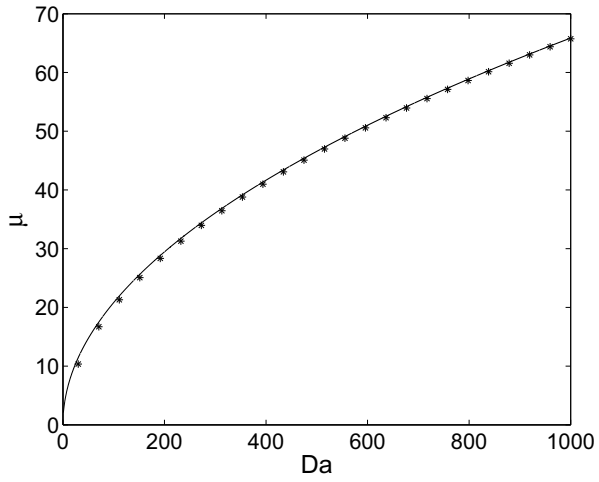

(a)

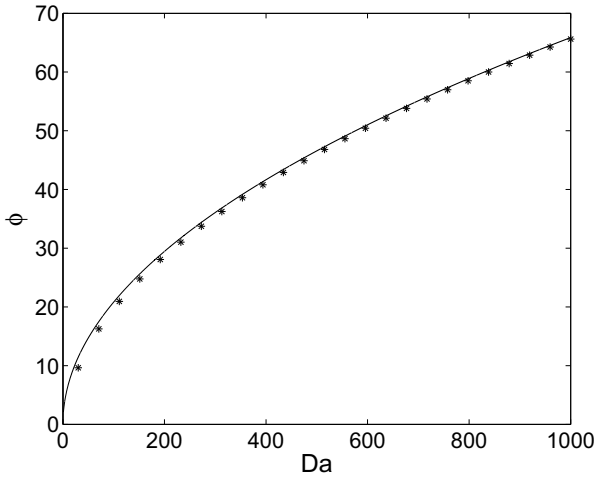

(b)

Figure 6.19: Comparison of the widths of the profiles of the stationary solutions, obtained by numerically integrating the full system (6.6)-(6.7) (represented by stars), with the phenomenological formula for the widths (6.31) (represented by a continuous line) over a range of Da for $Le = 10$. (a) The widths of the profiles of the temperature, μ. (b) The widths of the profiles of the concentration, ϕ.

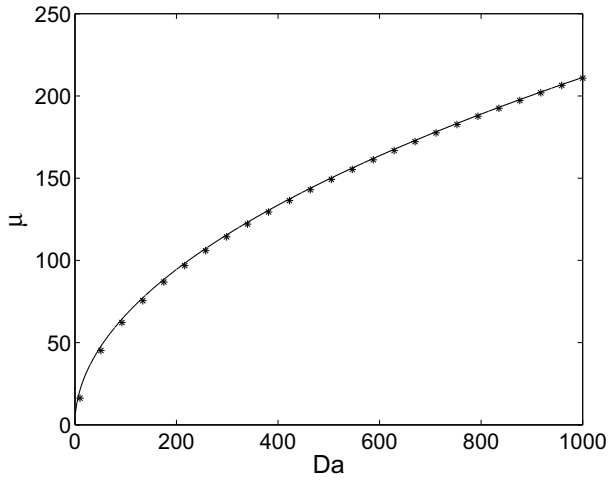

(a)

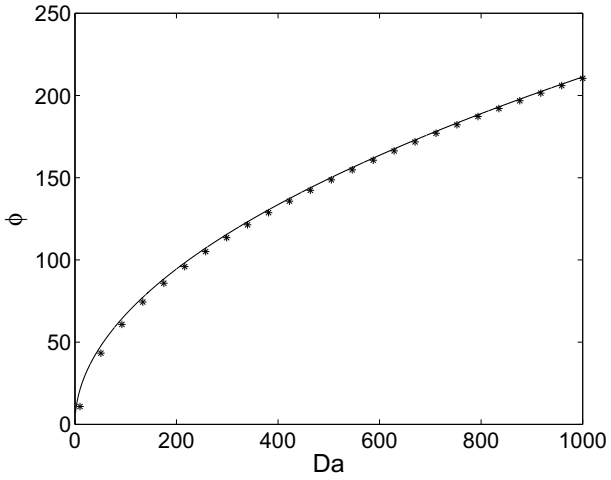

(b)

Figure 6.20: Comparison of the widths of the profiles of the stationary solutions, obtained by numerically integrating the full system (6.6)-(6.7) (represented by stars), with the phenomenological formula for the widths (6.31) (represented by a continuous line) over a range of Da for $Le = 100$. (a) The widths of the profiles of the temperature, μ. (b) The widths of the profiles of the concentration, ϕ.

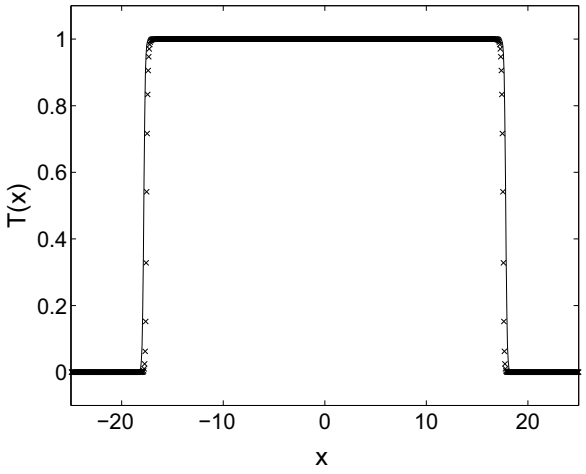

Figure 6.21: The profile of the stable stationary solution of the temperature $T(x)$ at $Le = 1$ and $Da = 1000$, obtained by numerically integrating the full system (6.6)-(6.7) (represented by crosses), superimposed with a test function (6.16) (represented by a continuous line). The width of the test function is given by the phenomenological argument for the widths (6.31), and its inverse width given by the solution of the conditions (6.23)-(6.24) obtained from the nonperturbative method.

6.6 Summary

We studied the effect of chaotic stirring on a combustion system using a reduced 1-D filament model introduced in [64, 63] to describe the cross-filament dynamics. The effect of stirring on this system is to remove heat from the filaments by quenching them. Subsequently a travelling front does not contain enough heat to ignite the preheat zone, and this leads to the unwanted termination of the reaction. For sufficiently small values of the Damköhler number (i.e. for sufficiently large stirring rates) the reaction cannot be sustained. Nontrivial states can only form through the filaments above a critical Damköhler number Da_c.

We used the nonperturbative method discussed in Chapter 3, to determine this critical Damköhler number and to describe the solution behaviour near Da_c. This critical Damköhler number is not very sensitive to variations in the Lewis number for sufficiently large values of Le, and this phenomenon is captured by our method (see Fig. 6.5). The solution behaviour close to criticality was found to be well approximated by bell-shaped test functions such

as a Gaussian test function (6.14) for small Lewis numbers (the "gaseous regime") and by tanh-based test functions (6.16) for large Lewis numbers (the "solid regime"). The solutions along the unstable solution branch could be approximated by bell-shaped functions for all Le.

We then described the solutions for large Damköhler numbers. For small Lewis numbers the temperature approaches the burnt temperature $T = 1$ from above, and higher temperatures can be reached in the product zone. For larger Lewis numbers the burnt temperature is approached for higher Damköhler numbers from above. We note that the largest change of the temperature with respect to the Damköhler number occurs close to the critical Damköhler number. For all Le, the concentration of the reactant c reaches 0 within the product zone already slightly above the critical Damköhler number, corresponding to a full consumption of the fuel within the product zone. The extent of the product zone as a function of the Damköhler number was also described and a clear square-root behaviour was observed. A simple phenomenological argument allowed us to explain this dependence. We have determined an empirical formula for the wave speed of the unstirred combustion system for high Damköhler and high Lewis numbers. This empirical formula allowed us to determine the actual form of combustion fronts far away from the bifurcation with good accuracy.

Chapter 7

Summary

In this thesis, we studied the effect of chaotic stirring on the behaviour of reaction-diffusion systems. In particular we examined the resulting stirring-induced saddle-node bifurcations and described the solution behaviour near these bifurcations. We considered a 1-D filament model for the dynamics of the systems. This model supports stationary solutions which arise from the balance between stirring and diffusion. For a sufficiently large stirring rate the systems do not exhibit any nontrivial solutions and this critical value corresponds to a saddle-node bifurcation.

We used a nonperturbative non-asymptotic method to analyze the solution behaviour of the systems. This method involves restricting the solution space to that of a set of appropriately chosen parameterised test functions, and determining the parameters which minimise the error made by this restriction. This method allowed us to study solution profiles, for instance bell-shaped solutions, which cannot be described using asymptotic matching techniques. In addition to the stirring-induced saddle-node bifurcation, the nonperturbative method was also used to examine several other bifurcations and solution behaviours that arise in such chaotically stirred reaction diffusion systems. To demonstrate this method, we chose several systems with multiple homogeneous steady states.

This method was first used to study two one-component systems. We examined an autocatalytic system where it was found that the solution behaviour near the saddle-node could be well approximated by a Gaussian test function as well as a tanh-based test function. However, when we used a plateau-like test function to describe the solution far from the saddle-node, we found that this method does not yield a unique set of parameters for each value of Da. This is linked to a degeneracy in the limit of large Da, and we found that if we fix the width of the chosen test function using a phenomenological argument, then we can obtain results that match up well with

those of the full system. The other one-component system we considered was the bistable system. For this system, we again find that both a Gaussian as well as a tanh-based test function could be used to approximate the solution profile near the saddle-node. The same tanh-based test function could also be used to accurately describe the solution far from the saddle-node. In both systems, we obtained explicit relations for the parameters near the saddle-node using the Gaussian test function.

We next examined a two-component excitable system with an activator that has a much larger diffusion coefficient than the inhibitor. In addition to the saddle-node due to stirring, this system has a second saddle-node associated with propagation failure which is the generic saddle-node for excitable media. We numerically investigated this system and found a rich and complex bifurcation scenario and solution behaviour. In particular we observed a previously unreported region of bistability characterised by a hysteresis loop. We also observed a region of oscillatory behaviour related to a supercritical Hopf bifurcation. In addition, we found several higher codimension points which connect these bifurcations, near which a range of different solution behaviours were observed. We successfully used the nonperturbative method to describe the solution behaviour near the two saddle-nodes, as well as the various other bifurcation scenarios. Using a Gaussian test function, we obtained explicit relations for the parameters near the saddle-node. We introduced a highly versatile test function which could approximate all the observed solution profiles of this system. Using such a test function with the nonperturbative method, we could also describe the more complex solutions in the regimes of the Hopf bifurcation, the hysteresis loop as well as near the two saddle-nodes. The oscillatory solution near the Hopf bifurcation was analysed using a time-dependent version of the nonperturbative method, and we found that the obtained values of the time periods of the oscillations as well as the critical values of the Hopf bifurcation closely matched the numerical results.

We finally examined a two-component combustion system which modelled the temperature and concentration of a flame filament. Stirring such a system removes heat from the flame filaments and when the stirring rate is too large the flame is quenched. This quenching point corresponds to the bifurcation point of a saddle-node. Using the nonperturbative method, we examined the dependence of the system behaviour on the Damköhler number and the Lewis number. We found that the solution near the saddle-node could again be well approximated using bell-shaped test functions for low values of Le, and with a versatile tanh-based test function for large Le. This corresponds to the numerical observation that the solution profile near the critical Damköhler number quickly becomes plateau-like for large Le. To describe the solution

behaviour far from the saddle-node, we found an empirical formula for the widths of the solution.

We thus found that this nonperturbative method allows us to effectively describe the solution behaviour of chaotically stirred reaction-diffusion systems in terms of the system parameters alone. Using this method we describe the solution of an infinite-dimensional partial differential equation by a set of algebraic equations (in the case of steady-state solutions) or by a set of ordinary differential equations (in the case of oscillatory time-dependent solutions), constituting a dimensional reduction. We conclude that while the accuracy of results obtained with this method depends on our choice of test functions, the method nevertheless provides a simple and effective way of studying the behaviour of reaction-diffusion systems.

Appendix A

Description of numerical methods

In Chapter 2, we describe a 1-D filament model which can be used to study the behaviour of chaotically stirred reaction-advection-diffusion systems. This model is given by a set of nonlinear partial differential equations (2.3), which describe the temporal evolution of an initial condition $u(x, t = 0)$. As discussed in Sec. 2.2, these systems exhibit stationary solutions which arise due to the balance between advection and diffusion. The steady-state solutions are obtained by solving the corresponding set of steady-state ordinary differential (2.4) equations (for which $\partial/\partial t = 0$).

We now describe the methods used to numerically solve the equations. The full set of partial differential equations are solved using a semi-implicit Crank-Nicolson decomposition in which the nonlinear terms are treated using an Adams-Bashforth scheme [13]. This scheme is second-order in time and space. The set of ordinary differential equations are solved using a shooting method. To illustrate these methods we consider for simplicity a one-component model. We then outline how to apply the schemes for multi-component models.

A.1 Solving the partial differential equations

We consider the following one-component reaction-advection-diffusion system

$$\frac{\partial c}{\partial t} = D\,\frac{\partial^2 c}{\partial x^2} + x\,\frac{\partial c}{\partial x} + Da\,\mathcal{F}\left(c\right)\,, \tag{A.1}$$

where c may be the concentration of the component, D is its diffusion coefficient, Da is the Damköhler number and $\mathcal{F}\left(c\right)$ is the nonlinear reaction term.

We assume boundary conditions given by $c_x(\pm\infty) = 0$. We write (A.1) as

$$\frac{\partial c}{\partial t} = \mathcal{L}c + \mathcal{N}(c)\,, \tag{A.2}$$

where $\mathcal{L} = D\,\partial_{xx} + x\,\partial_x$ is a linear operator and $\mathcal{N}(c) = Da\,\mathcal{F}(c)$ comprises the nonlinear terms of the system. We may solve such a system using a semi-implicit Crank-Nicolson decomposition for the linear terms and an explicit second-order Adams-Bashforth scheme for the nonlinear terms [127]. This scheme is second-order in time, and its advantage is that it is an unconditionally stable scheme, which does not require a Courant-Friedrich-Levy condition on the size of the time step.

We consider a sufficiently large spatial domain $x \in [-L/2, L/2]$. We discretise the spatial domain L with a constant grid spacing Δx. The temporal discretisation is done using a constant time step Δt. The box therefore has $N = L/\Delta x$ grid points and the value of $c(x)$ at the j^{th} grid point and at the n^{th} time step will be represented by c_j^n. For this finite box, we will consider Neumann boundary conditions and shall set $\partial c/\partial x$ at $x = \pm L/2$ to zero.

We discretise (A.2) in time using the semi-implicit Crank-Nicolson decomposition and the Adams-Bashforth scheme as

$$\frac{c_j^{n+1} - c_j^n}{\Delta t} = \mathcal{L}\left(\frac{c_j^{n+1} - c_j^n}{2}\right) + \frac{1}{2}\left(3\mathcal{N}\left(c_j^n\right) - \mathcal{N}\left(c_j^{n-1}\right)\right)\,, \tag{A.3}$$

which we can write as an explicit equation for c^{n+1}

$$\left(I - \frac{\Delta t}{2}\mathcal{L}\right)c_j^{n+1} = \left(I + \frac{\Delta t}{2}\mathcal{L}\right)c_j^n + \frac{\Delta t}{2}\left(3\mathcal{N}\left(c_j^n\right) - \mathcal{N}\left(c_j^{n-1}\right)\right)\,. \tag{A.4}$$

We now discretise space and represent the spatial derivatives using second order finite differencing. We express the operator $\mathcal{L} = D\,\partial_{xx} + x\,\partial_x$ as a matrix which acts as

$$L_{ij}c_j = D\left(\frac{c_{j+1} - 2\,c_j + c_{j-1}}{\Delta x^2}\right) + x_j\left(\frac{c_{j+1} - c_{j-1}}{2\,\Delta x}\right)\,. \tag{A.5}$$

Since the scheme (A.4) requires c^0 and c^1, we employ a simple forward Euler step to estimate c^1,

$$c_j^1 = c_j^0 + \Delta t\left(L_{ij}c_j^0 + \mathcal{N}\left(c_j^0\right)\right)\,. \tag{A.6}$$

Although the forward Euler scheme is only first order in time, we find that the error made is absorbed by the more accurate stable Crank-Nicolson scheme.

This method can be easily extended to a multi-component system. Consider a two-component model of the form

$$\frac{\partial c}{\partial t} = D_1 \frac{\partial^2 c}{\partial x^2} + x \frac{\partial c}{\partial x} + \mathcal{N}_1 (c, v) \ , \tag{A.7}$$

$$\frac{\partial v}{\partial t} = D_2 \frac{\partial^2 v}{\partial x^2} + x \frac{\partial v}{\partial x} + \mathcal{N}_2 (c, v) \ , \tag{A.8}$$

where c and v are, for example, the concentration of the two components. The system has linear operators $\mathcal{L}_1 = D_1 \, \partial_{xx} + x \, \partial_x$ and $\mathcal{L}_2 = D_2 \, \partial_{xx} + x \, \partial_x$, while the nonlinear terms are given by

$$\mathcal{N}_i (c, v) = \frac{1}{2} \left(3 \mathcal{N}_i (c^n, v^n) - \mathcal{N}_i (c^{n-1}, v^{n-1}) \right) \ , \tag{A.9}$$

for $i = 1, 2$. Following the same procedure as before, we obtain the following explicit temporal discretisation for c^{n+1} and v^{n+1}

$$\left(I - \frac{\Delta t}{2} \mathcal{L}_1 \right) c^{n+1} = \left(I + \frac{\Delta t}{2} \mathcal{L}_1 \right) c^n + \frac{\Delta t}{2} \left(3 \mathcal{N}_1 (c^n, v^n) - \mathcal{N}_1 (c^{n-1}, c^{n-1}) \right) \ , \tag{A.10}$$

$$\left(I - \frac{\Delta t}{2} \mathcal{L}_2 \right) v^{n+1} = \left(I + \frac{\Delta t}{2} \mathcal{L}_2 \right) v^n + \frac{\Delta t}{2} \left(3 \mathcal{N}_2 (c^n, v^n) - \mathcal{N}_2 (c^{n-1}, v^{n-1}) \right) \ . \tag{A.11}$$

We invert the left hand side matrices to obtain explicit expressions for c^{n+1} and v^{n+1}. Again the required fields c^1 and v^1 are obtained using forward Euler steps from c^0 and v^0 respectively.

This scheme can be used to determine the stable steady-state solution by allowing a sufficiently long integration time. We check convergence to the steady-state solution by taking the l_1-norm of the error between c^{n+1} and c^n, which in the case of a one-component scheme is

$$E(n) = \sum_{j=1}^{N} \left| c_j^{n+1} - c_j^n \right| < \varepsilon \, . \tag{A.12}$$

For our simulations we used a value $\varepsilon = 10^{-12}$. Although this allows us to accurately obtain the stable steady-state solutions, to find the unstable stationary solutions we need to use a shooting method which we now describe.

A.2 Solving the ordinary differential equations

The stationary solutions are solutions of the steady-state equation

$$D\,\frac{\partial^2 c}{\partial x^2} + x\,\frac{\partial c}{\partial x} + Da\,\mathcal{F}\,(c) = 0\,, \tag{A.13}$$

where we again consider for simplicity a one-component system. We consider the spatial domain $x \in [0, L]$ and solve this second order ordinary differential equation using a shooting method which is described as follows.

At $x = 0$ we prescribe the functional value $c(0)$, which we treat as a parameter, and its derivative, which due to the inherent symmetry of the solution is zero. We then "shoot" from this boundary to the right boundary at $x = L$, where $c \approx 0$. At $x = L$ for a sufficiently large L the sought after solution behaviour will have the asymptotic behaviour at $x \to \infty$. We want to match the "shot" solution with these prescribed asymptotic boundary conditions. The desired solution linking the two boundaries is found by varying the amplitude $c(0)$ at the left boundary and the amplitude of the right boundary condition. Only for a unique set of boundary values does a solution exist.

The values of $c(x)$ and $c_x(x)$ at the boundary $x = L$ are found by considering the behaviour in the limit $x \to \infty$. The solution satisfies $c = 0$ in this limit. We thus linearise the system (A.13) around $c = 0$, and write

$$c = \kappa\,\delta c\,, \tag{A.14}$$

where κ is a small parameter. The linearised system is then

$$D\;(\delta c)_{xx} + L\;(\delta c)_x + Da\,\frac{\partial \mathcal{F}}{\partial c}\,(c = 0)\;\delta c = 0\,. \tag{A.15}$$

This can be written as a system of first order equations

$$\begin{pmatrix} (\delta c)_x \\ (\delta v)_x \end{pmatrix} = \begin{pmatrix} 0 & 1 \\ -\dfrac{Da}{D}\,\dfrac{\partial \mathcal{F}}{\partial c}\,(c = 0) & -\dfrac{L}{D} \end{pmatrix} \begin{pmatrix} \delta c \\ \delta v \end{pmatrix}. \tag{A.16}$$

The eigenvalues of this system $\lambda_\pm$ are given by

$$\lambda_\pm = -\frac{L}{2\,D} \pm \sqrt{\left(\frac{x}{2\,D}\right)^2 - \frac{Da}{D}\,\frac{\partial \mathcal{F}}{\partial c}\,(c = 0)}\,. \tag{A.17}$$

We note here that for $\partial \mathcal{F}\,(c = 0)/\partial c < 0$, $c = 0$ is a saddle with one positive and one negative eigenvalue. The eigenvalue $\lambda_- < 0$ and its corresponding

eigenvector determine the asymptotic behaviour at $x \to \infty$. We therefore require the solution of (A.13) to take the following values at $x = L$

$$c(L) = \kappa\, e^{\lambda_- L} \quad \text{and} \quad c_x(L) = \kappa\, \lambda_-\, e^{\lambda_- L}\,. \tag{A.18}$$

Hence the solution of (A.13) is found by varying $c(0)$ and κ such that the solution "shot" from the initial conditions at $x = 0$ matches up with the values of $c(x)$ and $c_x(x)$ at $x = L$ given by (A.18). This is tested numerically by varying these parameters until

$$c(L) - \kappa\, e^{\lambda_- L} < \vartheta \quad \text{and} \quad c_x(L) - \kappa\, \lambda_-\, e^{\lambda_-} < \vartheta\,, \tag{A.19}$$

for some specified value of theta. For our calculations, we used a value $\vartheta = 10^{-8}$.

The shooting method allows us to determine both the stable and unstable solutions. We find them using different choices of our initial guesses $c(0)$ and κ, which may differ substantially (as seen for example in Fig. 4.5 where the difference in the values of $c(0)$ for the stable and unstable branch increases as we move away from the saddle-node).

Appendix B

Derivation of the expressions for the free parameters of a Gaussian test function in an excitable system

B.1 Derivation of the amplitude and inverse pulse width

In Chapter 5, it was seen that the solution behaviour of an excitable system (5.1)-(5.2) near the saddle-node due to stirring $Da_c(\epsilon)$ could be approximated by a Gaussian test function (5.14). Such a function was used with the non-perturbative method to analyse the solution in this regime. It was noted that for a such a test function, one could derive explicit analytic results for the parameters f_0 (5.27) and w (5.29) which correspond to the amplitude and the inverse pulse width of the Gaussian test function respectively. Here we shall detail the steps involved in this derivation, and we shall also simplify these expressions in various limiting cases.

As described in Chapter 5, we restrict the solution space of the system to that of the test functions U and V. The conditions for minimising the error made by this restriction are (5.25) and (5.26), which we restate here as

$$\langle w^2\, U_{\eta\eta} + \eta\, U_\eta + Da\, U(1-U)(U-u_s-V) \mid U\rangle_\eta = 0\,, \tag{B.1}$$

$$\langle w^2\, U_{\eta\eta} + \eta\, U_\eta + Da\, U(1-U)(U-u_s-V) \mid \eta\, U_\eta\rangle_\eta = 0\,. \tag{B.2}$$

Here we can make a few simplifications for some of the integrals using partial integration. To describe the solution behaviour of a chaotically stirred excitable system, we only choose test functions U which are symmetric and

for which $U(-\infty) = U(\infty) = 0$. For such test functions, we find that

$$\langle \eta\, U_{\eta\eta}\, U_\eta \rangle = -\frac{1}{2}\langle U_\eta^2 \rangle\,, \qquad \langle \eta\, U_\eta\, U^n \rangle = -\frac{1}{n+1}\langle U^{n+1} \rangle\,. \tag{B.3}$$

for $n > 0$. We note that for the limiting value $\delta = 0$, the equation for the inhibitor (5.4) can be written as

$$\eta\, V_\eta = -Da\,\epsilon\,(U - a\,V)\,. \tag{B.4}$$

This can be used to simplify the integral

$$\begin{aligned}\langle \eta\, U^{n-1} U_\eta\, V \rangle &= -\frac{1}{n}\left(\langle \eta\, U^n\, V_\eta \rangle + \langle U^n\, V \rangle\right) \\ &= -\frac{1}{n}\langle U^n\, V \rangle + \frac{1}{n} Da\,\epsilon\left(\langle U^{n+1} \rangle - a\langle U^n\, V \rangle\right)\,.\end{aligned} \tag{B.5}$$

We can now combine the conditions (B.1)-(B.2) to give us the single condition for the test functions

$$\begin{aligned}\frac{9\,a + 8\,\alpha}{12\,a}\langle U^4 \rangle - \frac{5 + 4\,\alpha}{6}\langle U^3\, V \rangle - \frac{5\,a\,(1 + u_s) + 6\,\alpha}{6\,a}\langle U^3 \rangle \\ + (1 + \alpha)\,\langle U^2\, V \rangle + \left(u_s + \frac{1}{Da}\right)\langle U^2 \rangle = 0\,,\end{aligned} \tag{B.6}$$

where we have defined $\alpha = Da\,\epsilon\, a/2$.

The integrals of the type $\langle U^n\, V \rangle$ can be evaluated by considering the solution of $V(\eta)$ for the limiting value $\delta = 0$. When U is given by a Gaussian test function, i.e. $U(\eta) = f_0 \exp(-\eta^2)$, we find that V is given by (5.23). This expression is restated here as

$$V(\eta) = \frac{f_0\,\alpha}{a}\,\eta^{2\alpha}\,\Gamma(-\alpha, \eta^2)\,. \tag{B.7}$$

Writing the incomplete Gamma function in terms of an infinite sum [5] (eqn. (6.5.29)), we get the following expression

$$V(\eta) = \frac{f_0\,\alpha}{a}\,\eta^{2\alpha}\left(\Gamma\,(-\alpha) + \eta^{-2\alpha}\sum_{j=0}^{\infty}\frac{(-1)^j\,\eta^{2j}}{j!\,(\alpha - j)}\right)\,. \tag{B.8}$$

The integral $\langle U^n V \rangle$ can now be explicitly written as

$$\begin{aligned}\langle U^n\, V \rangle =& \frac{f_0\,\alpha}{a}\Gamma\,(-\alpha)\int_{-\infty}^{\infty}\eta^{2\alpha} U^n(\eta)\,d\eta \\ &+ \frac{f_0\,\alpha}{a}\int_{-\infty}^{\infty} U^n(\eta)\sum_{j=0}^{\infty}\frac{(-1)^j\,\eta^{2j}}{j!\,(\alpha - j)}\,d\eta\,.\end{aligned} \tag{B.9}$$

As U is a Gaussian test function, this simplifies to

$$\begin{aligned}\langle U^n\, V\rangle = \frac{f_0^{n+1}\,\alpha}{a}\Bigg(&\Gamma\left(-\alpha\right)\Gamma\left(\alpha+1/2\right)n^{-1/2-\alpha}\\ &+\sum_{j=0}^{\infty}\int_{-\infty}^{\infty}e^{-n\eta^2}\frac{(-1)^j\,\eta^{2j}}{j!\,(\alpha-j)}d\eta\Bigg)\,,\end{aligned} \tag{B.10}$$

where the order of integration and summation has been reversed for the second integral. The integral over η can be found explicitly, and the summation is found to yield

$$\sum_{j=0}^{\infty}\frac{(-1)^j\,n^{-1/2-j}\Gamma\left(j+1/2\right)}{j!\,(\alpha-j)} = \frac{1}{\alpha}\sqrt{\frac{\pi}{n}}\,{}_2F_1\left(\{1/2,-\alpha\}\,;\{1-\alpha\}\,;-\frac{1}{n}\right)\,. \tag{B.11}$$

Substituting this back into (B.10), we get

$$\begin{aligned}\langle U^n\, V\rangle =& f_0^{n+1}\Bigg[\frac{\alpha}{a}\Gamma\left(-\alpha\right)\Gamma\left(\alpha+\frac{1}{2}\right)n^{-\frac{1}{2}-\alpha}\\ &+\frac{1}{a}\sqrt{\frac{\pi}{n}}\,{}_2F_1\left(\left\{\frac{1}{2},-\alpha\right\}\,;\{1-\alpha\}\,;-\frac{1}{n}\right)\Bigg]\\ =:& f_0^{n+1}\,K\left(n\right)\,.\end{aligned} \tag{B.12}$$

Furthermore, we find that for the choice of a Gaussian test function the following integrals in (B.6) can be found explicitly

$$\langle U^n\rangle = \sqrt{\frac{\pi}{n}}f_0^n\,,\qquad \langle\eta^2 U_\eta^2\rangle = \frac{3}{4}\langle U^2\rangle\,. \tag{B.13}$$

for $n>0$. Substituting (B.12) and (B.13) into (B.6), we obtain a quadratic equation for the amplitude f_0 (5.27), which we write here as

$$\begin{aligned}&\Big(\frac{9\,a+8\alpha}{12\,a}\sqrt{\frac{\pi}{4}}-\frac{5+4\,\alpha}{6}K(3)\Big)f_0^2-\\ &\Big(\frac{5\,a\,(1+u_s)+6\,\alpha}{6\,a}\sqrt{\frac{\pi}{3}}+(1+\alpha)\,K(2)\Big)f_0+\left(u_s+\frac{1}{Da}\right)\sqrt{\frac{\pi}{2}}=0\,.\end{aligned} \tag{B.14}$$

We can then find the expression for the inverse width w (5.29) by substituting (B.12) and (B.13) into (B.1) and we restate this here as

$$\begin{aligned}w=\sqrt{Da}\Bigg[&f_0^2\left(\sqrt{\frac{2}{\pi}}K(3)-\frac{1}{\sqrt{2}}\right)-\\ &f_0\left(\sqrt{\frac{2}{\pi}}K(2)-(1-u_s)\sqrt{\frac{2}{3}}\right)-\left(u_s+\frac{1}{2\,Da}\right)\Bigg]^{1/2}\,.\end{aligned} \tag{B.15}$$

B.2 Limiting cases

B.2.1 The limit $a \to 0$

In the limit $a \to 0$, the inhibitor $v(x,t)$ will not decay in space. If U is taken to be a Gaussian test function (5.14), and we set $a = 0$ in the equation for the inhibitor in the slow stirring limit (B.4), we obtain the expression

$$V(\eta) = -\frac{f_0 Da\,\epsilon}{2}\mathrm{Ei}(-\eta^2)\,, \tag{B.16}$$

which is in terms of the exponential integral

$$\mathrm{Ei}(x) = \int_{-\infty}^{x} \frac{e^{\varsigma}}{\varsigma} d\varsigma\,. \tag{B.17}$$

In this limit, we find that the integrals $\langle U^n\, V\rangle$ can be solved explicitly to obtain a simplified expression for $K(n)$ (5.31), which we restate here as

$$K(n) = Da\,\epsilon\sqrt{\frac{\pi}{n}}\,\mathrm{arcsinh}\big(\sqrt{n}\big)\,. \tag{B.18}$$

B.2.2 The limit $\epsilon \to 0$

In the limiting case $\epsilon \to 0$, the chaotically stirred excitable system (5.1)-(5.2) behaves like the bistable system (which has been described in Chapter 4). This is due to the fact that in this limit the inhibitor is a constant. Setting $\epsilon = 0$ in (5.28) (and using $K(n) = 0$ for this limit), we obtain an expression

$$A\, f_0^2 + B\, f_0 + C = 0\,, \tag{B.19}$$

where

$$A = \frac{3}{4}\,,\quad B = -\frac{5\,(1+u_s)}{3\sqrt{3}}\,,\quad C = \frac{\sqrt{2}\,(Da\,u_s + 1)}{Da}\,. \tag{B.20}$$

This corresponds to the result obtained for the bistable system (4.20)-(4.21) [91, 26].

B.2.3 The limit $Da \to \infty$

As discussed in Section 2.2, the system will behave asymptotically like the rescaled unstirred system in the limit $Da \to \infty$. We expect that in this limit, we can reproduce the results (5.18)-(5.22) found in [47] for the unstirred system in a frame of reference that moves with speed $c_0 = \mu/\sqrt{Da}$.

To do this we first show that the inhibitor of the stirred system $v(\eta)$ is equal to that of the unstirred system $\tilde{v}(\eta)$ in the limit $Da \to \infty$. The equation for the inhibitor under the influence of stirring is

$$\eta\, v_\eta = -\theta(u - a\, v)\,, \tag{B.21}$$

where $\theta = \epsilon Da$, while the corresponding equation for the inhibitor in the unstirred system (5.8) can be rescaled to give

$$\tilde{v}_\eta = -\Theta(u - a\,\tilde{v})\,, \tag{B.22}$$

where $\Theta = \theta/(\mu\, w)$, and where we take $\eta = w\, x$ and $\mu = \sqrt{Da}\bar{w}$. This equation can be solved by variation of constants to give

$$\tilde{v}(\eta) = -\Theta\, e^{a\Theta\eta} \int_{-\infty}^{\eta} d\eta'\, e^{-a\Theta\eta'} u(\eta')\,. \tag{B.23}$$

The corresponding solution of the stirred system (B.21) is

$$v(\eta) = -\theta\, \eta^{a\theta} \int_{-\infty}^{\eta} d\eta'\, \eta'^{-a\theta} \frac{1}{\eta'} u(\eta')\,. \tag{B.24}$$

By using $\lim_{\theta\to\infty}(1+z/\theta)^\theta = \exp(z)$ we find that in the limit $\theta \to \infty$ equation (B.24) converges to

$$\begin{aligned} v(\eta) &= -\theta\, e^{a\theta\eta} \int_{-\infty}^{\eta} d\eta'\, e^{-a\theta\eta'} \frac{1}{\eta'} u(\eta') \\ &\to -\Theta\, e^{a\Theta\eta} \int_{-\infty}^{\eta} d\eta'\, e^{-a\Theta\eta'} u(\eta')\,, \end{aligned}$$

where for an activator $u(w\, x)$ located at $x = \mu$, we have used $u(w\, x)/(w\, x) \to u(w\, x)/(w\, \mu)$ for $\mu \to \infty$. We therefore find that the solution for the inhibitor of the stirred system (B.21) will converge to the solution for the inhibitor of the unstirred equation (B.22) for $Da \to \infty$, i.e. $v = \tilde{v}$ in this limit.

We now rewrite the algebraic equations (B.6) for the stirred system (5.3)-(5.4) as

$$A\, f_0^2 + B\, f_0 + C = 0\,, \tag{B.25}$$

with

$$A = \frac{3}{4}\langle \tilde{U}^4 \rangle - \frac{5}{6}\langle \tilde{U}^3\, V \rangle + \frac{\theta}{3}(\langle \tilde{U}^4 \rangle - a\langle \tilde{U}^3\, V \rangle)\,, \tag{B.26}$$

$$B = -\frac{5}{6}\,(1 + u_s)\,\langle \tilde{U}^3 \rangle + \langle \tilde{U}^2\, V \rangle - \frac{\theta}{2}(\langle \tilde{U}^3 \rangle - a\langle \tilde{U}^2\, V \rangle)\,, \tag{B.27}$$

$$C = \left(u_s + \frac{1}{Da}\right)\langle \tilde{U}^2 \rangle\,, \tag{B.28}$$

where we take $U = f_0\tilde{U}$. From (B.21), we find

$$A = \frac{3}{4}\langle\tilde{U}^4\rangle - \frac{5}{6}\langle\tilde{U}^3\,V\rangle - \frac{1}{3}\langle\eta\,V_\eta\,\tilde{U}^3\rangle\,, \tag{B.29}$$

$$B = -\frac{5}{6}\,(1+u_s)\,\langle\tilde{U}^3\rangle + \langle\tilde{U}^2\,V\rangle + \frac{1}{2}\langle\eta\,V_\eta\,\tilde{U}^2\rangle\,, \tag{B.30}$$

$$C = \left(u_s + \frac{1}{Da}\right)\langle\tilde{U}^2\rangle\,. \tag{B.31}$$

As $v = \tilde{v}$ in the limit $Da \to \infty$, this gives us

$$V_\eta = -\Theta(U - a\,V)\,. \tag{B.32}$$

We can substitute this into (B.29)-(B.31) and use the evenness of U to obtain the expressions for A, B and C in (5.19) for the unstirred equations (5.7)-(5.8). We therefore find that the expressions for the unstirred case can be explicitly obtained from those of the stirred case in the limit $Da \to \infty$.

Bibliography

[1] M. Abel, A. Celani, D. Vergni, and A. Vulpiani. Front propagation in laminar flows. *Physical Review E*, 64(4):046307, 2001.

[2] E. R. Abraham. The generation of plankton patchiness by turbulent stirring. *Nature*, 391(6667):577, 1998.

[3] E. R. Abraham and M. M. Bowen. Chaotic stirring by a mesoscale surface-ocean flow. *Chaos*, 12(2):373, 2002.

[4] E. R. Abraham, C. S. Law, P. W. Boyd, S. J. Lavender, M. T. Maldonado, and A. R. Bowie. Importance of stirring in the development of an iron-fertilized phytoplankton bloom. *Nature*, 407(6805):727, 2000.

[5] M. Abramowitz and I. A. Stegun. *Handbook of Mathematical Functions with Formulas, Graphs, and Mathematical Tables*. Dover, New York, ninth dover printing, tenth gpo printing edition, 1964.

[6] A. Adrover, M. Giona, F. J. Muzzio, S. Cerbelli, and M. M. Alvarez. Analytic expression for the short-time rate of growth of the intermaterial contact perimeter in two-dimensional chaotic flows and Hamiltonian systems. *Physical Review E*, 58(1):447, 1998.

[7] F. Ali and M. Menzinger. Stirring effects and phase-dependent inhomogeneity in chemical oscillations: The Belousov-Zhabotinsky reaction in a CSTR. *Journal of Physical Chemistry A*, 101(12):2304, 1997.

[8] M. A. Allen, J. Brindley, J. H. Merkin, and M. J. Pilling. Autocatalysis in a shear flow. *Physical Review E*, 54(2):2140, 1996.

[9] M. M. Alvarez, F. J. Muzzio, S. Cerbelli, A. Adrover, and M. Giona. Self-similar spatiotemporal structure of intermaterial boundaries in chaotic flows. *Physical Review Letters*, 81(16):3395, 1998.

[10] H. Aref. Stirring by chaotic advection. *Journal of Fluid Mechanics*, 143:1, 1984.

[11] S. Balasuriya, G. Gottwald, J. Hornibrook, and S. Lafortune. High Lewis number combustion wavefronts: A perturbative Melnikov analysis. *Siam Journal on Applied Mathematics*, 67(2):464, 2006.

[12] D. Barkley. A model for fast computer simulation of waves in excitable media. *Physica D*, 49(1-2):61, 1991.

[13] C. M. Bender and S. A. Orszag. *Advanced mathematical methods for scientists and engineers. I. Asymptotic methods and perturbation theory*. Springer-Verlag, New York, 1999. Reprint of the 1978 original.

[14] U. R. Bidkar and D. V. Khakhar. Collision rates in chaotic flows: Dilute suspensions. *Physical Review A*, 42(10):5964, 1990.

[15] P. W. Boyd, A. J. Watson, C. S. Law, E. R. Abraham, T. Trull, R. Murdoch, D. C. E. Bakker, A. R. Bowie, K. O. Buesseler, H. Chang, M. Charette, P. Croot, K. Downing, R. Frew, M. Gall, M. Hadfield, J. Hall, M. Harvey, G. Jameson, J. LaRoche, M. Liddicoat, R. Ling, M. T. Maldonado, R. M. McKay, S. Nodder, S. Pickmere, R. Pridmore, S. Rintoul, K. Safi, P. Sutton, R. Strzepek, K. Tanneberger, S. Turner, A. Waite, and J. Zeldis. A mesoscale phytoplankton bloom in the polar southern ocean stimulated by iron fertilization. *Nature*, 407(6805):695, 2000.

[16] J. H. E. Cartwright, E. Hernández-García, and O. Piro. Burridge-Knopoff models as elastic excitable media. *Physical Review Letters*, 79(3):527, 1997.

[17] J. Chaiken, R. Chevray, M. Tabor, and Q. M. Tan. Experimental study of Lagrangian turbulence in a Stokes flow. *Proceedings of the Royal Society of London Series A*, 408(1834):165, 1986.

[18] R. Chella and J. M. Ottino. Modeling of rapidly-mixed fast-crosslinking exothermic polymerizations. 1. Adiabatic temperature rise. *AIChE Journal*, 29(3):373, 1983.

[19] R. Chella and J. M. Ottino. Conversion and selectivity modifications due to mixing in unpremixed reactors. *Chemical Engineering Science*, 39(3):551, 1984.

[20] W. L. Chien, H. Rising, and J. M. Ottino. Laminar mixing and chaotic mixing in several cavity flows. *Journal of Fluid Mechanics*, 170(1):355, 1986.

[21] M. J. Clifford, S. M. Cox, and E. P. L. Roberts. Lamellar modelling of reaction, diffusion and mixing in a two-dimensional flow. *Chemical Engineering Journal*, 71(1):49, 1998.

[22] P. Constantin, A. Kiselev, A. Oberman, and L. Ryzhik. Bulk burning rate in passive-reactive diffusion. *Archive for Rational Mechanics and Analysis*, 154(1):53, 2000.

[23] P. Constantin, A. Kiselev, and L. Ryzhik. Quenching of flames by fluid advection. *Communications on Pure and Applied Mathematics*, 54(11):1320, 2001.

[24] S. Cortassa, H. Sun, J. P. Kernevez, and D. Thomas. Pattern formation in an immobilized bienzyme system: A morphogenetic model. *Biochemical Journal*, 269(1):115, 1990.

[25] S. M. Cox. Chaotic mixing of a competitive-consecutive reaction. *Physica D*, 199(3-4):369, 2004.

[26] S. M. Cox and G. A. Gottwald. A bistable reaction-diffusion system in a stretching flow. *Physica D*, 216(2):307, 2006.

[27] G. Damköhler. Influence of currents, diffusion and heat transfer on the efficiency of the reaction furnace. *Zeitschrift für Elektrochemie und Angewandte Physikalische Chemie*, 42:846, 1936.

[28] J. M. Davidenko, A. V. Pertsov, R. Salomonsz, W. Baxter, and J. Jalife. Stationary and drifting spiral waves of excitation in isolated cardiac muscle. *Nature*, 355(6358):349, 1992.

[29] S. Edouard, B. Legras, F. Lefèvre, and R. Eymard. The effect of small-scale inhomogeneities on ozone depletion in the arctic. *Nature*, 384(6608):444, 1996.

[30] S. Edouard, B. Legras, and V. Zeitlin. The effect of dynamical mixing in a simple model of the ozone hole. *Journal of Geophysical Research D*, 101(D11):16771, 1996.

[31] I. R. Epstein. The consequences of imperfect mixing in autocatalytic chemical and biological systems. *Nature*, 374(6520):321, 1995.

[32] E. A. Ermakova, V. I. Krinsky, A. V. Panfilov, and A. M. Pertsov. Interaction between spiral and flat periodic autowaves in an active medium. *Biofizika*, 31(2):318, 1986.

[33] S. D. Fields and J. M. Ottino. Effect of segregation on the course of unpremixed polymerizations. *AIChE Journal*, 33(6):959, 1987.

[34] S. D. Fields and J. M. Ottino. Effect of stretching path on the course of polymerizations: Applications to idealized unpremixed reactors. *Chemical Engineering Science*, 42(3):467, 1987.

[35] S. D. Fields and J. M. Ottino. Effect of striation thickness distribution on the course of an unpremixed polymerization. *Chemical Engineering Science*, 42(3):459, 1987.

[36] D. A. Fisher. A model for fast reactions in turbulently mixed liquids. Master's thesis, University of Minnesota, Minneapolis, Minnesota, 1968.

[37] D. A. Fisher. *Development and application of a model for fast reactions in turbulently mixed liquids*. PhD thesis, University of Minnesota, Minneapolis, Minnesota, 1974.

[38] R. A. Fisher. The wave of advance of advantageous genes. *Annals of Eugenics*, 7:353, 1937.

[39] R. FitzHugh. Impulses and physiological states in theoretical models of nerve membrane. *Biophysical Journal*, 1(6):445, 1961.

[40] J. G. Franjione and J. M. Ottino. Feasibility of numerical tracking of material lines and surfaces in chaotic flows. *Physics of Fluids*, 30(12):3641, 1987.

[41] V. C. Garçon, A. Oschlies, S. C. Doney, D. McGillicuddy, and J. Waniek. The role of mesoscale variability on plankton dynamics in the north atlantic. *Deep-Sea Research II*, 48(10):2199, 2001.

[42] C. H. Gibson and W. H. Thomas. Effects of turbulence intermittency on growth inhibition of a red tide dinoflagellate, Gonyaulax polyedra Stein. *Journal of Geophysical Research C*, 100(C12):24841, 1995.

[43] M. Giudici, C. Green, G. Giacomelli, U. Nespolo, and J. R. Tredicce. Andronov bifurcation and excitability in semiconductor lasers with optical feedback. *Physical Review E*, 55(6):6414, 1997.

[44] M. Gorman, M. El-Hamdi, and K. A. Robbins. Chaotic dynamics near the extinction limit of a premixed flame on a porous plug burner. *Combustion Science and Technology*, 98(1-3):47, 1994.

[45] M. Gorman, M. El-Hamdi, and K. A. Robbins. Experimental observation of ordered states of cellular flames. *Combustion Science and Technology*, 98(1-3):37, 1994.

[46] G. A. Gottwald. Bifurcation analysis of a normal form for excitable media: Are stable dynamical alternans on a ring possible? *Chaos*, 18(1):013129, 2008.

[47] G. A. Gottwald and L. Kramer. On propagation failure in one- and two-dimensional excitable media. *Chaos*, 14(3):855, 2004.

[48] G. A. Gottwald and L. Kramer. A normal form for excitable media. *Chaos*, 16(1):013122, 2006.

[49] G. A. Gottwald, A. Pumir, and V. Krinsky. Spiral wave drift induced by stimulating wave trains. *Chaos*, 11(3):487, 2001.

[50] P. H. Haynes. Transport, stirring and mixing in the atmosphere. In H. Chaté and E. Villermaux, editors, *Proceedings of the NATO Advanced Study Institute on Mixing: Chaos and Turbulence*, pages 229–272, Cargese, Corse, France, 1996. Kluwer Academic Publishers, Dordrecht.

[51] E. Hernández-García and C. Lopéz. Sustained plankton blooms under open chaotic flows. *Ecological Complexity*, 1(3):253, 2004.

[52] E. Hernández-García, C. Lopéz, and Z. Neufeld. Small-scale structure of nonlinearly interacting species advected by chaotic flows. *Chaos*, 12(2):470, 2002.

[53] E. Hernández-García, C. Lopéz, and Z. Neufeld. Filament bifurcations in a one-dimensional model of reacting excitable fluid flow. *Physica A*, 327(1-2):59, 2003.

[54] E. Hernández-García, C. López, and Z. Neufeld. Spatial patterns in chemically and biologically reacting flows. In G. Bofetta, G. Lacorata, G. Visconti, and A. Vulpiani, editors, *Chaos in Geophysical Flows*, pages 35–61. Otto Editore, Torino, Italy, 2003.

[55] A. L. Hodgkin and A. F. Huxley. A quantitative description of membrane current and its application to conduction and excitation in nerve. *Journal of Physiology*, 117(4):500, 1952.

[56] S. Jakubith, H. H. Rotermund, W. Engel, A. von Oertzen, and G. Ertl. Spatiotemporal concentration patterns in a surface-reaction: Propagating and standing waves, rotating spirals, and turbulence. *Physical Review Letters*, 65(24):3013, 1990.

[57] S. C. Jana, G. Metcalfe, and J. M. Ottino. Experimental and computational studies of mixing in complex stokes flows: The vortex mixing flow and multicellular cavity flows. *Journal of Fluid Mechanics*, 269(1):199, 1994.

[58] R. Kapral and K. Showalter, editors. *Chemical Waves and Patterns*. Kluwer Academic, Dordrecht, 1993.

[59] G. Károlyi, I. Scheuring, and T. Czárán. Metabolic network dynamics in open chaotic flow. *Chaos*, 12(2):460–469, 2002.

[60] J. Keener and J. Sneyd. *Mathematical Physiology*. Springer-Verlag, New York, 1998.

[61] D. V. Khakhar, H. Rising, and J. M. Ottino. Analysis of chaotic mixing in 2 model systems. *Journal of Fluid Mechanics*, 172(1):419, 1986.

[62] A. Kiselev and L. Ryzhik. Enhancement of the travelling front speeds in reaction-diffusion equations with advection. *Annales de l'institut Henri Poincaré- Analyse non linéaire*, 18(3):309, 2001.

[63] I. Z. Kiss, J. H. Merkin, and Z. Neufeld. Combustion initiation and extinction in a 2D chaotic flow. *Physica D*, 183(3-4):175, 2003.

[64] I. Z. Kiss, J. H. Merkin, S. K. Scott, P. L. Simon, S. Kalliadasis, and Z. Neufeld. The structure of flame filaments in chaotic flows. *Physica D*, 176(1-2):67, 2003.

[65] A. Kolmogorov, I. Petrovsky, and N. Piscounoff. Étude de l'équation de la diffusion avec croissance de la quantité de matière et son application à un problème biologique. *Bulletin de l'Université d'Etat à Moscou, Série Internationale*, 1:1, 1937.

[66] P. Kolodziej, C. W. Macosko, and W. E. Ranz. The influence of impingement mixing on striation thickness distribution and properties in fast polyurethane polymerization. *Polymer Engineering and Science*, 22(6):388, 1982.

[67] D. K. Kondepudi, R. J. Kaufman, and N. Singh. Chiral symmetry breaking in sodium chlorate crystallization. *Science*, 250(4983):975, 1990.

[68] D. K. Kondepudi and C. Sabanayagam. Secondary nucleation that leads to chiral symmetry breaking in stirred crystallization. *Chemical Physics Letters*, 217(4):364, 1994.

[69] V. I. Krinsky and K. I. Agladze. Interaction of rotating waves in an active chemical medium. *Physica D*, 8(1-2):50, 1983.

[70] H. S. Kwon. A description of mixing of fluids based on intermaterial area per unit volume. Master's thesis, University of Minnesota, Minneapolis, Minnesota, 1976.

[71] D. J. Lamberto, F. J. Muzzio, P. D. Swanson, and A. L. Tonkovich. Using time-dependent RPM to enhance mixing in stirred vessels. *Chemical Engineering Science*, 51(5):733, 1996.

[72] L. D. Landau and E. M. Lifshits. *Fluid Mechanics*. Elsevier, Butterworth-Heinemann, Oxford, UK, 2000.

[73] J. Lechleiter, S. Girard, E. Peralta, and D. Clapham. Spiral calcium wave propagation and annihilation in Xenopus laevis Ooctyes. *Science*, 252(5002):123, 1991.

[74] L. J. Lee, J. M. Ottino, W. E. Ranz, and C. W. Macosko. Impingement mixing in reaction injection molding. *Polymer Engineering and Science*, 20(13):868, 1980.

[75] C. W. Leong. *Chaotic Mixing of Viscous Fluids in Time-Periodic Cavity Flows*. PhD thesis, University of Massachusetts, 1990.

[76] C. W. Leong and J. M. Ottino. Experiments on mixing due to chaotic advection in a cavity. *Journal of Fluid Mechanics*, 209:463, 1989.

[77] O. Levenspiel. *Chemical Reaction Engineering*. Wiley, New York, 2nd edition, 1972.

[78] M. Liu, F. J. Muzzio, and R. L. Peskin. Effects of manifolds and corner singularities on stretching in chaotic cavity flows. *Chaos Solitons & Fractals*, 4(12):2145, 1994.

[79] M. Liu, F. J. Muzzio, and R. L. Peskin. Quantification of mixing in aperiodic chaotic flows. *Chaos Solitons & Fractals*, 4(6):869, 1994.

[80] M. Liu, R. L. Peskin, F. J. Muzzio, and C. W. Leong. Structure of the stretching field in chaotic cavity flows. *AIChE Journal*, 40(8):1273, 1994.

[81] C. López, Z. Neufeld, E. Hernández-García, and P. H. Haynes. Chaotic advection of reacting substances: Plankton dynamics on a meandering jet. *Physics and Chemistry of the Earth Part B*, 26(4):313, 2001.

[82] B. F. Madore and W. L. Freedman. Computer simulations of the Belousov-Zhabotinsky reaction. *Science*, 222(4624):615, 1983.

[83] A. P. Martin. On filament width in oceanic plankton distributions. *Journal of Plankton Research*, 22(3):597, 2000.

[84] A. P. Martin. Phytoplankton patchiness: the role of lateral stirring and mixing. *Progress in Oceanography*, 57(2):125, 2003.

[85] A. P. Martin, K. J. Richards, A. Bracco, and A. Provenzale. Patchy productivity in the open ocean. *Global Biogeochemical Cycles*, 16(2):1025, 2002.

[86] A. P. Martin, K. J. Richards, and M. J. R. Fasham. Phytoplankton production and community structure in an unstable frontal region. *Journal of Marine Systems*, 28(1-2):65, 2001.

[87] H. P. McKean. Nagumo's equation. *Advances in Mathematics*, 4(3):209, 1970.

[88] P. McLeod, A. P. Martin, and K. J. Richards. Minimum length scale for growth-limited oceanic plankton distributions. *Ecological Modelling*, 158(1-2):111, 2002.

[89] A. B. Medvinsky, A. V. Panfilov, and A. M. Pertsov. Autowave process characterization in heart tissue. In V. I. Krinsky, editor, *Self Organization, Autowaves and Structures Far From Equilibrium*, page 195199. Springer-Verlag, Berlin, 1984.

[90] S. N. Menon and G. A. Gottwald. Bifurcations in a chaotically stirred excitable system. submitted.

[91] S. N. Menon and G. A. Gottwald. Bifurcations in reaction-diffusion systems in chaotic flows. *Physical Review E*, 71(6):066201, 2005.

[92] S. N. Menon and G. A. Gottwald. Bifurcations of flame filaments in chaotically mixed combustion reactions. *Physical Review E*, 75(1):016209, 2007.

[93] M. Menzinger and A. K. Dutt. The myth of the well-stirred CSTR in chemical instability experiments: The chlorite/iodide reaction. *Journal of Physical Chemistry*, 94(11):4510, 1990.

[94] M. Menzinger and P. Jankowski. Heterogeneities and stirring effects in the Belusov-Zhabotinsky reaction. *Journal of Physical Chemistry*, 90(7):1217, 1986.

[95] E. Meron. Pattern formation in excitable media. *Physics Reports*, 218(1):1, 1992.

[96] G. Metcalfe and J. M. Ottino. Autocatalytic processes in mixing flows. *Physical Review Letters*, 72(18):2875, 1994.

[97] A. S. Mikhailov. *Foundations of Synergetics I: Distributed Active Systems*. Springer-Verlag, Berlin, 2nd edition, 1994.

[98] J. D. Murray. *Mathematical Biology*. Springer-Verlag, New York, 2nd edition, 1993.

[99] F. J. Muzzio and M. Liu. Chemical reactions in chaotic flows. *Chemical Engineering Journal*, 64(1):117, 1996.

[100] F. J. Muzzio, C. Meneveau, P. D. Swanson, and J. M. Ottino. Scaling and multifractal properties of mixing in chaotic flows. *Physics of Fluids A*, 4(7):1439, 1992.

[101] F. J. Muzzio and J. M. Ottino. Coagulation in chaotic flows. *Physical Review A*, 38(5):2516, 1988.

[102] F. J. Muzzio and J. M. Ottino. Dynamics of a lamellar system with diffusion and reaction: Scaling analysis and global kinetics. *Physical Review A*, 40(12):7182, 1989.

[103] F. J. Muzzio and J. M. Ottino. Evolution of a lamellar system with diffusion and reaction: A scaling approach. *Physical Review Letters*, 63(1):47, 1989.

[104] F. J. Muzzio and J. M. Ottino. Diffusion and reaction in a lamellar system: Self-similarity with finite rates of reaction. *Physical Review A*, 42(10):5873, 1990.

[105] F. J. Muzzio, E. L. Paul, and H. Freeman, editors. *Handbook of Industrial Pollution Prevention*. McGraw-Hill, New York, 1994.

[106] F. J. Muzzio, P. D. Swanson, and J. M. Ottino. The statistics of stretching and stirring in chaotic flows. *Physics of Fluids A*, 3(5):822, 1991.

[107] F. J. Muzzio, P. D. Swanson, and J. M. Ottino. Mixing distributions produced by multiplicative stretching in chaotic flows. *International Journal of Bifurcations and Chaos*, 2(1):37, 1992.

[108] J. Nagumo, S. Arimoto, and S. Yoshizawa. Active pulse transmission line simulating nerve axon. *Proceedings of the Institute of Radio Engineers*, 50(10):2061, 1962.

[109] I. Nagypál and I. R. Epstein. Fluctuations and stirring rate effects in the chlorite-thiosulfate reaction. *Journal of Physical Chemistry*, 90(23):6285, 1986.

[110] E. B. Nauman. Mixing in polymer reactions. *Journal of Macromolecular Science-Reviews in Macromolecular Chemistry and Physics*, C 10(1):75, 1974.

[111] Z. Neufeld. Excitable media in a chaotic flow. *Physical Review Letters*, 87(10):108301, 2001.

[112] Z. Neufeld, P. H. Haynes, V. C. Garçon, and J. Sudre. Ocean fertilization experiments may initiate a large scale phytoplankton bloom. *Geophysical Research Letters*, 29(11):1534, 2002.

[113] Z. Neufeld, P. H. Haynes, and T. Tél. Chaotic mixing induced transitions in reaction-diffusion systems. *Chaos*, 12(2):426, 2002.

[114] Z. Neufeld, I. Z. Kiss, C. S. Zhou, and J. Kürths. Synchronization and oscillator death in oscillatory media with stirring. *Physical Review Letters*, 91(8), 2003.

[115] Z. Neufeld, C. Lopéz, E. Hernández-García, and O. Piro. Excitable media in open and closed chaotic flows. *Physical Review E*, 66(6):066208, 2002.

[116] J. M. Ottino. Lamellar mixing models for structured chemical reactions and their relationship to statistical models, macro- and micromixing and the problem of averages. *Chemical Engineering Science*, 35(6):1377, 1980.

[117] J. M. Ottino. Description of mixing with diffusion and reaction in terms of the concept of material surfaces. *Journal of Fluid Mechanics*, 114(JAN):83, 1982.

[118] J. M. Ottino. *The Kinematics of Mixing: Stretching, Chaos and Transport*. Cambridge University Press, Cambridge, 1989.

[119] J. M. Ottino. Mixing and chemical reactions: A tutorial. *Chemical Engineering Science*, 49(24A):4005, 1994.

[120] J. M. Ottino, C. W. Leong, H. Rising, and P. D. Swanson. Morphological structures produced by mixing in chaotic flows. *Nature*, 333(6172):419, 1988.

[121] J. M. Ottino, F. J. Muzzio, M. Tjahjadi, J. G. Franjione, S. C. Jana, and H. A. Kusch. Chaos, symmetry, and self-similarity: Exploiting order and disorder in mixing processes. *Science*, 257(5071):754, 1992.

[122] J. M. Ottino, W. E. Ranz, and C. W. Macosko. Lamellar model for analysis of liquid-liquid mixing. *Chemical Engineering Science*, 34(6):877, 1979.

[123] J. M. Ottino, A. Souvaliotis, and G. Metcalfe. Chaotic mixing processes: New problems and computational issues. *Chaos, Solitons & Fractals*, 6:425, 1995.

[124] O. Paireau and P. Tabeling. Enhancement of the reactivity by chaotic mixing. *Physical Review E*, 56(2):2287, 1997.

[125] N. Peters. *Turbulent Combustion*. Cambridge University Press, Cambridge, 2000.

[126] T. Poinsot and D. Veynante. *Theoretical and Numerical Combustion*. Edwards, New York, 2001.

[127] W. Press, S. Teukolsky, W. Vetterling, and B. Flannery. *Numerical Recipes in C*. Cambridge University Press, Cambridge, 2nd edition, 1992.

[128] W. E. Ranz. Applications of a stretch model to mixing, diffusion and reaction in laminar and turbulent flows. *AIChE Journal*, 25(1):41, 1979.

[129] R. Reigada, F. Sagues, I. M. Sokolov, J. M. Sancho, and A. Blumen. Kinetics of the $A + B \rightarrow 0$ reaction under steady and turbulent flows. *Journal of Chemical Physics*, 105(24):10925, 1996.

[130] R. Reigada, F. Sagues, I. M. Sokolov, J. M. Sancho, and A. Blumen. Spatial correlations and cross sections of clusters in the $A + B \rightarrow 0$ reaction. *Physical Review E*, 53(4):3167, 1996.

[131] R. Reigada, F. Sagues, I. M. Sokolov, J. M. Sancho, and A. Blumen. Fluctuation-dominated kinetics under stirring. *Physical Review Letters*, 78(4):741, 1997.

[132] R. Reigada, F. Sagues, I. M. Sokolov, J. M. Sancho, and A. Blumen. Spatial organization in the $A + B \rightarrow 0$ reaction under confined-scale mixing. *Journal of Chemical Physics*, 107(3):843, 1997.

[133] P. D. Ronney. Some open issues in premixed turbulent combustion. In J. Buckmaster and T. Takeno, editors, *Modeling in Combustion Science*, Lecture Notes in Physics, pages 3–22. Springer-Verlag, New York, 1994.

[134] D. Rothstein, E. Henry, and J. P. Gollub. Persistent patterns in transient chaotic fluid mixing. *Nature*, 401(6755):770, 1999.

[135] A. B. Rovinsky and M. Menzinger. Chemical instability induced by a differential flow. *Physical Review Letters*, 69(8):1193, 1992.

[136] V. S. Santoro, A. Liñán, and A. Gomez. Propagation of edge flames in counterflow mixing layers: Experiments and theory. *Proceedings of the Combustion Institute*, 28(2):2039, 2000.

[137] D. R. Sawyers, M. Sen, and H. C. Chang. Effect of chaotic interfacial stretching on bimolecular chemical reaction in helical-coil reactors. *Chemical Engineering Journal*, 64(1):129, 1996.

[138] I. Scheuring, G. Károlyi, Á. Péntek, T. Tél, and Z. Toroczkai. A model for resolving the plankton paradox: Coexistence in open flows. *Freshwater Biology*, 45(2):123, 2000.

[139] I. Scheuring, G. Károlyi, Z. Toroczkai, T. Tél, and Á. Péntek. Competing populations in flows with chaotic mixing. *Theoretical Population Biology*, 63(2):77, 2003.

[140] J. Schmalzl, G. A. Houseman, and U. Hansen. Mixing in vigorous, time-dependent three-dimensional convection and application to earth's mantle. *Journal of Geophysical Research B*, 101(10):21847, 1996.

[141] L. S. Schulman and P. E. Seiden. Percolation and galaxies. *Science*, 233(4762):425, 1986.

[142] A. Scott. *Nonlinear Science: Emergence and Dynamics of Coherent Structures*. Oxford University Press, Oxford, 1999.

[143] S. K. Scott. *Chemical Chaos*. Oxford University Press, New York, 1991.

[144] F. Siegert and C. J. Weijer. Analysis of optical density wave propagation and cell movement in the cellular slime mould Dictyostelium discoideum. *Physica D*, 49(1-2):224, 1991.

[145] I. M. Sokolov and A. Blumen. Mixing effects in the $A+B \rightarrow 0$ reaction-diffusion scheme. *Physical Review Letters*, 66(14):1942, 1991.

[146] I. M. Sokolov and A. Blumen. Reactions in systems with mixing. *Journal of Physics A*, 24(15):3687, 1991.

[147] S. Solomon. Stratospheric ozone depletion: A review of concepts and history. *Reviews of Geophysics*, 37(3):275, 1999.

[148] T. H. Solomon and J. P. Gollub. Chaotic particle transport in time-dependent Rayleigh-Bénard convection. *Physical Review A*, 38(12):6280, 1988.

[149] J. C. Sommerer, H. C. Ku, and H. E. Gilreath. Experimental evidence for chaotic scattering in a fluid wake. *Physical Review Letters*, 77(25):5055, 1996.

[150] J. C. Sommerer and E. Ott. Particles floating on a moving fluid: A dynamically comprehensible physical fractal. *Science*, 259(5093):335, 1993.

[151] S. A. Spall and K. J. Richards. A numerical model of mesoscale frontal instabilities and plankton dynamics. I. Model formulation and initial experiments. *Deep-Sea Research I*, 47(7):1261, 2000.

[152] P. D. Swanson and J. M. Ottino. A comparative computational and experimental study of chaotic mixing of viscous fluids. *Journal of Fluid Mechanics*, 213(1):227, 1990.

[153] D. G. H. Tan, P. H. Haynes, A. R. MacKenzie, and J. A. Pyle. Effects of fluid-dynamical stirring and mixing on the deactivation of stratospheric chlorine. *Journal of Geophysical Research D*, 103(1):1585, 1998.

[154] X. Z. Tang and A. H. Boozer. Design criteria of a chemical reactor based on a chaotic flow. *Chaos*, 9(1):183, 1999.

[155] T. Tél, A. de Moura, C. Grebogi, and G. Károlyi. Chemical and biological activity in open flows: A dynamical system approach. *Physics Reports*, 413(2-3):91, 2005.

[156] T. Tél, T. Nishikawa, A. E. Motter, C. Grebogi, and Z. Toroczkai. Universality in active chaos. *Chaos*, 14(1):72, 2004.

[157] J. L. Thiffeault. Advection-diffusion in lagrangian coordinates. *Physics Letters A*, 309(5-6):415, 2003.

[158] Z. Toroczkai, G. Károlyi, Á. Péntek, T. Tél, and C. Grebogi. Advection of active particles in open chaotic flows. *Physical Review Letters*, 80(3):500, 1998.

[159] Z. Toroczkai and T. Tél, editors. *Focus Issue: Active Chaotic Flow, special issue of* Chaos *12*, 2002.

[160] J. E. Truscott and J. Brindley. Equilibria, stability and excitability in a general class of plankton population models. *Philosophical Transactions of the Royal Society of London Series A*, 347(1685):703, 1994.

[161] J. E. Truscott and J. Brindley. Ocean plankton populations as excitable media. *Bulletin of Mathematical Biology*, 56(5):981, 1994.

[162] E. E. Underwood. *Quantitative Stereology*. Addison-Wesley, Reading, Massachusetts, 1970.

[163] W. van Saarloos. Front propagation into unstable states. *Physics Reports*, 386(2-6):29, 2003.

[164] M. Vinson. Interactions of spiral waves in inhomogeneous excitable media. *Physica D*, 116(3-4):313, 1998.

[165] R. O. Weber, G. N. Mercer, H. S. Sidhu, and B. F. Gray. Combustion waves for gases ($Le = 1$) and solids ($Le \to \infty$). *Proceedings of the Royal Society of London Series A*, 453(1960):1105, 1997.

[166] S. Wiggins. *Chaotic Transport in Dynamical Systems*. Springer-Verlag, New York, 1992.

[167] F. A. Williams. *Combustion Theory*. Benjamin-Cummings, Menlo Park, CA, 1985.

[168] A. Wonhas and J. C. Vassilicos. Diffusivity dependence of ozone depletion over the midnorthern latitudes. *Physical Review E*, 65(5):051111, 2002.

[169] P. C. Yang and G. P. Brasseur. The nonlinear response of stratospheric ozone to NO_x and ClO_x perturbations. *Geophysical Research Letters*, 28(4):717, 2001.

[170] W. R. Young, A. J. Roberts, and G. Stuhne. Reproductive pair correlations and the clustering of organisms. *Nature*, 412(6844):328, 2001.

[171] J. M. Zalc and F. J. Muzzio. Parallel-competitive reactions in a two-dimensional chaotic flow. *Chemical Engineering Science*, 54(8):1053, 1999.

[172] C. S. Zhou, J. Kürths, Z. Neufeld, and I. Z. Kiss. Noise-sustained coherent oscillation of excitable media in a chaotic flow. *Physical Review Letters*, 91(15):150601, 2003.

[173] V. S. Zykov. *Simulation of Wave Processes in Excitable Media*. Manchester University Press, New York, 1987.